Enhanced Conducting Polymer PEDOT:PSS/ Silicon Hybrid Solar Cells:

Optimization of Thin Film Properties and Heterojunction Interactions

By

Donald McGillivray

A thesis

presented to the University of Waterloo

in fulfillment of the

Thesis requirements for the degree of

Doctor of Philosophy in

Chemistry

Waterloo, Ontario, Canada, 2019

© Donald McGillivray 2019

Examining Committee Membership

The following served on the Examining Committee for this thesis. The decision of the Examining Committee is by majority vote.

External Examiner	NAME: Giovanni Fanchini Title: Dr.
Supervisor(s)	NAME: Tong Leung Title: Dr.
Internal Member	NAME: Vivek Maheshwari Title: Dr.
Internal-external Member	NAME: Yuning Li Title: Dr.
Other Member(s)	NAME: Abdelaziz Houmam Title: Dr.

AUTHOR'S DECLARATION

This thesis consists of material all of which I authored or co-authored: see Statement of Contributions included in the thesis. This is a true copy of the thesis, including any required final revisions, as accepted by my examiners.

I understand that my thesis may be made electronically available to the public.

Statement of Contribution

Donald McGillivray contributed to the design, research, and execution of this study. D. McGillivray performed the experiments including sample preparation, characterization and device fabrication. D. McGillivray analyzed and interpreted all the data, and tested the solar cell performance. D. McGillivray wrote the paper (used in Chapter 3). Joseph P. Thomas, MD Anisur Rahman, Nina F. Heinig, Lei Zhang, Marwa Abd-Ellah, and Saurabh Sirvastava, discussed the results, and Dr. Tong Leung discussed, commented and edited the manuscripts.

Abstract

In this work the operating properties of PEDOT:PSS - silicon hybrid solar cells were carefully studied. The motivation is to find a cost-effective alternative to some of the energy, environmental and sustainability issues the world is currently facing. Solar cells are already providing plentiful renewable energy but they remain constrained by inflexibility, weight, cost and efficiency. Overcoming these obstacles will allow these energy producing devices to become widespread and, along with them, new technologies and economies to emerge. Hybrid solar cells (HSCs) address these issues by junctioning conducting polymer with an inorganic semiconductor. The beneficial properties of these materials can be exploited to improve the cost effectiveness, flexibility, and ease of processing of the polymer, and the electron lifetime and diffusion length, and stability of the inorganic material. PEDOT:PSS and n-type silicon is one such HSC with easily reproducible high efficiencies around 12% that could greatly reduce the cost per watt ratio and other challenges associated with conventional silicon solar cells.

In Chapter 2, the material properties of inorganic semiconductors, focusing on silicon, are introduced and the details of Schottky junctions, p-n junction and solar cells properties are discussed. These properties are compared and contrasted with conducting polymers, focusing on PEDOT:PSS, which function in a fundamentally different way from inorganics in that charge mobility is much more limited to intra or inter molecular transport. Finally the physics behind thin films and surfaces for the absorbance of light is examined.

In Chapter 3, a novel method of increasing the conductivity of PEDOT:PSS was found by post-treating pre-deposited films with a 50 vol% ethylene glycol/methanol mixture. This post-treatment method more than doubled the conductivity to 1334 S/cm over the method of adding an ethylene glycol co-solvent to the PEDOT:PSS solution (637 S/cm). It also reduced the film thickness in half (51%) due to the removal of PSS. The treatment resulted in PEDOT to have a greater quinoidal character, and because of the decrease in PSS, more defined PEDOT containing nanodomains with the chains laying horizontal to the substrate.

In Chapter 4, the optical properties of the films were studied using a single stack layer to model the reflectance of PEDOT:PSS on silicon and to determine the effects of film thickness on short circuit current density (J_{SC}). Using the complex refractive index, the reflection of PEDOT:PSS films and silicon respectively, and the phase shifts found from fitting experimental transmittance and reflectance data, the external quantum efficiency (EQE) for the cells could be simulated. The J_{SC} calculated from these results

showed that J_{SC} followed a sigmoidal curve and the highest value 28.3 mA/cm^2 was obtained at a thickness of 85 nm. Interestingly, the post-treated cells had overall lower J_{SC} with a maximum of 26.2 mA/cm^2 at 63 nm due to the increased anisotropy, absorbance and series resistance. A comparative measure of resistivity was performed by removing the optical component from the quantum efficiency to reveal the electrical contributions and by fitting the data using a modified single diode equivalent circuit. This indicated that the resistivity was 75% higher for the post-treated films over the co-solvent films. Using the absorbance, reflectance, and EQE models for the optimal thickness of 85 nm, the optical generation and loss mechanisms could be calculated: 61.5% of the incident light was converted into current, 22.2% was lost to reflectance, 6.9% was absorbed by the film, 2.7 was absorbed by the rear electrode, and 6.7 was lost to recombination at the surface and in the bulk silicon.

In Chapter 5, the PEDOT:PSS/silicon heterojunction was studied and the influence of passivation layers was examined using dark current density curves and the open-circuit voltage of the cell. It was discovered that the size of the native silicon oxide layer could be determined by the blue shift in the Raman C_α=C_β band. It was noted that the native oxide continued to grow uninterrupted after PEDOT:PSS was deposited on hydrogen-terminated silicon resulting in a contaminated native oxide layer with decreased performance. It was concluded that the contamination at the surface, increased defects and Fermi level pinning could cause a decrease in band bending, leading to increased carrier recombination and poor performance. Allowing a controlled native oxide layer to grow to 2 nm in a clean environment increased the inversion layer and performance. The increase in bi-polaron modes with post-treatment together with the increased concentration of PEDOT and the effective density of acceptor states resulting from the removal of PSS, caused a stronger inversion and electron blocking at the interface.

Finally in Chapter 5, P3HT was used as an interfacial layer between PEDOT:PSS and silicon. It was found that spin-coating a solution of P3HT dispersed in dichlorobenzene on silicon produced a homogeneous layer of small interconnected nanocrystallites. When applied to HSCs, no charge separation or transfer originating from the P3HT chromophore could be detected indicating the inversion layer existed entirely within the silicon substrate. However the larger open circuit voltage and change in dark saturation current undedicated the layer blocked electron majority carrier transfer from the silicon, increasing shunt resistance and open-circuit voltage.

By combining the research of into short-circuit current density, and open-circuit voltage, it was concluded that the highest achievable efficiency of the setup used in this research was 11.8%.

Acknowledgments

This thesis would not have been possible without the contributions of many colleagues and friends both at the University of Waterloo and elsewhere and I would like to direct my sincere gratitude to them. To my supervisor Dr. Tong Leung, I truly appreciated the amount of work you have done, providing me with this opportunity, on supporting me with resources, on the training on the many tools available and editing and providing feedback on this thesis. Your advice and guidance was highly valued, and I enjoyed my time learning and working in the WATlab.

My sincere thanks have to go to my advisory committee: Dr. Vivek Maheshwari, Dr. Yuning Li, and Dr. Abdelaziz Houmam for their constructive feedback, excellent discussions which always lead to new insights, and positive encouragement supporting me throughout this long stressful process. I would also like to thank Cathy van Esch for fielding my many questions, being an ear to listen, and always being positive.

I would very much like to think my lab mates: Jung-Soo Kang, Saurabh Srivastava, Hanieh Farkhondeh, Mahdi Beedel, and Marwa Abd-Ellah, and Frank Guan, for their friendship, inquisitiveness, and outgoing positive attitudes. A special thanks to Dr. Nina Heinig, and Dr. Lei Zhang for their training and endless help and patience with the many instruments that were a key component of this research. A very special thanks to Dr. Joseph Palathinkal Thomas, whose work this thesis builds off of and who introduced me to hybrid solar cells and showed me the device construction. Finally I want to thank Anisur Rahman, who acted as a sounding board for many of my ideas, and whose constant support, inquisitiveness, advice, and motivation helped me immensely over the years.

There were many generous people from outside the faculty that provided support and advice, specifically Christopher McMahon , Kevin Liu, Kier von Konigslow, and Benji Wales who acted as a brain trust and kept me focused.

Of course whether I was at the university or not there were people that supported and bolstered me, and were always very understanding, respecting my time constraints during the long process; this is especially true to my partner Emily Stahl. And last but certainly not least I would like to thank my parents who have always supported and encouraged me and loving me unconditionally while asking for nothing in return.

Table of Contents

List of Figures

List of Tables

1. Introduction

The sun continuously irradiates the earth with more than enough energy to satisfy the societies' demands.[1] Photovoltaics provides a sustainable method of capturing this energy, because it is pollution-free, stable, has no moving parts, and versatile when compared to other alternatives such as fossil fuels or nuclear energy. Photovoltaics makes use of an appropriate type of material capable of converting light into useful electricity, and it exploits the properties of semiconductor materials. Commercial photovoltaics are still expensive, energy intensive to produce, relatively inefficient, and it can be heavily dependent on the availability of rare materials that are hard to recycle. There is a push to develop new technologies to reduce the cost and increase the efficiency such that the price per kWh is more economical. One such emerging technology are semiconducting polymer solar cells, which can be produced in an efficient manner very inexpensively, but the photoconversion efficiency of these solar cells remains low. To obtain high efficiencies at low cost, there has been a fusion between inorganic and organic photovoltaics, commonly referred to as hybrid solar cells. These hybrid solar cells benefit from traditional photovoltaics, because they are more efficient than purely organic solar cells, and can be flexible, light weight, multicolour, and made with inexpensive and fast roll-to-roll processing. Beyond conventional energy demand in the future, hybrid solar cells will supply energy to unconventional applications and devices, open up new markets, and disrupt current ones.

1.1. Energy use and alternatives

The demand for increased energy caused by a rising worldwide middle class able to purchase more power hungry appliances, and new devices and appliances entering the market means that future power generation will have to increase. Adding this increased power demand to the increased environmental and security concerns caused by traditional energy production, it becomes clear that alternative energy sources such as solar should be exploited. Unlike the conventional sources of energy (coal, oil, natural gas, and nuclear energy), solar energy does not depend on quickly diminishing natural reserves. Along with other sustainable energy sources (such as hydro and wind), solar energy would provide the best balance between maintaining our current quality of life and being able to extend it long into the future.

Solar energy is evolving quickly, and the growth and cost numbers for 2016/2017 indicate that this is an industry quickly approaching those of legacy energy generation.[2] Table 1.1 compares different

electricity generating technologies reported in the US in the last 10 years from relevant studies (reported in 2010 USD). Shown are the average values, since there are large variations in the reported capital costs for electricity generation and they are influenced by the locations, regulations, labour cost, and financing options. The thermal efficiencies of power plants are determined by using the higher heating value that includes the heat of vaporization.[3] The current global price of energy generation provided by solar modules stands at $0.447/Watt and it represents about14% of the total cost of installation for which the average in the US is at $3.21/Watt in 2016 [GTM research]. Large scale solar is already approaching the $/kW installation cost of coal in Canada, and it should become increasingly competitive as technology improves. Fossil fuels have additional cost in Canada after accounting for its transportation across its large land mass, which provides distinct advantages for solar energy in remote communities. Furthermore, solar can be more easily implemented in the north where ice and tundra make building large plats or wind mills difficult.

Table 1.1: Cost, efficiencies and Canadian capacity of electric power generation.

Technology	Capital Cost ($USD/kW)[a]	Fixed Operation & Maintenance Cost ($USD/kW-year)[a]	Efficiency (%)	Total Canadian Capacity GWh 2016[c]
Coal (steam plant)	2900	25	38[b]	60374 (9.3%)
Coal (IGCC)[e]	4000	35	39[b]	
Natural Gas (simple cycle)	750	6	34[b]	65512 (9.6%)
Natural Gas (CC)[f]	1050	10	52[b]	
Biomass (steam plant)	4000	95	25[b]	13214 (2.0%)
Biomass (IGCC)	6000	140	30[b]	
Nuclear	5500	95	33[b]	95418 (14.6%)
Wind (on-shore)	2000	50	<59[d]	30462 (4.7%)
Geothermal	5200	100	10[b]	
Hydro			~80[d]	383392 (58.8%)
Solar				
Photovoltaic (Rooftop)	4200	60	~20[b]	-
Photovoltaic	2800	40	~22[d]	3568 (0.5%)

(Large-scale)				
Concentrated Solar	4800	65	-	-
Thermal Concentrated Solar	8000	65	-	-

a. NREL (National Renewable Energy Laboratory). 2016. *2016 Annual Technology Baseline*. Golden, CO: National Renewable Energy Laboratory. http://www.nrel.gov/analysis/data_tech_baseline.html.
b. Muratori, M.; Ledna, C.; McJeon, H.; Kyle, P.; Patel, P.; Kim, S. H.; Wise, M.; Kheshgi, H. S.; Clarke, L. E.; Edmonds, J. Cost of Power or Power of Cost: A U.S. Modeling Perspective. *Renew. Sustain. Energy Rev.* **2017**, *77* (December 2016), 861–874.[3]
c. Canadas Renewable Power Landscape 2017 – Energy Market Analysis. (2017) National Energy Board of Canada (https://www.neb-one.gc.ca/nrg/sttstc/lctrct/rprt/2017cndrnwblpwr/cndnvrvw-eng.html)
d. Kreith, F. *Principles of Sustainable Energy Systems*; CRC Press, 2014.[4]
e. Integrated gasification combined cycle (IGCC)
f. Combined cycle (CC)

Like all emerging technologies, solar energy will become even more cost-competitive with ongoing R&D, scale-up and commercialization. The adherence of Moore's law in the semiconductor industry has caused a large reduction in the price of silicon wafers and has allowed the solar industry to follow a similar price reduction and efficiency increase in what is referred to as the Swanson's law.[5] Over the last 40 years, the price of solar modules decreases by 20% with each doubling of modules shipped. This has been the case for conventional silicon solar cells, but much research is taking place on different solar conversion technologies and there is great potential to accelerate Swanson's law. While this rapid cost decrease in solar modules is occurring and is reducing the total cost of photovoltaic generation, the cost of building a new power plant based on fossil fuels has increased.[3]

Unconventional solar cells can be generally split into two groups: very high efficiency or inexpensive, both with the aim of lowering the cost-to-Watt ratio. High-efficiency photovoltaics includes germanium arsenide solar cells, cadmium telluride solar cells, solar cells used in space applications, and multi-junction solar cells used in high-concentrator photovoltaics (which have proven efficiencies between 20 and 46%), while inexpensive photovoltaics includes: amorphous silicon solar cells, dye sensitized solar cells, quantum dot or plasmonic solar cells, organic solar cells, hybrid solar cells, perovskite solar cells, and copper indium gallium selenide (CIGS) cells. Typical performances of the more common solar cells are compared in Table 1.2. With the exception of amorphous silicon solar cells, these lower-cost cells are still in the research and development phase. A great deal of work is ongoing

with the goal to improve the stability, longevity, toxicity and performance. However, hybrid solar cells stand out since they can piggy-back on the proven efficiencies of silicon and are significantly simpler in design and preparation than the others. They have a real potential to fulfill the demand for low cost/watt.

Table 1.2: Photovoltaic materials and properties of lower-cost solar cells.

Type of Photovoltaic Cell	Material	Open-circuit voltage (V)	Short-circuit current density (mA/cm^2)	Fill factor	Photoconversion Efficiency (%)	Ref.
Conventional Silicon	Crystalline silicon	0.696	42.0	0.836	24.4	(6)
Provoskite	Formamidinium lead iodide	1.11	25.0	0.817	22.6	(7)
CIGS	Copper indium gallium selenide	0.741	37.8	0.806	22.6	(8)
Hybrid solar cell	PEDOT:PSS – n-Si	0.663	31.9	0.7	14.8	(9)
Dye sensitized solar cell	TiO_2, Cobalt electrolyte, Porphyrin dye (SM315)	0.91	18.1	0.78	13.0	(10)
Amorphous silicon	H-Silicon	0.55	28.74	0.75	11.9	(11)
Bulk heterojunction solar cell	J61[a] :ITIC[b]	0.912	18.31	0.706	11.77	(12)

a. Benzdithiophene-alt-fluorobenzotriazole copolymer
b. 2,2′-[[6,6,12,12-Tetrakis(4-hexylphenyl)-6,12-dihydrodithieno[2,3-*d*:2′,3′-*d*′]-s-indaceno[1,2-*b*:5,6-*b*′]dithiophene-2,8-diyl]bis[methylidyne(3-oxo-1*H*-indene-2,1(3*H*)-diylidene)]]bis[propanedinitrile]

1.2. Hybrid Solar Cells

Modern electronic devices are based on semiconducting materials, and silicon has long been the material that has dominated the industry. Silicon is abundant around the world, low-cost and stable, and it has been extensively studied and developed forming the foundation of today's technologies, with mature production capabilities. However, unlike inorganic semiconductors, the properties of polymers can be easily altered through chemical means. Polymers can be easily synthesized and processed, and they are flexible, colorful and more versatile than inorganics. Many challenges remain until polymers can compete with silicon and be used to produce the low-cost and versatile devices dreamt about. However, we can come closer to reaching this goal by combining silicon with polymers in devices and gain the versatility

that is lacking in silicon while boosting the stability and electronic properties of polymers. This symbiosis is evident in the advances of hybrid solar cells.

Hybrid solar cells (HSCs) incorporate the benefits of both inorganic and organic material groups such as the high stability, long electron lifetime and diffusion length of an inorganic material; and the lower-cost, processability and flexibility of an organic polymer. HSCs are developing into a viable alternative to conventional silicon-based cells and they strive to greatly reduce the price per watt produced. There are three types of HSCs depending on where most light is absorbed and charge carriers are produced: (i) the organic chromophore, (ii) both organic and inorganic materials, or (iii) the inorganic semiconductor.[13] Cells designed to absorb most light close to the heterojunction show greater charge separation and efficiency.[14] Since HSCs are highly adaptable, they allow for the optimization of the absorption spectrum and electronic properties through changes in the organic or inorganic material, providing an effective way to optimize absorption.

HSCs with a p-n junction, consisting of a n-type silicon *base* and a p-type conducting polymer blend [poly(3,4-ethylene-dioxythiophene) poly(styrenesulfonate) (PEDOT:PSS)] *emitter* layer, have been shown to produce efficiencies as high as 14.8%.[9] In a typical PEDOT:PSS – n-Si HSC, shown schematically in Figure 1.1, light absorbed in the silicon base produces positive and negative charge carriers which can be separated by an electric field between the top (silver) and bottom (aluminum) electrodes. These separated charges at the interface enter the circuit through the silver anode and aluminum cathode and they can be used to do electrical work.

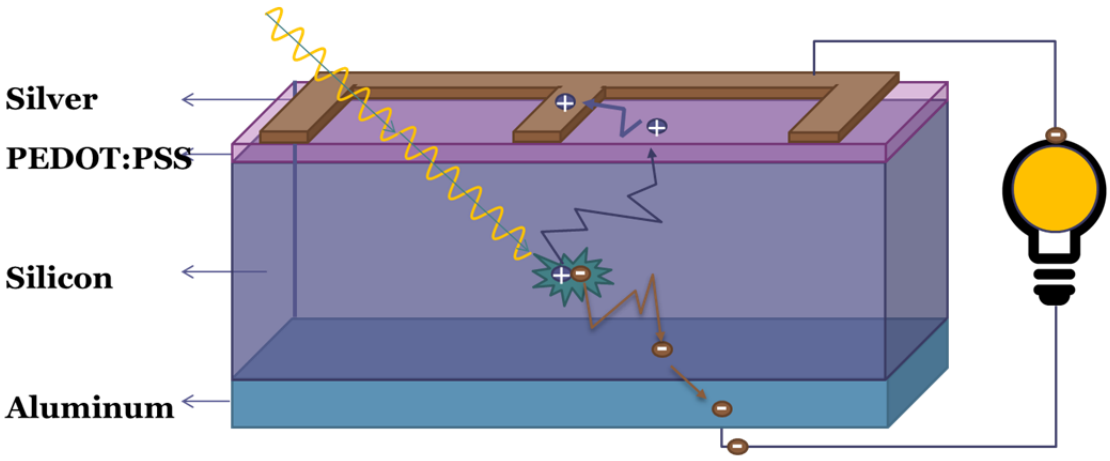

Figure 1.1: PEDOT:PSS – n-silicon hybrid solar cell with a top silver anode and a bottom aluminum cathode. Light is absorbed and electron-hole pairs are created in the silicon base, the charge carriers are then separated due to the built-in-potential at the junction and they then enter the circuit through the electrodes to do work.

Combining the p-type PEDOT:PSS with n-type silicon produces an extraordinarily simple hybrid solar cell. Due to the low absorption coefficient of PEDOT:PSS throughout the visible spectrum, most of the light is absorbed and charge carriers are produced in the silicon base.[15,16,17] The PEDOT:PSS layer provides the built-in potential at the interface for charge separation and acts as a hole transport medium. However, the high potential of the lowest unoccupied molecular orbital (LUMO) of PEDOT:PSS causes the cell to be current-limited by the hole drift into the PEDOT:PSS layer, [16,18,19,20] which remains to be one of the greatest challenges in developing a viable HSC technology.

1.3. Thesis Objectives

The main objective of this research is to investigate the optical and electrical interactions between PEDOT:PSS and n-type silicon and the production of energy in hybrid solar cells. Chapter 2 discusses the fundamental concepts of semiconductor physics, solar cells, conducting polymers, analysis of PEDOT:PSS and P3HT, and the optical properties of thin films. In Chapter 3, the methods used to increase the conductivity of PEDOT:PSS are investigated, with particular attention paid to removing the insulating PSS component, which can have auxiliary consequences on the photovoltaic performance. The existing understanding of conductive enhancement, in particular post-treatment of the films, is found not to be sufficient in explaining the electronic trends seen in photovoltaic operation. An improved morphological and electrical model appears necessary in understanding how these properties change after chemically altering the film and consequently in optimizing the photovoltaic behavior.

In addition to the morphological and electrical properties of the PEDOT:PSS film, photovoltaics performance is dependent on the optical characteristics, in particular its absorptivity, and reflective properties of the film (Figure 1.2). In Chapter 4, using experimentally derived reflectance and quantum efficiency data, a model is proposed to account for the changes in absorptivity, reflectivity off silicon, refractive index, and resistivity as functions of the film thickness and concentration of PSS. With knowledge of how these parameters are correlated, they can be optimized to maximize the photocurrent produced by the cell.

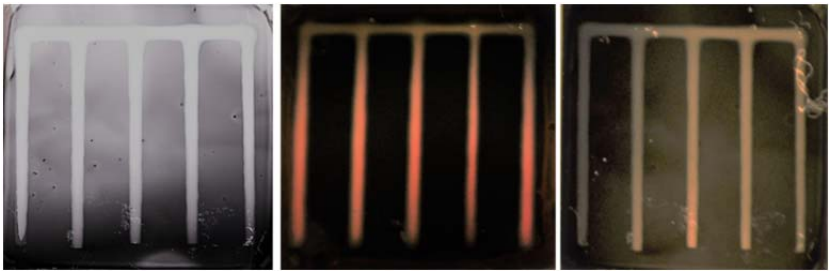

Figure 1.2: 1 cm^2 PEDOT:PSS hybrid solar cells.

The ability of a solar cell to capture light and to produce photo-carriers is one of two photovoltaic properties needed to produce power, the other being the electromotive force needed to propel the carriers around the circuit. In HSC, this electric potential depends on the complex and highly sensitive junction between PEDOT:PSS and n-silicon. In the fabrication of HSC, this junction can be formed by spin-coating, printing, or doctor-blade application of the organic compound in solution, all of which are commonly performed in ambient conditions and not systematically deposited in vacuum controlled conditions. The composition of these surfaces and their electronic properties are therefore considered contaminated, when compared to the clean pristine “ideal” surfaces. Chapter 5 examines the important interfacial effects introduced by silicon oxide growth, thickness, PEDOT:PSS composition, and the application of a poly(3-hexyl thiophene) interfacial layer. The investigation of the nature of this sensitive junction will lead to a better understanding of the interfacial properties that are beneficial for improving the efficiency and stability of HSC.

2. Fundamentals

In this section the fundamental principles involved in the operation of hybrid solar cells will be presented. An introduction to semiconductors is given before discussing combining them with other materials to form junctions essential to the functioning of solar cells – Schottky and p-n junctions – and their interaction with light to generate photo-carriers and their subsequent recombination. Like conventional solar cells, the HSCs in this work involve silicon. A brief description of silicon is therefore given before explaining the main operation principles of solar cells. The fundamentals behind conducting polymers is presented since they form the counterpart to silicon in HSCs and the polymers PEDOT:PSS and P3HT used in this thesis are described. Finally the optical properties of thin films and their contribution to light absorption in solar cells will be discussed.

2.1. Semiconductors

The transport of electrons and the conversion of light to electricity (and vice-versa) in solids requires an understanding of the band theory of solids. This well-developed theory can be used to explain, among other things, the differences between metals, semiconductors and insulators, the movement of charge carriers in them, the optical properties of solids, and the properties associated with surfaces and junctions. These properties could be well understood by the Kronig-Penney model of an electron in a one-dimensional periodic potential and the Bragg/Lowe model concerning the wave reflections in a crystal lattice.[14]

The Kronig-Penney model reveals the dispersion relation between the wavevector ($k=p/\hbar$) and energy of an electron.[21] It defines the allowed energy ranges that the electron can exist or its electronic energy bands, separated by energy gaps or band-gaps (forbidden regions where charges cannot exist). The Bragg equation identifies that the Brillouin zone boundaries as the locations that the electron wave experiences strong reflections from the crystal lattice planes, and the locations where the energy gap minima are likely to be observed.[22]

Simplistically, as atoms are brought together to form a molecule or a lattice as in a crystal, the wavefunctions of the valance electrons begin to overlap. Since no two electrons can share the same set of quantum numbers, as bound by the Pauli Exclusion Principle, the orbitals split into discrete energy levels. Given the large number of atoms in a solid lattice, these discrete orbitals become closely spaced in energy, and the large number of closely spaced energy levels can be effectively considered as a continuum or a

band of allowed energies. As the atoms are brought closer together the next electron shell may begin to interact and split into another band of allowed energies and so forth for each electron shell. Between these bands can be gaps where no solution to the Schrödinger equation exists and thus elections with that energy cannot exist, this gap is called the band-gap (Figure 2.1). At 0 K the available electrons will completely fill the low-lying states. The maximum number of states in the highest occupied energy band corresponds to double the amount of unit cells in the lattice (2N) due to the degeneracy arising from the electron spin quantum number, *s*, of either ½ or -½. In materials such as silicon or germanium with an even number of valance electrons, all the states up to the band-gap are filled at 0 K, since there is an even number of states. The band below this gap is referred to as the valance band and the empty band above the conduction band. Electrons gaining energy equal or above that of the energy gap can move from valance to conduction band. Those with large band-gaps (>4 eV) are insulators. Materials with a small band-gap (< 3 eV) that can be easily overcome with additional energy is referred to as semiconductors. Electrons in the conduction band can easily access additional empty states that allow for movement and conduction. A half-filled band is the result of an odd number of valance electrons, as in the case of metals such as Al, Ga, and In, and can also be easily promoted to (partially) empty higher states within the band. Electrical conductivity results if an electric field is enough to impart a net momentum to these electrons.

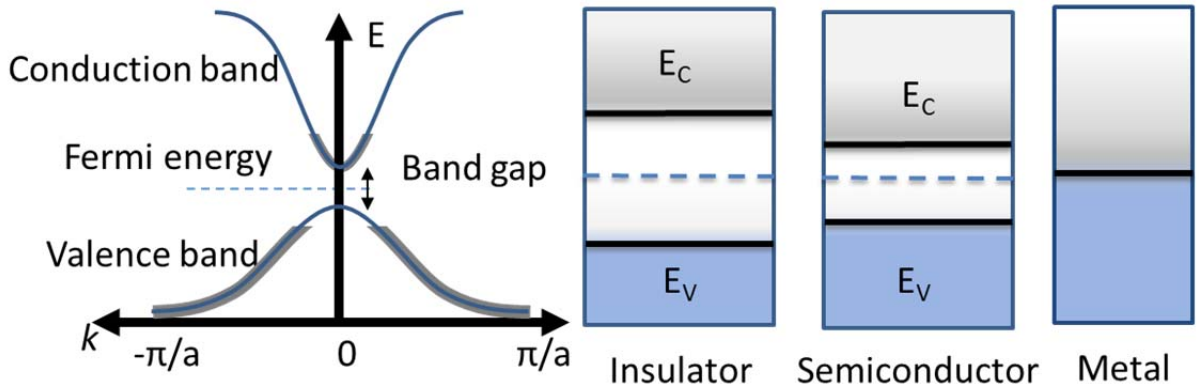

Figure 2.1: Left: reduced zone scheme of E vs k for the first Brillouin zone boundaries π/a. Right: energy diagrams for an insulator, a semiconductor and a metal. E_c and E_v represent the conduction band and valance band respectively.

In semiconductors, if energy greater than the band-gap energy can be imparted to the electrons, such as through thermal or photoelectric excitations (as is the principle behind solar cells), the electron can leave breaking its covalent bond. The electron excited into the conduction band leaves behind a

broken bond, called a hole. The empty states in the valance band are mobile as they can be quickly filled with electrons and contribute to the conductivity. These electron-hole pairs give rise to two independent charge carriers. At higher temperatures, electrons will naturally be excited filling a state in the conduction band and leaving behind a hole. The energy above which there is a 50% probability of finding an electron and below which a 50% probability of finding a hole is called the Fermi energy. Since in pure or intrinsic semiconductors there is an equal number of conduction-band electrons and valence-band holes, the Fermi energy lies midway in the band-gap.

Under an applied electric field the acceleration of an electron or hole in a crystal will depend on the reflections of its wave function off the crystal planes and the interaction with other charges. The effective mass is used to signify differences in inertia of electrons and holes for different materials.[23] For some semiconductors, the valance band maximum and conduction band minimum coincide at the same crystal momentum, and results in a direct band-gap semiconductor (as shown in Figure 2.1). For these, an increase in energy equal to the band-gap is all that is needed to promote an electron. Semiconductors such as GaAs, GaN and CdTe have a direct band-gap. An indirect band-gap results when the valance band maximum and conduction band minimum occur at different *k* values. Silicon and GaP belong to this group, for which both energy equaling the band-gap and the correct momentum are needed to excite an electron from the valence band to the conduction band. The distinction between direct and indirect band-gaps is important in solar cells and diodes, which involve photons whose momentum, $= \frac{h}{\lambda}$, is very small, making harder for an electron to make the transition through absorption alone. The extra momentum is usually supplied by a phonon, or lattice vibration, which is dependent on temperature. For this reason excitations to the conduction band are more difficult but the converse is also true. Indirect band-gaps have longer carrier lifetimes and diffusion lengths because they need a phonon to recombine.

The Fermi level in an intrinsic semiconductor is found at the mid-gap energy. However, doping the semiconductor through the incorporation of different impurities allows for the control of electron or hole concentrations and can be used to shift the Fermi energy. When doping is done using atoms with additional valance electrons than the constituent atoms in the crystal, they could act as electron donors. The excess electrons, which do not form bonds, are only weakly bound and can easily be excited and fill conduction band states. The result is an n-type semiconductor, an example of which would be a silicon crystal, belonging to Group IV, doped with a group V atom such as phosphorus. On the other hand, when an atom with one less valance electrons is used for doping, they act as electron acceptors, attracting electrons that result in hole states in the valance band and making it a p-type semiconductor. Boron, a

group III atom, is an electron acceptor that is commonly used to make p-type silicon. When dopant atoms are added, the number of electrons in the conduction band no longer equals the number of holes in the valance band. Instead, at room temperature, it is assumed that all dopant atoms are ionized such that the number of electrons (holes) in the conduction band (valance band) is equal to the number of dopants, since this temperature is not considered sufficient to excite a large number of electron-hole pairs. It is possible to change the Fermi level upon doping, so that it will lie closer to the conduction band in an n-type material, and to the valance band in a p-type material. This results in conduction that is dominated by the movement of electrons in n-type or holes in p-type materials.

2.2. Junctions

Solar cells and light emitting diodes (LEDs) depend on an internal electric field confined to a small cross-section occurring at a junction where a material composition gradient exists. The field is referred to as a built-in potential, and it is the driving force behind the photovoltaic separation of charges that causes the electrons and holes to separate in opposite directions. The effective electric field can result from gradients in the effective density of states, work function (ϕ),[†] electron affinity (χ),[‡] and band-gap. A charge carrier density gradient by itself is not enough to generate a net current if the diffusion constants for elections and holes are the same, because any charges carriers separated by the field will simply recombine through diffusion. A potential difference only exists in an asymmetric environment where there is a mechanism to favour selectively removing electrons or holes, such as contact with a cathode or anode, respectively. The transition that forms the gradient can be achieved at the interface between two different materials, i,e. a heterojunction, or through a gradual change in the composition of an alloy, i.e. a homojunction. In a conventional p-n junction solar cell, the gradient is formed by varying the doping level (work function) of a single semiconductor, and/or by limiting material defects common with heterojunctions.

The Fermi level, a measure of the electron energy level of a material described above, lies within the half-filled conduction band of a metal, or in the forbidden energy gap of a semiconductor. When two

---

[†] The energy required to remove the least tightly bound electron from the Fermi level in the material (E_f) to the vacuum level (E_{vac}). $\phi = E_{vac} - E_f$

[‡] The energy difference between the conduction band minimum and the vacuum level. $\chi = E_{vac} - E_c$

materials with different Fermi levels are brought into contact, charges will flow across the junction to achieve the lowest energy configuration (unless, in the rare case, that the two Fermi levels align with each other). Unlike a metal, an internal electric field can be maintained in the semiconductor. This flow of electrons out of (or into) the semiconductor at the junction comes from donor (or acceptor) atoms in the semiconductor. This leaves the surface region from which the donors (or acceptors) originated ionized opposite to the bulk. These carriers originate from the space charge region, that exists one diffusion length from the interface (about 1 micron in silicon) beyond that the electric field falls back to zero. Charge carriers will flow from this space charge region until a charge gradient builds up sufficiently to prevent further flow, at which point the two layers are in thermal equilibrium. Unlike the electric potential, the electron affinity and the band-gap are material specific, and invariant with respect to the vacuum level. The conduction band and valance band energies must therefore change and bend to accommodate the changing energy levels in this region. This phenomenon is referred to as band bending. The amount of band bending is equal to the built-in-potential (qV_{bi}).[14,23,24,25]

2.2.1. Schottky Junction

In a metal-semiconductor junction, if the semiconductor is n-type, as inFigure 2.2., the space charge region becomes depleted of the majority carriers (electrons) and has a positive charge. This results in the conduction band and valance band bending upwards in this region, leading to an energy barrier for the electrons to overcome in order to leave the semiconductor for the metal. This barrier is equivalent to the difference between the work functions of the two materials. Consequently, there is an inequivalent impediment for the electron flow in both directions. These junctions that impede the majority carriers are referred to as Schottky contacts.[24] For current to flow across the junction a potential must be applied to overcome this barrier, and this junction is referred to as a Schottky junction.

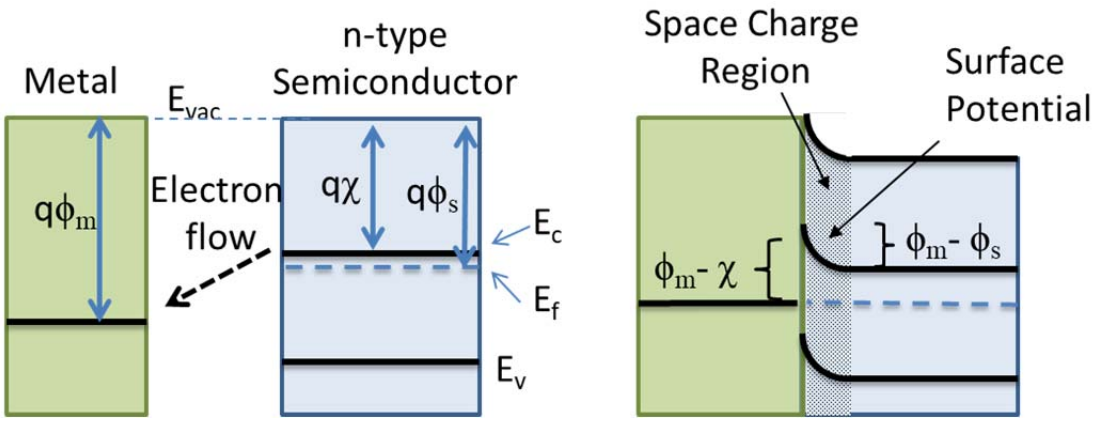

Figure 2.2: Fermi levels and band energies of separated and joined n-type semiconductor and metal. After contact, electrons flow from the semiconductor to the metal forming the space charge region (shaded area) and resulting in band bending and an electron barrier to electron flow in both directions. q is the electronic charge, ϕ_m and ϕ_s are the work functions of the metal and semiconductor, respectively, χ is the electron affinity, E_{vac} is the vacuum-level energy, E_f is the Fermi energy, and E_c and E_v are the energies corresponding to the conduction band minimum and valance band maximum, respectively.

In the case where the electron affinity of the metal is smaller than that of the n-type semiconductor, charges will flow from the metal to obtain equilibrium, leaving the space charge region electron rich and causing the bands to bend downward (Figure 2.3). In this case, there is no potential barrier for the flow of electrons from semiconductor to metal, although there is in the other direction. These junctions that freely allow the flow of majority carriers from the semiconductor, with the resulting current being linear with respect to the applied voltage, are referred as the ohmic contacts.

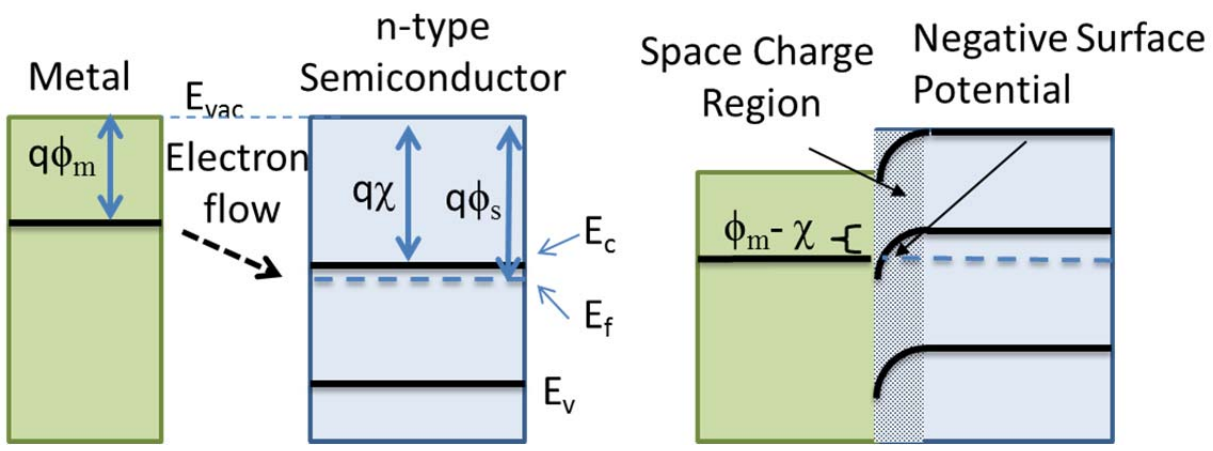

Figure 2.3: Metal and n-type semiconductor before and after contact to form an ohmic junction. Electrons flow into the semiconductor and a negative charge builds up on the semiconductor surface. There is no potential barrier to the electron flow from the semiconductor to the metal.

Schottky junctions are dominated by the flow of majority carriers, and electrons in the metal experience a larger potential barrier than those in the semiconductor (as represented by Figure 2.2). Without any external potential only electrons in the conducting material with enough kinetic energy can overcome the barrier, which is dependent on temperature (T) and is called thermionic emission. Thermionic emission is determined using the equation: [14,23,24,25]

$$J_e = A^{**}T^2 \exp\left(-\frac{q(\phi_m-\chi)}{kT}\right), \tag{2.1}$$

where A^{**} denotes the reduced effective Richardson constant that is material-specific for the junction, and k is Boltzmann's constant. Equation 2.1 illustrates that the Schottky diode reverse saturation current decreases as the barrier height increases. Besides the buildup of charges in the semiconductor to minimize the potential energy of the system described above, there are other sources of charges that could exist at the junction. These include: (i) Dangling bonds occurring at the interface since the lattices of the conductor material and semiconductor might not match along different crystallographic orientations. (ii) Diffusion of metal atoms into the semiconductor causing a change in the surface potential. (iii) The presence of oxide layers or other impurities at the interface that could change the surface potential (e.g., silicide formation in metal/silicon junctions). Since silicon interacts strongly with oxygen, it is very difficult to completely eliminate oxygen, the presence of which tends to trap positive charges due to the passivation of Si

dangling bonds.[26,27] The buildup of these charges causes band bending that is difficult to predict and must be regulated.

2.2.2. p-n Junction

The junction between two oppositely doped semiconducting materials forms the foundation of modern electronics. When electrons coming from donors in the n-type material combine with holes in the p-type material, both sides of the junction become oppositely charged with respect to the bulk. The space charge region that exists across the junction is referred to as the depletion region since it is devoid of majority carriers. The result is that majority carriers (electrons in the n-type side and holes on the p-side) need to overcome a potential barrier while the minority carriers (that comprise the photocurrent in a solar cell) could easily cross. A benefit of this is that potentially a much larger electric field can be created than those found in the Schottky junctions.

When the combination of n-type and p-type materials has reached their lowest energy configuration, an equilibrium is established, in which case the diffusion current resulting from a concentration gradient of the majority carriers and the drift current from the minority carriers entering the electric field cancel out, resulting in no net current. By taking a particle view of charge transfer and looking at the charge flux (electrons moves from negative to positive, opposite to the conventional current, while holes go from positive to negative), four carrier fluxes are considered. These are minority carrier drift involving (i) electrons on the p-side or (ii) holes on the n-side entering depletion region driven by the built-in-potential; and majority carrier diffusion involving (iii) electrons on the n-side or (iv) holes on the p-side diffusing across the junction due to the concentration gradients (Figure 2.4).

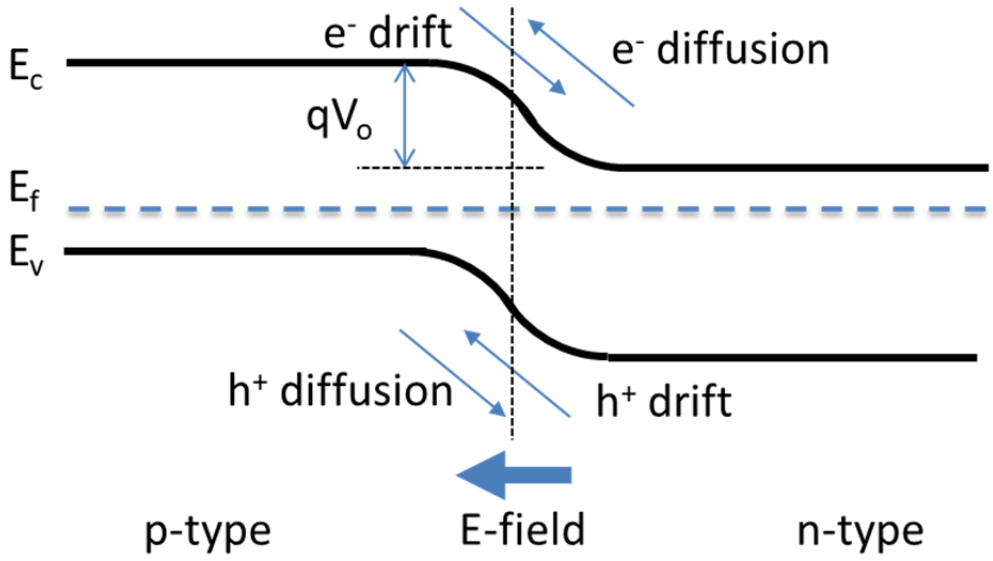

Figure 2.4 Band model of p-n junction showing the presence of the electric field across the depletion region and the contribution of hole and electron drift and diffusion. Note that electron and hole currents are used (opposite convention).

Applying an external bias to the diode will alter the electric field and the effective energy barrier height. Applying a forward bias, V > 0 (against the built-in-potential, negative electrode on p-type, positive on n-type), reduces the energy barrier resulting in a much larger diffusion flux (Figure 2.5). On the other hand, applying a reverse bias, V < 0 (in the same direction as the built-in-potential), increases the potential energy barrier, decreasing diffusion, and results in current dominated by the carrier drift flux. The sum of these fluxes becomes the measurable diode current density J and is given by:

$$J = J_o\left(\exp\left(\frac{qV}{kT}\right) - 1\right), \tag{2.2}$$

where J_0 is the reverse saturation current density described below, V is the applied potential, k is the Boltzmann constant, and T is the temperature. Counter-intuitively the current in reverse bias does not go to zero. This is because drift fluxes are dominated by thermally generated (or photo-excited) minority carriers that produce a constant current. This current is essentially independent of the reverse bias but related to material properties, such as the band-gap, doping level (number of electron acceptors, N_A, or donors, N_D) , amount of defects, carrier lifetime (τ_n, τ_p) and diffusion coefficient (D_n, D_p), as well as the

condition whether the carrier is generated on the n or p side of the junction. It is referred to as the reverse saturation current density, J_o, and is given by:[23]

$$J_o = qn_i^2 \left[\frac{1}{N_A} \sqrt{\frac{D_n}{\tau_n}} + \frac{1}{N_D} \sqrt{\frac{D_p}{\tau_p}} \right]. \quad (2.3)$$

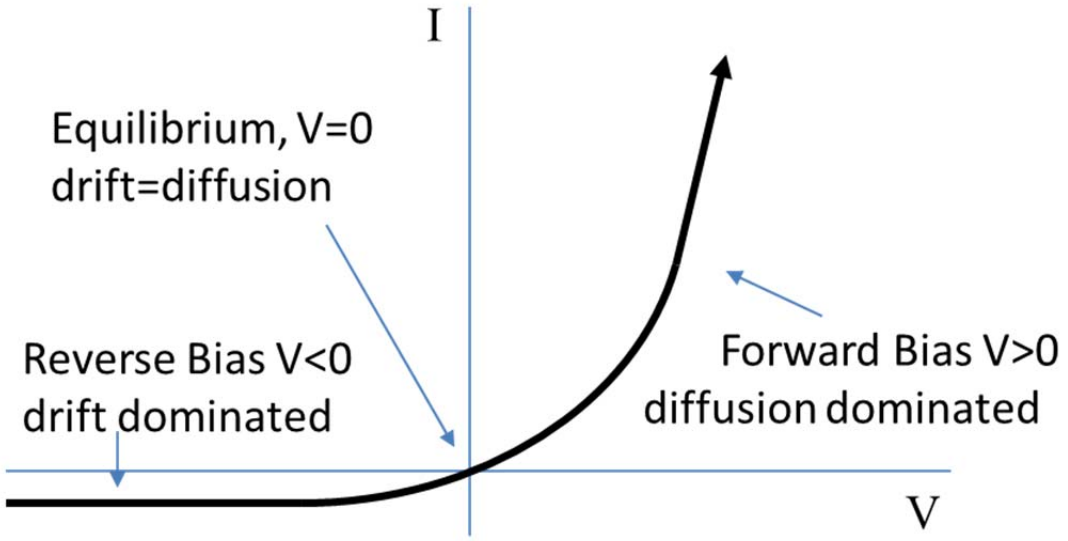

Figure 2.5: Diode current for the forward and reverse biases.

2.3. Carrier Generation and Recombination

The p-n junction provides the potential in solar cells but the photocurrent that flows through needs to be generated from exciting electrons that can make it to the circuit. It is important to maximise carrier creation while minimizing carrier loss for efficient solar cells of any type. Generation of carriers requires an input of energy equal to or greater than the forbidden energy gap, which can be provided thermally, or by lattice vibrations (phonons) or from radiation. Recombination is the destruction of carriers through electronic relaxation with the release of energy. Recombination could follow three different mechanisms: radiative recombination – with photon emission; non-radiative recombination – without phonon emission; or Auger recombination – imparting the excess energy to another free carrier (Figure 2.6Figure *2.*).[25]

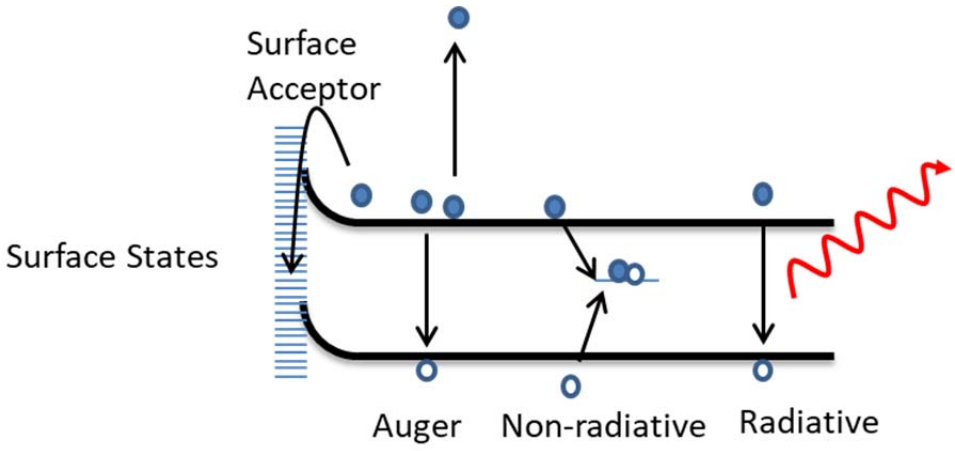

Figure 2.6: Types of recombination involving Auger, non-radiative, radiative processes.

Photogeneration is crucial to photovoltaic devices and it involves the generation of mobile charge carriers through the absorption of light by a semiconductor. The attenuation of light passing through a material is given by the macroscopic absorption coefficient α(λ), and the intensity, I, at a given thickness, d, can be found using the Beer-Lambert law:

$$I(x) = I(0)e^{-\alpha d} \tag{2.4}$$

The absorption coefficient is related to the imaginary part of the refractive index:

$$\mathrm{Im}(n) = \kappa = \frac{\alpha\lambda}{4\pi} \tag{2.5}$$

The total photocarrier generation rate for a material is the sum of all photon energies entering the material with energy above the band-gap energy that can be absorbed in the material given its thickness. Energy in excess of the band-gap is lost through thermalization, where the excess kinetic energy is imparted to the lattice through collisions that occur rapidly, on the picosecond time scale. [23,25]

Radiative recombination depends on carrier concentrations, since increasing the dopant level will increase recombination rate due to the increased probability of combining with a minority carrier, therefore $R \propto np$, where n and p are the carrier concentrations of electron and holes respectively.[14,24,28] It is suppressed in materials with an indirect band-gap since a phonon is needed for conservation of momentum.

Auger recombination is higher for low band-gap, doped materials at high temperatures. Of the recombination processes, non-radiative recombination processes are most affected by design and manufacturing of the photovoltaic devices, and steps can be taken to avoid these recombination processes, in contrast to radiative and Auger recombination processes, which are physical, intrinsic material processes in nature. Non-radiative processes usually involve trap states due to crystal impurities or defects. Shockley-Read-Hall recombination is a prevalent non-radiative process that involves trap states in the band-gap. A trap state is spatially localized in the material as opposed to free carriers, and it limits the mobility of the captured carriers. A trapped carrier can be released by thermal activation, or if a carrier of the opposite polarity is also captured the carriers will recombine, empting the trap. In areas where the doping concentrations are similar, $n=p$, such as in the depletion region, traps will lie close to the mid-gap, and they become effective recombination centers. Since defects are much more likely to occur at surfaces and interfaces due to dislocations, broken bonds and extrinsic impurities, they have a higher density of trap states and higher likelihood of annihilation of carriers. The result is a steady leakage of carriers to the surface resulting in a surface recombination current.

2.4. Silicon Wafers and Conventional Solar Cells

The main contributors to the high cost of silicon wafers are the silicon purification techniques, the high temperatures needed for growing and doping silicon, and the difficulty in processing the very hard and brittle material. Since hybrid solar cells in this work employ n-type silicon and in order to understand the cost and time savings for HSCs, a brief description of processing silicon and conventional solar cell development is given below.

To make a silicon solar cell, the silicon is first refined. Oxygen is removed from the SiO_2 starting material, usually in the form of high-purity quartz rock, by heating it (to 1500°C – 2000°C) in the presence of carbon.[29]

$$SiO_2 + C \rightarrow Si + CO_2$$

The resulting metallurgical grade silicon is then reacted with HCl at 200°C allowing the impurities to form their halides (e.g. $FeCl_3$, $AlCl_3$, BCl_3) so that distillation can be used to isolate the $SiHCl_3$. $SiHCl_3$ is

then reacted with hydrogen at 1100°C in a very time-consuming process (> 1 week) to produce the high-purity silicon.[30]

$$Si + 2HCl \rightarrow SiHCl_3 + H_2$$

$$SiHCl_3 + H_2 \rightarrow Si + 3HCl$$

To produce crystalline silicon, the Czochralski method is most often used. In this method, highly crystalline silicon is used as a seed for growing a single-crystal ingot from molten Si. Polycrystalline silicon is made simply by allowing the molten Si to cool slowly, which is much cheaper but this also leads to grain boundary defects. Upon appropriate doping, the ingot bulk can be p-type (usually doped with boron) or n-type (doped with phosphorus).[30] The ingots are then cut to size and cleaned in hot sodium hydroxide to remove the saw damage. For conventional solar cells, the wafer bulk is usually p-type and a phosphorus coating is screen printed on top. The wafer is then sintered above 1000°C to dope the surface through diffusion to form the p-n junction.[25] An antireflection coating (commonly TiO_2 or SiN_x) can also be added. Finally, the front comb-shaped or busbar contacts and the rear electrode are added, usually using Ag for the former and Al for the latter because of their desirable work functions.

2.5. Solar Cell Operation

Conventional solar cells combine n-type and p-type materials with different electron affinities to form the junction, and the built-in potential is dependent on the band offset as shown in Figure 2.4. Wherein lays a tradeoff, since a stronger built-in potential can be created with a larger band-gap material, which results in less absorption and therefore less photocurrent. There is therefore a delicate balance between the two in forming high-efficiency solar cells. Heterojunctions specifically in hybrid solar cells present an interesting challenge since the junction types and the absorption properties must be finely tailored. The operation of conventional *p-n* junction solar cells will be discussed below since many of the fundamentals are the same for HSCs.

The p-n junction solar cells are operated in the forward bias, and they depend on minority carriers excited through the absorption of light. A photo-generated electron-hole pair in the bulk continues to experience a coulombic attraction. However, if the electron-hole pair is generated at or sufficiently near the junction, it is allowed to migrate to the depletion region. The electron and the hole can be separated upon entering the field, resulting in minority carrier drift that contributes to the photocurrent. For this reason,

the photocurrent is said to be made up of minority carriers. As described above for a diode, under the reverse bias condition, there is a constant current due to the thermal excitation of electron-hole pairs (creating the so-called reverse saturation current). This is similar for a solar cell, except that the carriers are primarily excited by the absorption of radiation, and the reverse current increases in magnitude that is dependent on the light intensity and energy. Greater generation of the carriers and drift current means that open-circuit voltage occurs at a much larger forward bias and the entire ideal diode curve is shifted down such that the ideal diode equation under illumination becomes:[14,25]

$$J = J_o\left(\exp\left(\frac{qV}{kT}\right) - 1\right) - J_l \tag{2.6}$$

where J_l is the current density generated by photo carriers. The J-V curve is measured in the fourth quadrant, as seen in Figure 2.7, but it is conventional to reverse the sign of the current since they are assumed to generate power and not to consume it. By setting the current to zero, the built-in-potential can be estimated by solving for the voltage:

$$V_{OC} = \frac{kT}{q}\ln\left(\frac{J_l}{J_o} + 1\right) \tag{2.7}$$

and is referred to as the open-circuit voltage.

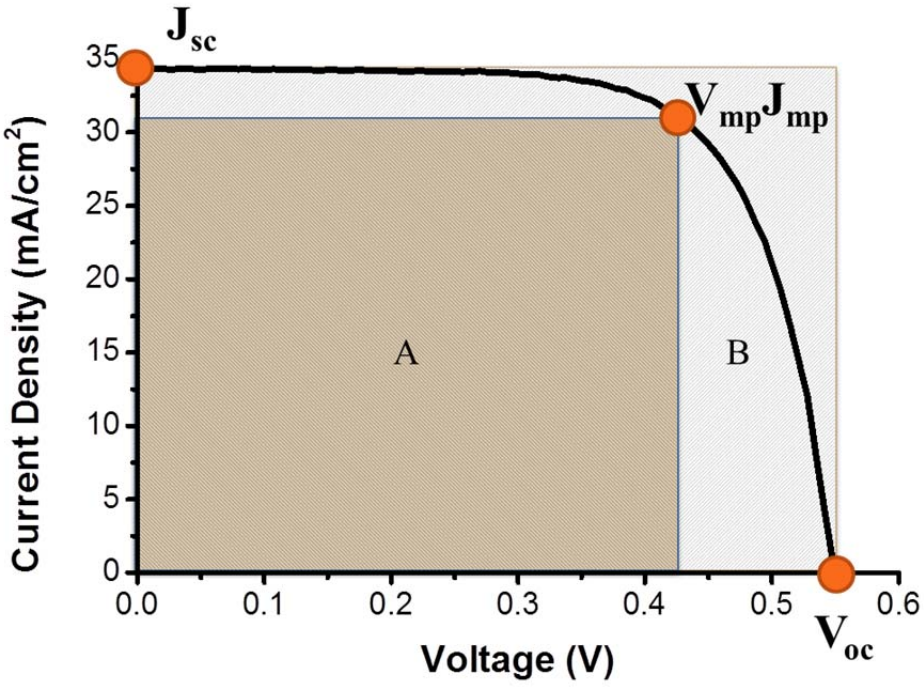

Figure 2.7: J-V characteristics of a solar cell under illumination, showing the operating point at which the area of the rectangle A is maximized.

In operation the maximum power density output occurs when the product, $P = JV$, is maximized as indicated by V_{mp} and J_{mp} in figure 2.7. The fill factor (FF) is used as a figure-of-merit to quantify the quality of the solar cell and is defined as the ratio of the theoretical maximum power of the cell, the product of short-circuit current density and open-circuit voltage ($J_{SC} \times V_{OC}$) to the actual maximum power density output ($J_{MP} \times V_{MP}$):

$$FF = \frac{J_{MP}V_{MP}}{J_{SC}V_{OC}} \tag{2.8}$$

For crystalline silicon solar cells, the fill factor is usually between 0.7 and 0.85.[25]

The ideal single diode equivalent circuit model is often used to describe the shape of the J-V curve under steady-state operation conditions (Figure 2.8), where the photogenerated electrons account for the source of the photocurrent, I_{ph}. The diode is used to represent bulk recombination, where R_{sh} is the

shunt resistance representing an alternative pathway of photocarrier recombination (e.g. surface Shockley-Read-Hall recombination), R_s is the ohmic series resistance that takes into account the conductivity of the emitter and base, electrical contacts and wiring, and finally V_{cell} is the operating voltage related to the built-in potential.

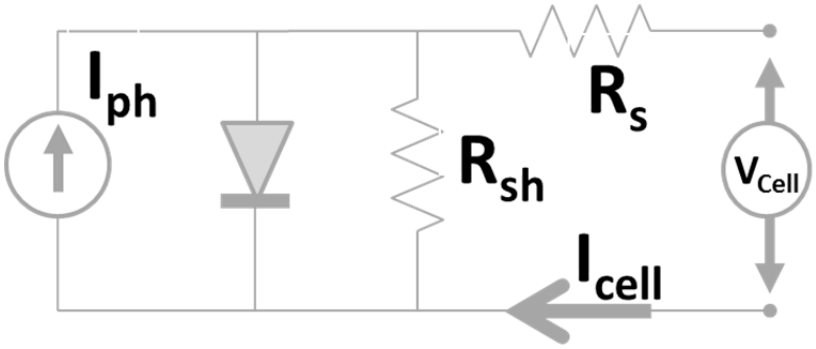

Figure 2.8: Single diode equivalent circuit model for a solar cell.

For which the output current I_{cell} is given by:

$$I_{cell} = I_{ph} - I_0 \left[\exp\left(\frac{qV}{nkT}\right) - 1\right] - \frac{V + IR_s}{R_{sh}} \tag{2.9}$$

Ideally, light would be absorbed at the junction where the field is present so that electron-hole pairs are immediately separated without a chance to recombine. The location where absorption occurs in a material is a function of the absorption coefficient, and in most semiconductors a higher visible irradiation energy results in a smaller penetration depth. For these two reasons, the junction should be close to the surface where these photons are being absorbed. Hybrid solar cells are specifically designed to take advantage of this by tailoring the polymer emitter layer. To maximize the efficiency of the cells, they should be built with an understanding of the illumination conditions in which they will be functioning. For the sake of evaluation in our terrestrial environment, all cells are measured under standard testing conditions, i.e. at 25°C and under a black body spectrum of 5800 K (American Society of Testing Materials) shown in Figure 2.9. This solar spectrum is referred to as AM1.5G and it represents the sunlight reaching the cell

through the atmosphere at an angle of 48° (from the vertical), taking into account the global (hemispherical) spectrum. It can be simulated by combining tungsten and xenon lamps. With an intensity maximum at 500 nm, the solar spectrum is mostly made up of contributions between 250 nm and 1000 nm (5 – 1 eV), which makes silicon with its band-gap 1.12 eV ideally suited.

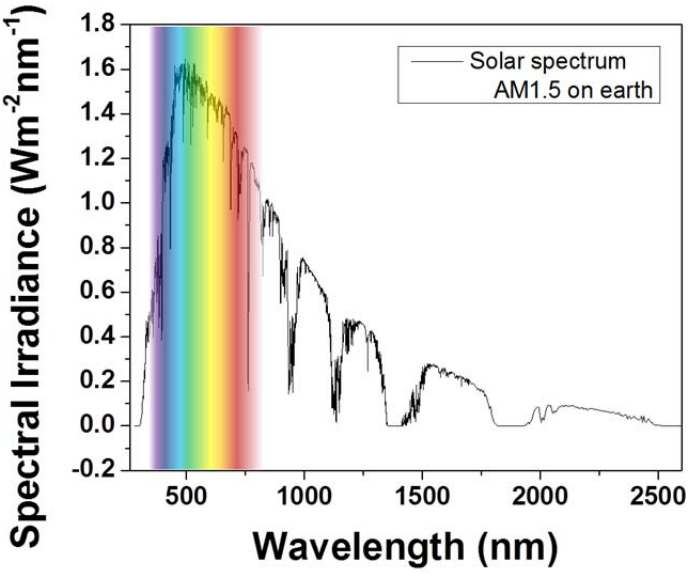

Figure 2.9: Solar radiation spectrum on earth AM 1.5. Data from: American Society for Testing and Materials (ASTM) Terrestrial Reference Spectra for Photovoltaic Performance Evaluation.[31]

2.6. Conducting Polymers

Conducting polymers, specifically polyacetylene, were discovered in 1977, which gained Allan J. Heeger, Allan MacDiarmid, and Hideki Shirakawa a Nobel Prize in Chemistry in the year 2000.[32] In the past few decades, the field of conducting polymers has matured rapidly to a point where currently a wide range of applications has been envisaged. These conducting polymers have tremendous opportunities in polymer electronics and can function in devices that are flexible, colourful or transparent and easily processable. These properties make them highly advantageous for "optoelectronic" devices such as displays, light emitting didoes (LEDs) and especially photovoltaics.

Conducting polymers refer to a chain of carbon atoms with alternating π and σ bonds or a conjugated structure, arising from the ability of carbon to have 3 different hybridizations: sp^3 (alkanes), sp^2 (alkenes), and sp (alkynes). Using ethylene as an example, there are three sp^2 orbitals that form sigma

bonds (two with hydrogen and one with the other carbon), the two remaining p orbitals from each carbon atom are used to form the other covalent C=C bond, which is higher in energy and delocalized perpendicular to the plane formed by the sp^2 orbitals. This bond orientation forms the lowest energy configuration of ethylene. Above the highest occupied molecular orbital (HOMO) is the lowest unoccupied molecular orbitals (LUMO) to which electrons can be excited. The energy gap between the HOMO and LUMO in molecules is similar to the band-gap seen in semiconductors. Adding a second ethylene molecule to the existing molecule could produce a butadiene molecule with four carbon atoms and two π bonds. Adding a third ethylene molecule would lead to a hexatriene molecule with 6 carbon atoms and 3 π bonds. For $(CH)_{2N}$, there are $N/2$ delocalized π and π* bonds resulting in a conjugated structure. Each time we add units to the chain, we add additional bonding configurations and energy levels, the energy levels become closer together, reducing the energy between the HOMO and LUMO to that of a band-gap. In semiconductors, it is the conduction band electrons that are mobile. In conjugated polymers the π electrons are delocalized and free to move around the polymer backbone. However, it requires energy equivalent to the energy gap to switch the conjugation of C–C and C=C and the movement of charges. This is a simplified explanation of intra-chain conduction in polymers, the ring structures and impurities of which are rarely uniform and are thereby complicating the physics used to describe them.[33]

There are obvious limits in the intra-chain conduction in the bulk material if it were the only mechanism of charge transport. The confinement of charges to a chain would not result in charge transport if the chain is not aligned with the field, even if it is, it would end up being trapped if there is no other means of hopping to another chain once isolated from the electrodes. Inter-chain transport is caused by quantum-mechanical tunneling by which charges hop between chains.[34] Inter-chain transport increases in importance as the chain length decreases. Hopping can also occur at kinks or defects or between two aromatic rings. As activation energy is needed for inter-chain hopping, conductivity in polymers, unlike semiconductors, increases with temperature. The delocalized electron cloud between two stacked ring structures will overlap due to van der Waals interaction. The absorption of a phonon allows an electron in one aromatic ring to lower its energy by moving to a nearby ring contributing to conduction.

2.6.1. Doping

As in semiconductors, doping causes a shift in the energy levels of the conjugated polymers. Doping can therefore be used to shift the energy levels to make them more conducting or change their absorption properties. Conducting polymers can be doped chemically by exposing them to electron accep-

tors (p-type dopant) or donors (n-type dopant), or electrochemically. A redox reaction results between the dopants and the polymer chains, and together they form an ionic complex. This complex results in oxidized or reduced polymer chains and their counter anion or cation, if an acceptor or donor is used respectively. Halogens such as those in AsF_5, and $FeCl_3$ are often used as acceptors but so can polymers like PSS, while alkali metals are used as donors.[33] The electrical properties including energy levels and the Fermi level can be altered through doping, which allows for the tunability of the material to act as an organic semiconductor or even a metal in some cases.[35] As in semiconductors doping in polymers introduces energy states within the band-gap just below the LUMO or above HOMO, resulting in charged quasi-particles referred to as polarons. While doping does not stoichiometrically alter the polymer chain, it can cause molecular rearrangement by changing the nature of the bonds to accommodate the additional charges in the chain.

2.6.2. Excitons

Conduction in polymers differs greatly from the generally understood conduction in metals and semiconductors, and is better understood using the concept of excitons, or elementary electronic excitations. These quasi-particles consist of solitons, polarons, and bipolarons (Figure 2.10) and are able to move along the polymer chains and participate in hopping between them.[33]

Conducting polymers are categorized as either degenerate or non-degenerate depending on the degeneracy of the ground state. Polyacetylene is an example of a degenerate polymer in which the alternating single and double bond configuration results in alternating bonds of different length in the ground state. Such a polymer chain would have an energy curve with two equal minima, where, if a perturbation was to cause the alternating C=C and C–C to reverse, it would have an equivalent energy state. Aromatic polymers, such as PEDOT, are non-degenerate since no two equivalent states could exist. The presence of the fixed ring structures breaks the degeneracy because any perturbation must cause alteration of the bond lengths. The bond lengths for joining the rings in the ground state are larger than the double bonds in the quinoid conformation. A perturbation causing bond alteration would have to raise the energy by a small amount (>0.4 eV) to overcome an activation energy.[35,36]

For degenerate polymers in which an electron is added or removed, through doping, photo or thermal means, the electronic energy levels rearrange themselves into a new lowest energy state resulting in a new conjugation. The alternating conjugation could become broken with the addition or removal of a double bond, respectively, due to the presence of an unpaired electron. This new state is stabilized by the

presence of a soliton, which can be neutral with a spin of ½ or positively or negatively charged (with *e*) but no spin.[35] The presence of a soliton is often associated with kinks and defects and is delocalized over several monomer units. The soliton is located in the middle of the band-gap.

When an electron is added to or removed from a non-degenerate conducting polymer, the polymer gains or losses a charge of *e* and spin ½ that is localized over several monomers, which obtains a quinoidal conformation[33]. This charge is called negative or positive polaron, depending on the addition or removal of the charge, or radical cation or anion in chemical terminology. Addition or removal of two electrons results in a bipolaron with a charge of ±2*e* if the spins of the separate polarons combine, although two polarons existing on one chain is also possible.[33] The bipolaron extends further over multiple units with the charges at the extremes, and are identified in PEDOT:PSS. Polarons and bipolarons are associated with energy levels within the band-gap. The locations of these excitons in mid gap states are ideal for characterization using typical spectroscopic means, including UV-vis, IR and Raman.[35]

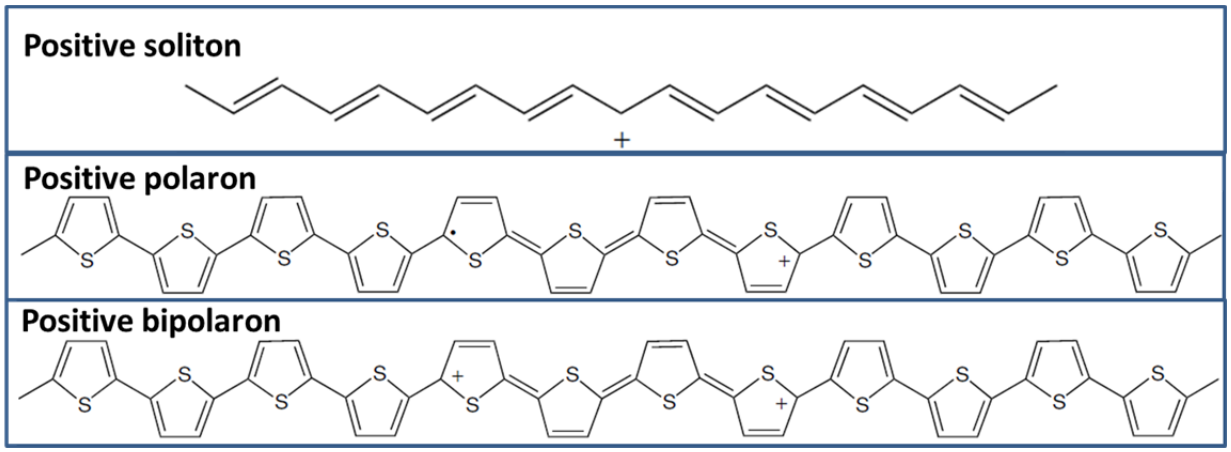

Figure 2.10: Elementary electron excitations in polymers.

2.7. PEDOT

2.7.1. Discovery and Synthesis

Polythiophenes have been known to have some interesting electronic properties since 1967.[37]After the conductive properties of polyacetylene was discovered, in the Nobel work of Heeger,

MacDiarmid, and Shirakawa, heterocycles with S or N heteroatoms were often added to help stabilize these polymer chains.[32] The thiophene or pyrrole rings provide the rigidity and stabilize the conjugated, doped bipolaron state through the electron-donating function of N or S.[33] It was in the 1982 work of Tourillon and Garnier that showed the true conducting properties (10-100 S/cm) of thiophene when it was electropolymerized with perchlorate or tetrafluoroborate counterions.[38] This discovery started a flurry of work, and poly(3-alkyl-thiophenes) (P3HT) were produced but they showed poor stability in air. However, oxygen-substituted thiophenes such as poly(alkoxy-thiophenes) showed promising stability and conductive properties, since the oxygen-bearing substituent could further delocalize the free radical and positively charged forms.[39] Working with this knowledge, Bayer Central Research Department attempted to extend the thiophene structures to bicyclic ring systems. After failing with 3,4-methylenedioxythiophene and 3,4-propenedioxythiophene, they achieved success with 3,4-ethylenedioxytiophene (EDOT). EDOT was unstable and oxidized easily but after they polymerized it by the action of iron-III chloride, it was found that PEDOT (Figure 2.11 b) had excellent conductive and stability properties. Jonas, Heywang and Schmidtberg were credited with the invention of PEDOT in 1980 and a patent in 1988.[40] Shortly after, synthesis of PEDOT by electrochemistry using the monomer EDOT was reported.[41] A year after, PEDOT was combined with PSS to enable suspension in water and to better facilitate its widespread usage.[39]

PEDOT is a p-type conducting polymer that is electrochemically stable and transparent. It has a rigid backbone and planar geometry. In its oxidized state, it has high electron delocalization along its chain and a conductivity of 10 – 750 S/cm (as-polymerized 10^{-3} – 10^{-5} S/cm). The work function for PEDOT is 5.1 eV but it can be extended to 5.4 eV with an increased doping level.[42] PEDOT has an optical absorption band maximum at 2 eV which shifts to 0.6 eV upon doping.[43]

Table 2.1: Synthetic approaches of producing PEDOT

Synthesis Method	Details	Conductivity	Ref.
Oxidative Chemical Vapor Deposition (Vapor phase polymerization)	In this approach, a PEDOT film is produced by pyrolysis. An oxidant (i.e. $Fe(III)Cl_3$) is coated on a substrate and is then placed into a vacuum chamber. The EDOT monomer is sublimated around 110°C and allowed to condense and polymerize on the substrate. The films are rinsed with methanol to remove the oxidant, unreacted monomer, and spent oxidant (i.e. $Fe(III)Cl_2$).	9.1 x 10^{-4} S/cm (at a Cl doping level of 17%)	(42,44)
		348 S/cm (at a Cl doping level of 33%)	
		2500 S/cm	(45)
Self-Oxidation of	2,5-Dihalogeno-EDOTs are unstable and over time	80 S/cm	(46)

EDOT Halogens	they will decompose and transform into PEDOT solid. A prolonged reaction time (2 years) at low temperature (20°C) results in higher conductivities.		
Oxidative Polymerization	PEDOT is synthesized through a redox reaction of EDOT with metal ions from $FeCl_4^-$, $FeCl_3$, MgO_2, $Ce(SO_4)_2$, and $CuCl_2$, and followed by reaction in boiling acetonitrial or polypyrrole, and benzonitrile. Peroxodisulfates such as NaS_2O_8 and hypervalent iodine compounds, such as Koser's Reagent, are good oxidants that form conductive PEDOT.	(1 – 600 S/cm)	(47)
Oxidative Polymerization using $Fe(TOS)_3$	The highest conductivity obtained using oxidative polymerization is with iron(III) complexes. EDOT is dissolved in a weak base imidazole solution, and then added to a solution of $Fe(TOS)_3$ at 100°C. The mixture is then spin-coated onto a substrate. Polymerization occurs upon annealing at 110°C. The films are washed with methanol.	750 S/cm	(48)
Electrochemical Polymerization of PEDOT	Uniform PEDOT films can be made to polymerize at the cathode in a potentiostatic or galvanostatic cell. This method is effective in doping the films since the choice of counterion is limited only by the solubility of the salt in solution.	650 S/cm	(49)

2.7.2. PEDOT:PSS

The insulating PSSH anion (Figure 2.10 a) was first used in 1990 as the host polyelectrolyte and a template for PEDOT synthesis since the PEDOT polycation is insoluble in any solvent.[50] Therefore the PEDOT:PSS polyelectrolyte complex is formed *in situ*. PSS is durable and soluble in water, and it has no absorption in the visible region. The sulfonic acid group makes it strongly acidic and polar. Upon adding PSS in excess to the solution, the solubility of the EDOT monomers is increased, and PSS acts as an acid catalyst for the reaction. With a pH <3, the solution becomes more acidic as the reaction progresses.[39] Peroxodisulfates with monovalent cations (Na^+, K^+, NH_3^+) are used as the oxidizing agent often in combination of a Fe(III) salt as the catalyst for the polymerization of EDOT in water.[51]

The weight ratio of PEDOT:PSS typically ranges from 1:2.5 to 1:20, which corresponds to a thiophene group to sulfonic acid group molar ratio of 1:1.9 to 1:15.2, and this weight ratio will affect many physical properties of the films. PEDOT has a typical molecular weight of 1000 – 2500 g/mol (representing 6 to 18 repeating EDOT units) while PSS has a typical weight of 400,000 g/mol.[52,53] The PEDOT:PSS dispersions in water, in most cases, are below 2% with a viscosity under 80 mPas. Given the different unit spacing between charges in PEDOT compared to those of PSS, it is assumed there is no

ordering at the molecular or supramolecular level and the arrangement is expected to be of "spaghetti" type. The excess PSS surrounds the non-polar PEDOT, forming a micellar gel particle analogous to a nucleosome neckless (Figure 2.10 c). The size of the gel particles in solution ranges from 10 nm to 1 μm (but shear energy can be used to reduce the size). A larger gel particle results in greater conductivity but lower viscosity.[51] The gel particles themselves are entangled to a degree and are held together by hydrogen bonding between the sulfate groups of PSS.[54]

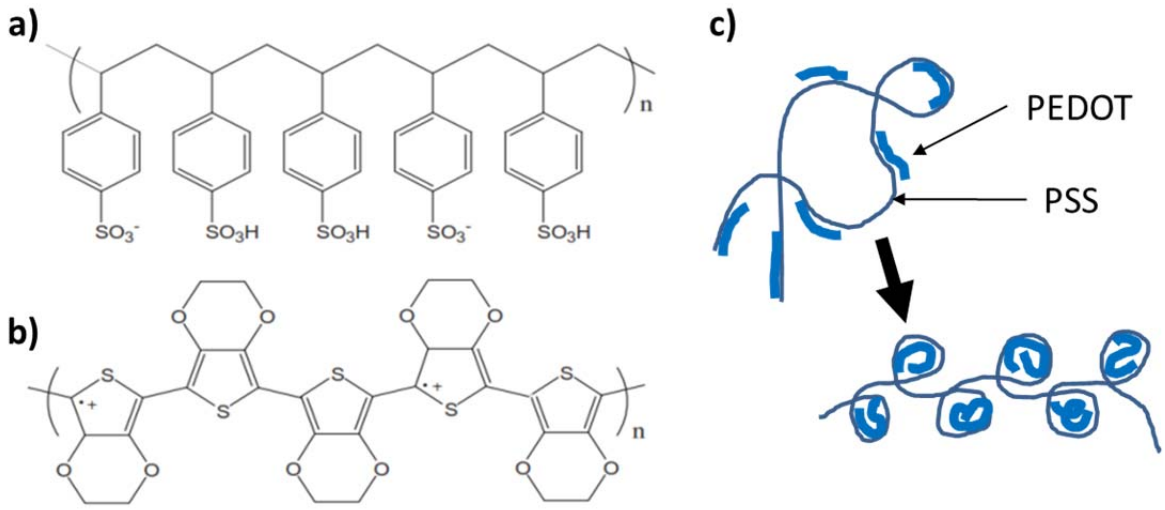

Figure 2.11: Chemical structures of a) PSS and b) PEDOT. c) *In-situ* polymerization on PSS and the rearrangement of the polyelectrolyte complex into micelles.

PEDOT:PSS is sold by Heraeus under the brand name Clevios™, which offers different grades with varying PEDOT:PSS weight ratios, viscosities and unsaturated conductivities varying from 10^{-5} – 1 S/cm. The popular Clevios PH1000 has a conductivity of ~1 S/cm, 1:2.5 PEDOT:PSS by weight, a boiling point 100°C, pH 1.5-2.5, and a granular size around 30 nm.[55]

2.7.3. PEDOT:PSS Film Properties

The as-deposited PEDOT:PSS films are mechanically stable with a Young's modulus of 0.9 GPa at 55% relative humidity (rH) and 2.8 GPa at 23% rH.[56,57] Films are thermally stable up to 200°C,[58] above which PSS will start to fragment at 250°C and undergo carbon oxidation above 250°C.[59] PEDOT:PSS is optically transparent in the visible range, with PSS absorbing in ultraviolet and charge carrier scattering of

PEDOT observable in the infra-red range. PEDOT is sensitive to light induced degradation by light-enhanced oxidation in the presence of oxygen. Sulfoxide and sulfone structures can form on the thiophene ring, or a hydroxyl group can form on the α-carbon atom next to the thiophene sulfur impeding conductivity.[60]

PEDOT:PSS shows stable p-type conductivity, which can be described by the variable range hopping (VRH) model, but only holes contribute to the charge transport since electrons will immediately be trapped by positively charged (oxidized) sites on the chain. [61] The work function for PEDOT:PSS is relatively high, 5.13 ±0.05 eV, with the Fermi level near the middle of the band-gap.[62,63]

For most semiconducting polymers deposited under ultra-high vacuum conditions, the alignment of the Fermi levels when interfaced with a metal occurs through a shift in the Fermi level in such a way that the vacuum level changes linearly when there is a change in the work function of the metal substrate. These types of interfaces fall within the Schottky-Mott regime, in which the vacuum level of the polymer, ϕ_p, changes linearly with the work function of substrate, ϕ_m, such that $\frac{\partial \phi_p}{\partial \phi_m} = 1$ and the Fermi level of the polymer is free to move within the band-gap.[64] However, PEDOT:PSS does not follow this trend. Instead, it approaches the Bardeen limit ($\frac{\partial \phi_p}{\partial \phi_m} \rightarrow 0$) similar to that demonstrated by small molecules and contaminated surfaces. [62,65] It is not until the outer PSS layer of the micellar grains is removed that mid-gap Fermi-level pining, consistent with a higher density of states of a heavily p-doped polymer (polarons), is identified. This indicates that PEDOT:PSS could equilibrate its Fermi level with that of a substrate by means of interface charge transfer because of its high density of charge carriers. A thin layer of insulating PSS will, however, reduce the interaction. [64] More importantly for solar cells and diodes, PEDOT:PSS exhibits a metallic behavior when interfaced on various metal substrates. The alignment of the Fermi level occurs through charge transfer at the polymer-metal (or polymer-semiconductor) interface, as described in Section 2.2.

2.7.4. Secondary Doping

It has been discovered that the conductivity of PEDOT:PSS can be increased by orders of magnitude simply by adding a co-solvent such as ethylene glycol to the polymer solution or by post-treatment by applying a solution to the as-deposited polymer. This is referred to as secondary doping

because it results in an increase in the conductivity of the already doped polymer,[‡] which can be maintained even after the removal of the secondary dopant.[66] Secondary doping usually causes a change in the morphology or an increase in the crystallinity. A range of chemicals including organic solvents, polyols, ionic liquids, surfactants and salts have proven to increase the conductivity of PEDOT:PSS films. The highest conductivity for the films have been produced by post-treating the films with sulfuric acid (4380 S/cm^{-1}) but the strong acid is very destructive to the film.[67]

The increase in conductivity is directly related to the film forming process where changes are observed both at the surface and in the bulk after adding a secondary dopant. A reduction in the amount of PSS can be seen from atomic force microscopy (AFM) and X-rap photoelectron spectroscopy (XPS) and this has reduced the tunnelling barrier to charge transport between PEDOT domains. [63,68,69] Ouyang *et al.* observed a change from the benzoidal, coiled structure of the PEDOT to the more elongated quinoidal structure. The quinoid conformation is due to bond distortion caused by the addition of a charge carrier (in this case, a hole) to the chain. It breaks up the degeneracy allowing for greater delocalization and the movement of charge carriers along the conjugated structure. Unlike polyacetylene with a linear chain of conjugated bonds, altering the bonding in an aromatic polymer such as PEDOT also has an effect on the energy levels.[35] An activation energy must be overcome to raise the energy state to that of the quinoid conformation. This can be done through doping or photo-excitation and is associated with the formation of bipolarons in PEDOT. The bipolarons are delocalized and they tend to be bound the quinoidal conformation over multiple monomer units.

2.8. P3HT

Poly(3-hexylthiophene) (P3HT) is another popular p-type conducting polymer used in thin-film transistors and in organic heterojunction solar cells when combined with (6,6)-phenyl-C_{61}-butyric acid methylester (PCBM), because of the excellent hole mobility >1 cm^2/Vs of P3HT.[70] P3HT has HOMO – LUMO gap of 2.28 eV, with interesting self-organizing properties and multiple crystalline structures. For these reasons, P3HT is also a good candidate for application in HSCs.

[‡] Primary doping refers to the addition of small quantities of an ionic material to increase the conductivity of the polymers as described above in the doping section.

P3HT consists of a conducting thiophene backbone with hexyl side chains attached to the third carbon, which increase its solubility and help with crystallization (Figure 2.12). Its conductive properties and crystallinity are highly sensitive to the molecular weight, and a high regioregularity is desired. Synthesis of regioregular P3HT makes use of the Grignard metathesis reaction, and Soxhlet extraction is used to isolate the desired product by molecular weight. P3HT is non-conducting in its natural state and only becomes conducting upon the addition of charges through doping. The HOMO level occurs at -5.12 eV and the LUMO is at -2.84 eV.[71,72]

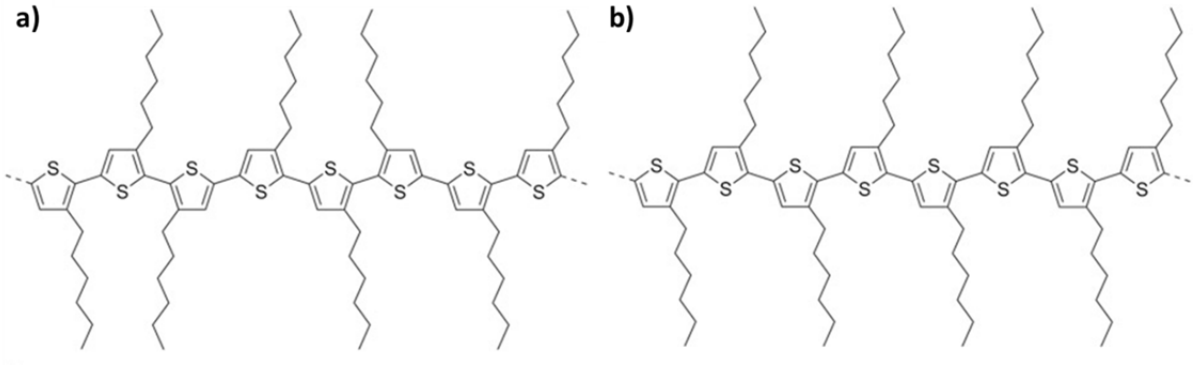

Figure 2.12: Placement of the hexyle side chains to produce (a) regioirregular, and (b) regioregular poly(3-hexylthiophene).

Regioregular P3HT is a rigid, planar polymer. Because of the strong intermolecular interactions, it will form ordered crystalline lamella and aggregate into spherulites, elongated 1D nanocrystals or fibers. Crystallinity is developed perpendicular to the polymer backbone, which is caused by the stacking of polymer chains due to the strong π-π interaction and repulsion arising from the hydrophobic interactions of the alkyl side chains. The polymer chains stack or zig-zag, along the fibrils folding back on themselves. The width of the nano-fiber is proportional to the temperature and molecular weight.[73] Crystal formation can occur in solution or after deposition. Chain orientation with regards to the substrate can be edge-on, face-on, or even standing chain. The edge-on orientation is by far the most common (Figure 2.13) and is obtained under equilibrium conditions without being kinetically quenched by rapid drying. Charge transport is highest along the chain axis (c-axis) and π-stacking direction (b-axis) and worst through the insulating side chains (a-axis).[74]

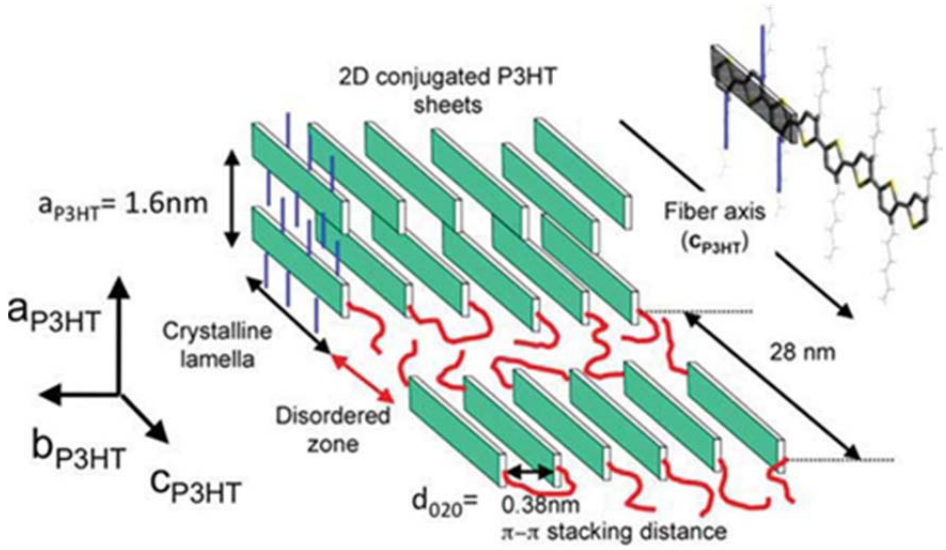

Figure 2.13: Edge-on chain orientation and stacking of P3HT (Reprinted from Ref. 74 with permission from Wiley-VCH).

2.9. Thin Films

The ability for solar cells to absorb light depends not only on the nature of its component materials but also strongly on their surface texture and reflectivity. It is only the absorbed light that can contribute to the photocurrent. As the PEDOT:PSS layer in a HSC is effectively transparent, it plays two important roles: (1) as the emitter layer to produce the built-in potential, and (2) as an optical thin film with the appropriate thickness, optical properties, and surroundings (other layers) to control the transmittance of light.

For efficient utilization of light, it is desirable to minimize the amount of reflection and to facilitate light absorption at the p-n junction. An anti-reflection coating can be tailored to optimize both of these functions. Reflection or transmittance at an interface is dependent on the refractive index of both media, the angle and polarization of the incident light and the proportion reflected can be given by Maxwell's equations. For reflection:

$$R = \left(\frac{n_1 - n_0}{n_1 + n_0}\right)^2 \tag{2.10}$$

where n_0 and n_1 are the complex refractive indices of the two media. When coating is applied to a surface, incident light will be reflected twice, once at the front surface and again at rear of the coating. When the phases of both these electromagnetic waves are 90° out of phase, they will undergo destructive interference reducing the reflectance (or constructive interference if they are 180° out-of-phase). For normal incidence, this will occur when the thickness of the film (d) is an integer value of a quarter of the wavelength of the incident light, $d = \frac{\lambda}{4n_1}$, or if the index of refraction of the middle film (n_1) film is the square root of the product of the surrounding films (n_0 and n_2) $n_1 = \sqrt{n_0 n_2}$. By using the appropriate index of refraction and film thickness, light can also be trapped through total internal reflection and be used in the solar cell. Since the solar spectrum is broad, the optimal wavelength for absorption should be in the middle of the spectrum.[‡] Often multiple anti-reflective coatings are added to provide minimal reflectance over a wider range of wavelength.

Since reflection and transmission depend on the angle of incidence, texturing or roughening a surface will scatter the incident light and can therefore be used to increase the absorbance. A randomizing texture is often used on the rear surface of the cell to reflect the unabsorbed light back, causing total internal reflectance and effectively increasing the path length and increasing the probability that it can be absorbed.[†]

[‡] For conventional silicon solar cells, reflectance is minimized in the red region corresponding to the high solar irradiance. However this makes them reflective in the blue region, causing them to often appear blue or violet.

[†] Asymmetrical front surfaces are used to increase the transmittance into the cell and increase the path length through it but they are mostly used with tracking systems with a constant angle of incidence.

3. PEDOT:PSS Film Post-Treatment – Optimization and Analysis[‡]

3.1. Introduction

Poly(3,4-ethylenedioxythiophene) polystyrene sulfonate (PEDOT:PSS) is a polyelectrolyte complex, in which the conducting PEDOT cation is polymerized in the presence of the non-conducting PSS anion that cannot be isolated from it. The long chains of PSS are thought to surround the rigid PEDOT resembling a micellar structure forming a very stable microdispersion in water. The PSS polymer chains reduce conductivity by screening and limiting charge delocalization to single PEDOT chains, and reducing variable range hoping (quantum-mechanical tunneling) of charge carriers from one chain to another. PSS will also induce defects and kinks into the PEDOT chain, producing mid-gap levels and other charge carrier traps. Moreover, it increases entanglement and inhibits the polymer from forming crystalline domains. A reduction in the detrimental effects of PSS on the conductivity and morphology of PEDOT should be beneficial to the performance of PEDOT:PSS containing optoelectric devices such as hybrid solar cells (HSCs). The as-prepared conductivity of films made from PEDOT:PSS dispersions (Clevios^{TM} PH1000) are low, below 1 S/cm at room temperature. Because of this, researchers have sought to reduce the influence of PSS and its impact on PEDOT chains. Two techniques that have proven effective are addition of co-solvents to the aqueous PEDOT:PSS solution, and post-treatment of the deposited films with a solvent or through chemical vapor deposition. These different techniques result in vastly different changes in the properties of the PEDOT:PSS films and their effect on PEDOT:PSS/planar-Si HSCs.

3.1.1. PEDOT:PSS additives / Co-Solvents

In 2002, Kim *et al.*[75] increased the conductivity of PEDOT to 80 S/cm by adding dimethyl sulfoxide (DMSO) to the PEDOT:PSS solution. Since then, much research has been devoted to further increase the conductivity and to understand the fundamental processes causing the increase. Additives that have successfully increased the conductivity include salt solutions, surfactants, acids, and polar organic or high dielectric solvents. The additives used and their effectiveness are listed in Table 3.1

[‡] This section is made from one of my publications: McGillivray Donald, Thomas Joseph P., Abd-Ellah Marwa, Heinig Nina F., Leung K. T., 2016, 8, pp 34303-8. Copyright (2016) by ACS Applied Materials and Interfaces.[137]

Table 3.1: Conductivity enhancing co-solvents added to PEDOT:PSS solutions

	Additives	**Conductivity (S/cm)**	**Reference**
Salts	1-butyl-3-methylimidazolium tetrafluoroborate	136	(76)
	1-butyl-3-methylimidazolium bromide	118	(76)
	Zwitterions	94	(77)
	InI_3	191	(77)
	$CuBr_2$	187	(78)
Surfactants	Sodium dodecyl sulfonate	80	(79)
	Zonyl FS-300	47	(80)
Point polar organic solvents	Dimethylformamide	30	(75)
	Sorbitol	91	(81,82,61)
	Diethylene glycol	10	(63)
	Ethylene glycol	-	(83)
	Glycerol	-	(84)
	Methanol	70	(85)
Acids	Acetic acid	200	(86)
	Propionic acid	-	(86)
	Hydrochloric acid	-	(86)
	H_2PtCl_6	1094	(87)
	Sulfuric acid	100	(88)
Base	NaOH	10	(89)

Organic/inorganic salts have good ionic conductivity and affinity for conducting polymers. They are often used in conjunction with conducting polymers in polymer-based electrochemical devices. The ions remain imbedded in the conducting polymer after annealing, acting as a dopant that adds charge carriers to PEDOT chains.[76] This can also be problematic since the ions could diffuse under an electric field and deteriorate the performance of the device. Ouyang *et al.*[78] found that the increase in conductivity was related to the softness parameter of the cation (soft Lewis acid), which is related to the binding energy of the metal cation to the PSS anion. The cation can interact with both the positively charged PEDOT and negatively charged PSS, screening the coulombic attraction between them and swelling the micellar particles in solution thereby allowing for rearrangement of PEDOT into a more linear confirmation. The lower affinity of PSS to PEDOT after the addition of ionic liquids can facilitate PSS being freed from the globular polymer network resulting in a lower concentration of PSS in the final film.[77]

Similarly, acids can induce PEDOT:PSS phase separation resulting in increased conductivity through protonation of PSS. $PSS^- + H^+ \rightarrow PSSH$. An acid with low pKa can give rise to a higher conductivity, assuming that other properties that could have an effect such as viscosity are the same.[90]

Surfactants added to the solution can also induce a phase separation and a change in the linear conformation of PEDOT but only up to a certain point, because they tend to be bulky and insulating and they cannot be removed after film deposition. However, their primary function is to increase the adhesion of the film onto the substrate and to enhance the overall flexibility.[76]

Polar organic solvents used as co-solvents allow for charge screening between the cationic PEDOT and its surrounding anionic PSS. They can be less bulky and more easily penetrable between the PEDOT and PSS ions than some of the other reagents discussed. The decreased coulombic attraction can facilitate de-entanglement of PSS and will be discussed below.

3.1.2. Post-Treatment

Post-treatment is a technique of increasing the conductivity of PEDOT:PSS films after deposition usually by immersing the film in a solvent. Similar types of reagents can be used for post-treatment as the additive method mentioned above. The treatment of films after deposition can cause a greater change in morphology and conductivity through swelling of the polymer film, doping, or PSS removal. Moreover, post-treatment has the advantage that there are no concerns regarding the solubility or phase separation of the polyelectrolyte complex found in the additive method.

Post-treatment can have a large effect on the film conductivity. Films treated with methanol had a conductivity of 1362 S/cm[91] compared to only 69.7 S/cm when methanol was added as co-solvent.[85] Similarly, treating with sulfuric acid had led to a remarkably high conductivity of 2400 S/cm[92] compared to only 100 S/cm when used as a co-solvent.[88] It also has the benefit that repeated treatments can be performed to get further gains. A very high conductivity can be achieved when the films are treated with acids like sulfuric acid and oxalic acid (1900 S/cm), malonic acid (2210 S/cm) and methansulfonic acid (2870 S/cm).[90] However, their concentrations have to be monitored or the acids can easily induce defects such as micropores at the interface or pinholes in the film.

The proposed conductivity enhancement mechanisms reported in the literature can be broken down into charge screening between PEDOT and PSS (using polar organic solvents, surfactants); or neutralizing PSS and doping PEDOT (using ionic liquids, acids). In this chapter, polar organic solvents

ethylene glycol and methanol are studied to determine the effects of vapor pressure and dielectric constant on the films. Parameters including reduction of film thickness, change in absorbance, swelling, conductivity, and morphology that affect solar cell performance were carefully examined.

3.2. Experimental Details

The HSCs were prepared on 1×1 cm^2, n-type (100) phosphorus-doped silicon substrates with a resistivity of 1-2 Ω cm and thickness of 200 μm (Virginia Semiconductor Inc.). The substrates were cleaned by sonication in acetone, isopropyl alcohol and washed with filtered high-resistivity water (18.2 MΩ-cm). The native silicon oxide layer on the wafers was removed with hydrofluoric acid (2 vol%) and then allowed to regrow on the polished side in air for 2 hours. Aluminum is used as the anode because of the good alignment of the Fermi level of Al with the conduction band edge of n-type silicon. To form the back electrode, Aluminum was sputter-coated with a magnetron sputtering system (EMS575X) immediately after the HF treatment to limit the oxide layer and to form a consistent ohmic contact on the Lambertian textured back side of the wafer.[‡]

3.2.1. PEDOT:PSS Film Formation:

Spin coating is a simple method of producing uniform films of a few nanometers to a few micrometers by applying a dispersion or "ink" to the substrate, spreading it by spinning onto the substrate and then drying the molecules on the substrate (Figure 3.1). The ink discussed here is PEDOT:PSS (Clevios™ PH1000) with the addition of 7 wt% ethylene glycol and 0.25 wt% florosurfactant (Zonyl FS-300) to increase its conductivity and wettability, respectively, unless otherwise noted.[80,93] The centripetal force combined with the surface tension of the ink removes excess solution leaving a uniform film. There are a number of considerations when spin-coating PEDOT:PSS onto silicon wafers, such as the spin speed and time, and ink application via static or dynamic deposition, all of which could affect the device performance. One major consideration is the film thickness (t), which is related to the spin speed (w) by $t \propto 1/\sqrt{w}$, as shown in Figure 3.1 a) inset. The drying rate related to the spin time and speed is important to the π-to-π stacking and crystallization of the films. A high drying rate can quench molecular motions into a thermodynamically unfavorable configuration, limiting the π-to-π stacking and ultimately

[‡] A Lambertian textured surface is patterned with rough, micrometer-sized features that result in the diffuse scattering of light and aid in the light trapping ability of solar cells through the total internal reflectance.[161]

interchain transport. After spin coating for 2 minutes at 6000 RPM, the polymer still contains a degree of moisture. The film is in a swollen state, with a thickness about 4 times its final thickness, which decreases with the continued evaporation of water (Figure 3.1 b)). Because of this, the films were left at room temperature for 10 minutes before annealing at 110°C to drive off any remaining moisture. Figure 3.2 shows a representation of this process.

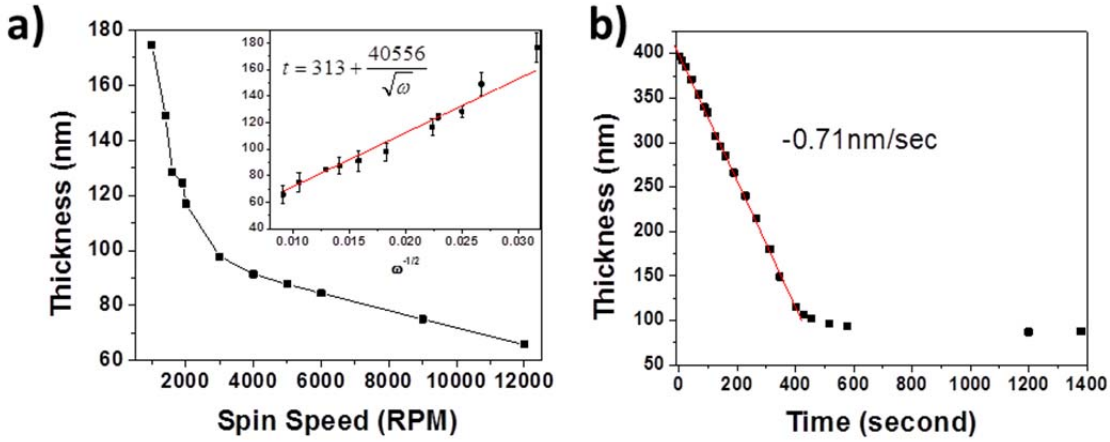

Figure 3.1: (a) Film thickness of PEDOT:PSS (Clevios PH 1000) film (a) as a function of spin speed and (b) as a function of drying time. The inset of (a) shows the inverse square-root relation of the spin speed with thickness, while (b) shows the reduction of swelling and relaxation of film with evaporation after spin coating.

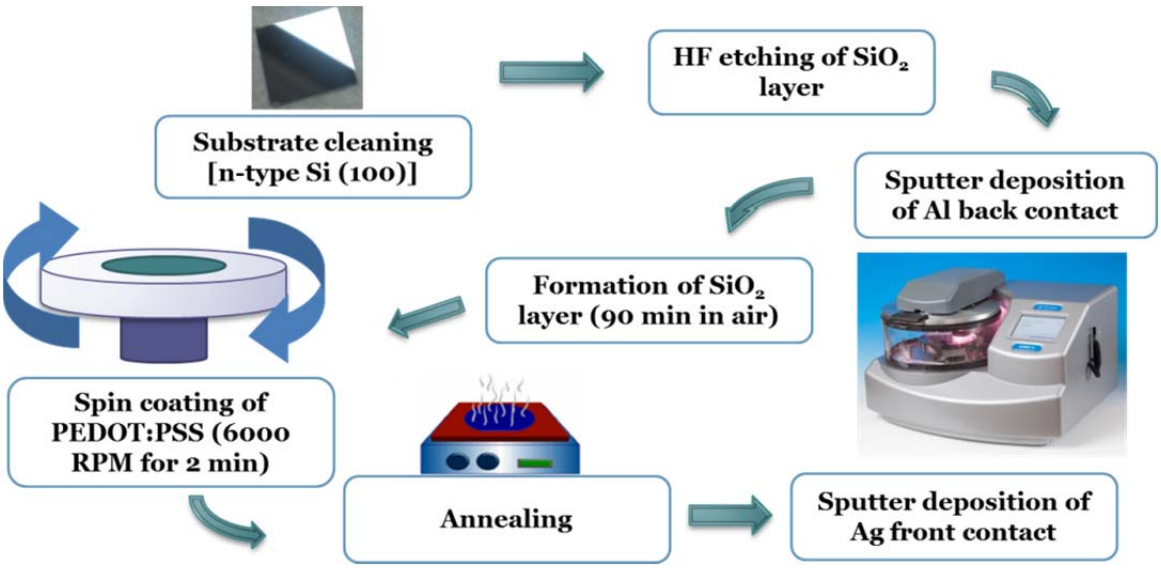

Figure 3.2: Typical steps in fabricating a HSC.

Post-treatment was done by adding 80 µL of a binary mixture of methanol (Sigma Aldrich, ≥99.9% purity) and ethylene glycol (VWR, ≥99.0% purity) with known volume fractions onto the PEDOT:PSS film. The solution was left on the surface for 2 minutes to insure penetration into the film and stop the Marangoni eddies[‡] that result from mixing solutions with a large difference in surface tension and vapor pressures. After spin coating at 6000 RPM for 2 minutes, the substrate was placed on a hot plate for 10 minutes.

10×10 mm^2 quartz substrates (SPI Supplies), 1 mm thick, were used for UV-vis experiments. They were prepared identically as the Si substrate. Absorbance/transmittance measurements were done by using a Perkin Elmer Lambda-1050 UV-Vis spectrometer, with the baseline obtained on the pristine quartz substrates before the film was deposited. A Filmmetric F40-UV thin film analyzer was used to collect reflectance spectra and to determine the film thickness, which was also verified by using a KLA Tencor P-6 profilometer. Conductivity measurements were done on glass substrates using the four-point

[‡] The Marangoni effect refers to turbulence in a mixture caused by differences in surface tension of two fluids. Gradients arise since the liquid with a higher surface tension will naturally tend to lower its total energy by bonding with the surrounding liquid, causing mass transfer from regions with low surface tension. The effect is opposed by gravity or a temperature gradient causing turbulence until equilibrium is achieved likely with the evaporation of the lower surface tension fluid. This is the effect that causes “wine tears” in one’s favorite alcohol.

probe method in a van der Pauw configuration (Ecopia HMS-5300). Raman spectra were collected with a 785 nm laser in a Bruker Senterra spectrometer. AFM images were collected by using an Asylum Cypher AFM in AM/FM mode unless otherwise noted.

3.3. Results and Discussion

3.3.1. Ethanol/Methanol Post-treatment

Co-solvents, such as ethylene glycol (EG) or methanol (MeOH),[85,91] have been used to improve the performance of PEDOT:PSS based organic solar cells. [16,94,95] Post treatment shows similar enhancements using similar solvents. [68,69] For both co-solvent and post-treatments, the proposed mechanism for enhancement is through phase segregation of PEDOT and PSS caused by charge screening from the solution and a reduction of the coulombic attraction between them.[69] This reduced interaction allows for rearrangement of the PEDOT segments into a more linear conformation and a greater delocalization of charge. The mechanism behind the phase segregation is not yet well understood. Both methanol and EG post-treatments show conductivity enhancements of the same order of magnitude and similar mechanisms have been proposed. [83,96,97] It is, however, unclear why these different solvents, with vastly different properties (Table 3.2), have produced the same result on the conductivity, while water, which shares similar properties, does not. In this Chapter, the physical and electrical properties of films treated with different solvents are examined to elucidate the mechanism that causes the observed changes and in their application to hybrid solar cells.

Table 3.2: Properties of solvents used as co-solvents and for post-treatment of PEDOT:PSS solution.

	Methanol	**50 vol% EG/MeOH**	**Ethylene Glycol**	**DMSO**	**Water**
Density (g/cm^3)	0.791	0.985	1.113 (1.04 @ 117^{o}C)[a]	1.100	0.998
Viscosity (mPa*s)	0.587	3.824	20.806 (2.06 @ 100^{o}C)[a]	1.996	0.890
Molar Volume (cm^3/mol)	40.482	47.357	55.757	-	18.05
Dielectric Constant	32.6	-	37.7	47	78.54
Boiling Point (^{o}C)	64.6	78.7	195	189	100
Vapor Pressure (kPa at 20^{o}C)	13.02	-	0.008	-	2.3
Dipole Moment (μ Debye) [b]	1.69	-	2.38	3.96	1.85

a. Vitoratos, E.; Sakkopoulos, S.; Dalas, E.; Paliatsas, N.; Karageorgopoulos, D.; Petraki, F.; Kennou, S.; Choulis, S. a. Thermal Degradation Mechanisms of PEDOT:PSS. *Org. Electron. physics, Mater. Appl.* **2009**, *10* (1), 61–66. [98]

b. CRC handbook of chemistry and physics; a ready-reference book of chemical and physical data, 85th ed., 2004-2005. (2004, 12). *Scitech Book News, 28*

UV-vis and thickness measurements were conducted on 85-nm-thick films before and after the post-treatment in order to determine the extent of PSS removal and the reduction in the film thickness, respectively (Figure 3.3a). The removal of PSS from PEDOT:PSS films can be monitored by the intensity reduction of the absorption band at 193 nm, associated with the benzene rings of PSS, before and after post-treatment (Figure 3.3b).[16,82] The greatest reductions in the film thickness and in the PSS absorption band intensity have been found for films post-treated with a 1:1 MeOH:EG mixture, which removes 51.7 ±2.8% of the film. For comparison, water reduced the thickness by 11.3 ± 4.3%. Experiments with consecutive post-treatment cycles on the same film were also attempted. The second cycle reduces ~10% of the thickness, after which only a slight decrease can be detected, indicating a limit to how much material can be removed through post-treatment.

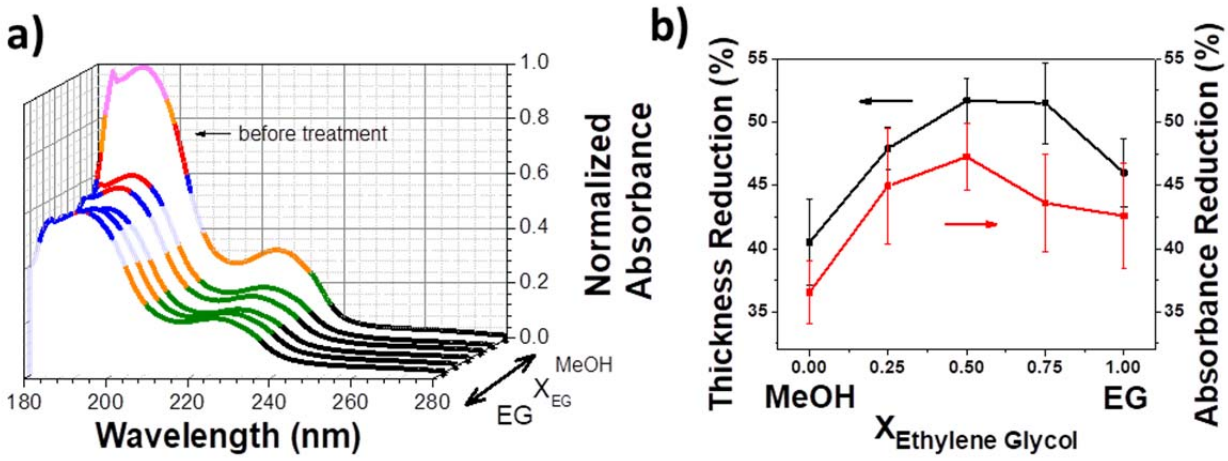

Figure 3.3: a) UV Absorbance spectra of PEDOT:PSS thin film treated with different MeOH/EG ratios. b) Percent reduction of film thickness and relative intensity reduction of the PSS absorption band at 195 nm for MeOH-EG solutions with different MeOH/EG ratios.

The conductivity was also examined and found to be greatly enhanced from 1 S/cm to 637 S/cm (±58 S/cm) with the addition of co-solvent to the stock PEDOT:PSS solution. It further increased, by over a factor of two, after post-treatment. Evidently, post-treatment using the MeOH-EG binary mixture leads to the film conductivity enhancement that follows a similar trend as the UV-vis and film thickness, with the highest recorded value of 1431 S/cm (the average was 1334 ±129 S/cm) found for a 1:1 mixture (Figure 3.4 a). A considerable increase in the conductivity by at least 10% relative to those of single-

solvent post-treatment is obtained by the post-treatment using the 1:1 binary mixture. The conductivity does not improve notably with consecutive treatments so only one cycle was needed.

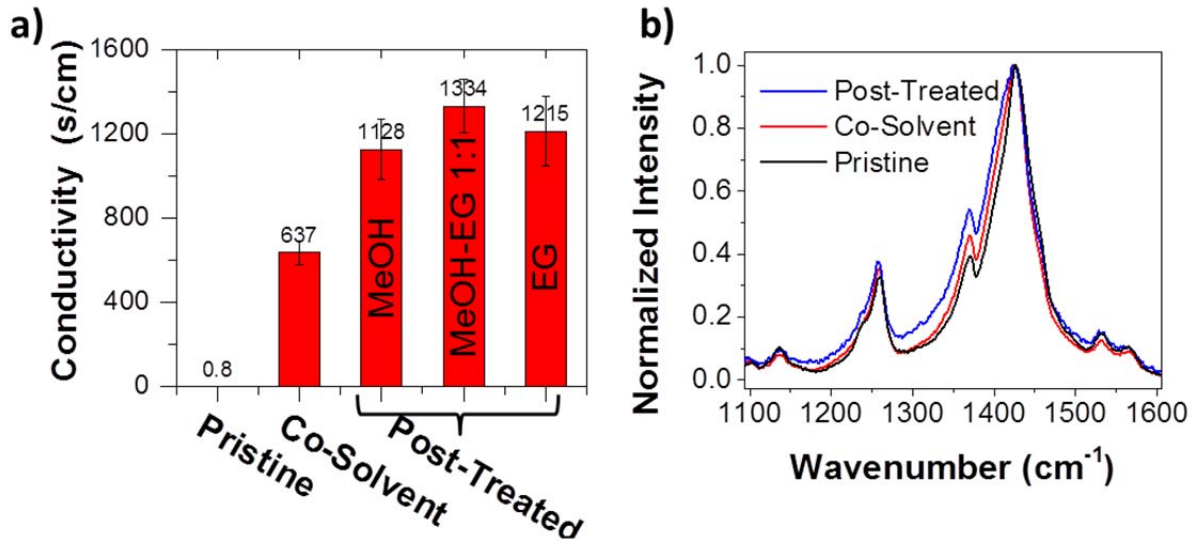

Figure 3.4: (a) Comparison of conductivities of the pristine, co-solvent-added and post-treated PEDOT:PSS films. (b) Raman spectra showing the structural changes of PEDOT to a more quinoidal conformation with post-treatment.

Raman spectroscopy is very sensitive to structural changes in polymers and is useful in studying secondary doping in conjugated polymers.[99] The vibrational modes of PEDOT and PSS were followed using a 785 nm excitation line for pristine, co-solvent-added and post-treated films (Figure 3.4 b). The 785 nm band was chosen for its proximity to the bi-polaron electronic transition of PEDOT at 850 nm, which is enhanced by resonance effects.[100] Bands for PEDOT lie mostly in the 1100 – 1600 cm^{-1} range. The most intense band located near 1425 cm^{-1}, to which the spectrum is normalized, is assigned to the C_α=C_β symmetric stretching mode, while the two weaker bands at 1532 cm^{-1} and 1563 cm^{-1} correspond to the C_α=C_β asymmetric stretching modes.[101] The bands at 1368 cm^{-1} and at 1256 cm^{-1} are attributed to the C_β–C_β stretching and C_α–C_α inter-ring stretching, respectively.[99] Broadening of the 1425 cm^{-1} band is evident with the addition of co-solvent, and further broadening is found with post-treatment. The relative intensity of the 1368 cm^{-1} band increases with the addition of a co-solvent and then again with post-treatment. We also observe a slight intensity increase and a red shift for the C_α–C_α inter-ring stretching mode at 1256 cm^{-1}. These changes are often associated with a change in the linear structural arrangement from the benzoidal conformation to a more quinoidal-like conformation.[99]

Unlike doping, the post-treatment methods are unlikely to provide any additional charge carriers, and they produce only a change in structural arrangement that leads to stable electronic redistribution, commonly referred to as secondary doping. The higher conductivity is attributed to the presence and greater delocalization of quasi particles, polarons and bi-polarons.[16] As mentioned above these free charge carriers are also detectable in the IR region of the absorbance spectra discussed below. There was not a large difference in the Raman or IR region when comparing methanol to ethylene glycol, or when multiple post-treatments were attempted, indicating that all solutions induce a similar electronic change.

The loss in thickness and reduction of PSS bands in the absorption spectrum provide evidence for the removal of hydrophilic PSS from the film. This was confirmed by Raman and ATR-FTIR on the white precipitate that could be seen with a microscope when the post-treatment wash solution was evaporated off (Figure 3.5a). The Raman done on these features did not detect any discernible PEDOT peaks. The ATR-FTIR on them shows a sharp PSS absorption band without any characteristic bands of PEDOT (Figure 3.5b). The main absorbance peaks for PSS at 1167 and 1125 cm^{-1} represent asymmetric stretching vibrations while those at 1035 and 1005 cm^{-1} correspond to the symmetric stretching vibration of $–SO_3^-$ pendent. Peaks at 830, 772, and 670 cm^{-1} can be attributed to the =C–H out of plane deformations while the peaks at 3048 and 3186 cm^{-1} are assigned to the aromatic =C-H stretching mode. The peak at 2920 cm^{-1} belongs to alkyl C-H stretching.[102] Absent from the PSS precipitate are PEDOT peaks, with the features at 1529, 1413 and 1368 cm^{-1} corresponding to the aromatic –C=C– component in the thiophene backbone.[99] The bands at 1154, 1118, and 1060 cm^{-1} belong to C–O–C of the dioxane component, while the features at 945, 861, and 707 cm^{-1} correspond to C–S stretching mode of the thiophene ring.

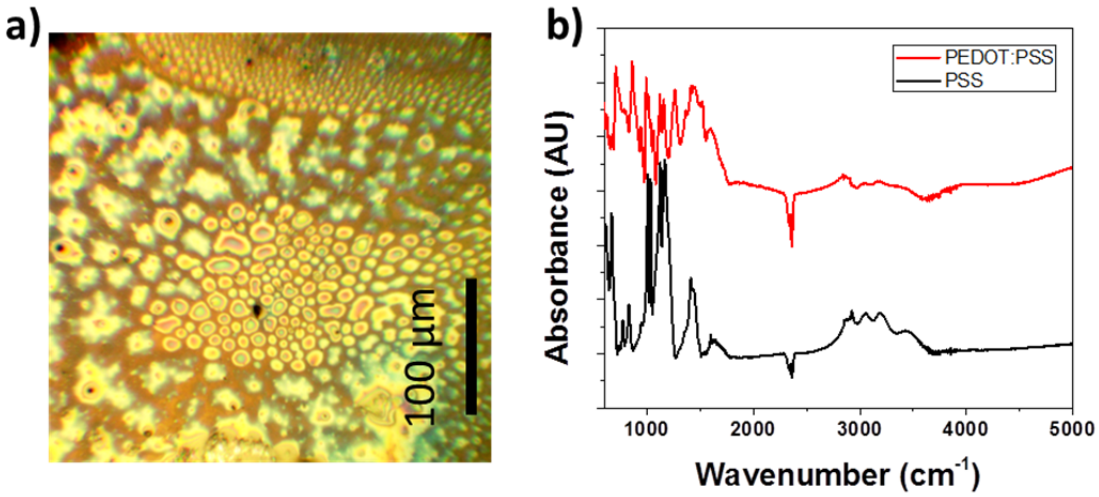

Figure 3.5: (a) Optical microscope image of the PSS precipitates obtained after the methanol-ethylene glycol solution is evaporated off. (b) ATR-FTIR spectra of the PEDOT:PSS film and the PSS precipitate desorbed from the film.

3.3.2. Film Morphology

Morphological changes can be observed among different films with AFM (Figure 3.6). The average RMS surface roughness is seen to increase from 0.96 ± 0.08 nm, to 1.56 ± 0.18 nm, and to 1.81 ± 0.24 nm for the respective pristine, co-solvent-added and post-treated films. At the same time better defined domains appear. This evolution is especially evident in the frequency images, depicting the third fundamental cantilever frequency in tapping mode, which are much more surface sensitive to the soft PSS (bright network) than the hard PEDOT (dark domains)(see appendix 1).[103] Evidently, the domains become larger and less elongated with the addition of co-solvents, and even more so with the post-treatment. The average area of the domains increases from 21.9 nm^2 to 35.2 nm^2 to 183 nm^2, while the aspect ratio increases from 0.308 to 0.312 to 0.428 for the respective pristine, co-solvent-added and post-treated films.

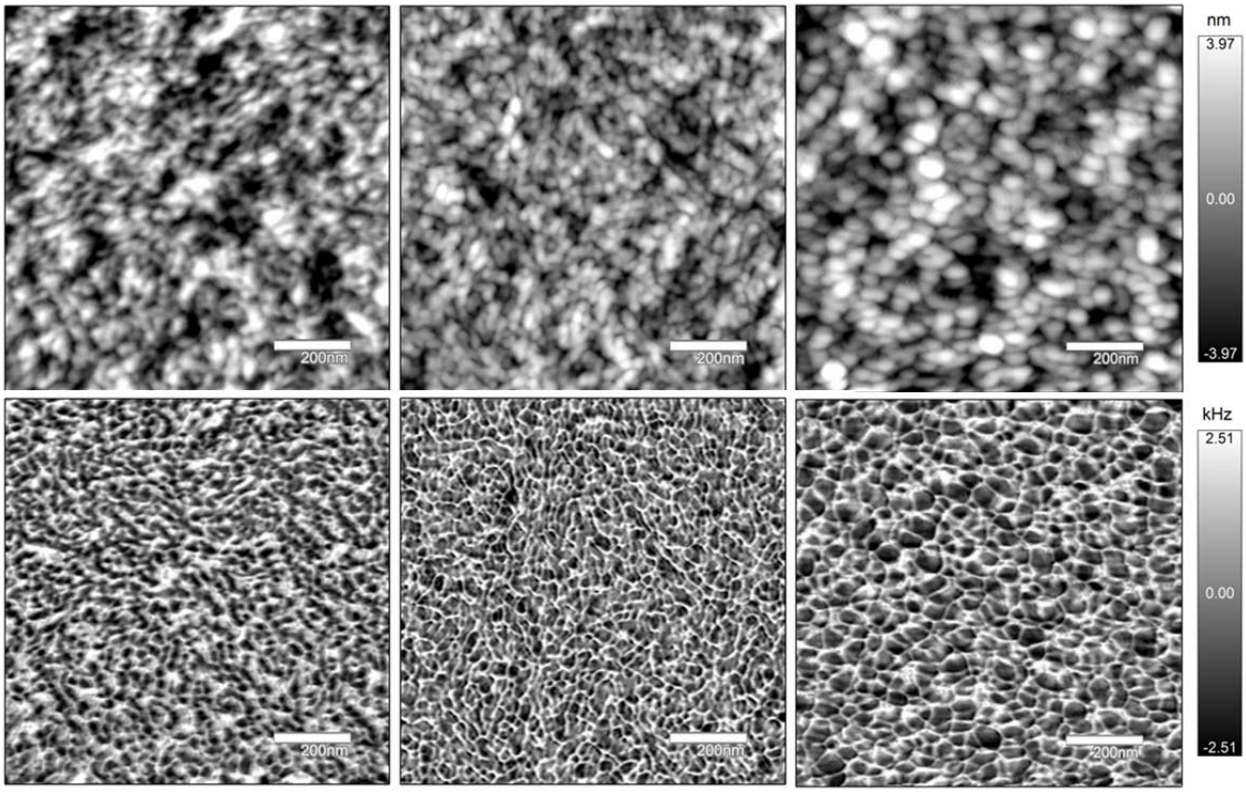

Figure 3.6: AFM images (Topography - top row, Frequency - bottom row) of pristine (left column), co-solvent-added (middle column) and post-treated films (right column), showing the segregation of PEDOT and PSS with secondary doping and the formation of nanodomains.

AFM investigations performed on films before and after post-treatment at the same spot were remarkably similar. Figure 3.7a) shows the area adjacent to a scratch on the film before and after post-treatment while Figure 3.7b) depicts a 33% decrease in the film thickness after the post-treatment. The films have outcrops of agglomerated PEDOT:PSS on the surface, a result of not filtering the solution, but these outcrops provide easy identification of the same location after post-treatment. Along the edge of the scratch is the accumulation of PSS. The RMS roughness of the film increased after treatment (from 1.4 to 1.8 nm) but the standard deviation decreased from 1.3 to 1.2 nm, indicating that after treatment the films were rougher over short lengths but more uniform over longer scales). Features that were present before could also be identified after post-treatment, despite many reports from other groups that a high concentration of PSS lies at the surface of the PEDOT:PSS film. [63,75,98,91] The similarities of the before and after images indicate this is not the case. The reduction in thickness is the cause of PSS being removed uniformly throughout the film.

AFM on the white PSS deposits obtained from evaporation of the wash solution shows that they are extraordinarily smooth and different from the bulk film, with a RMS roughness of 0.23 nm, which can be expected for a homogeneous polymer.[104] These results indicate that post-treatment leads to the disentanglement of PSS from the films remarkably without the removal of much PEDOT.

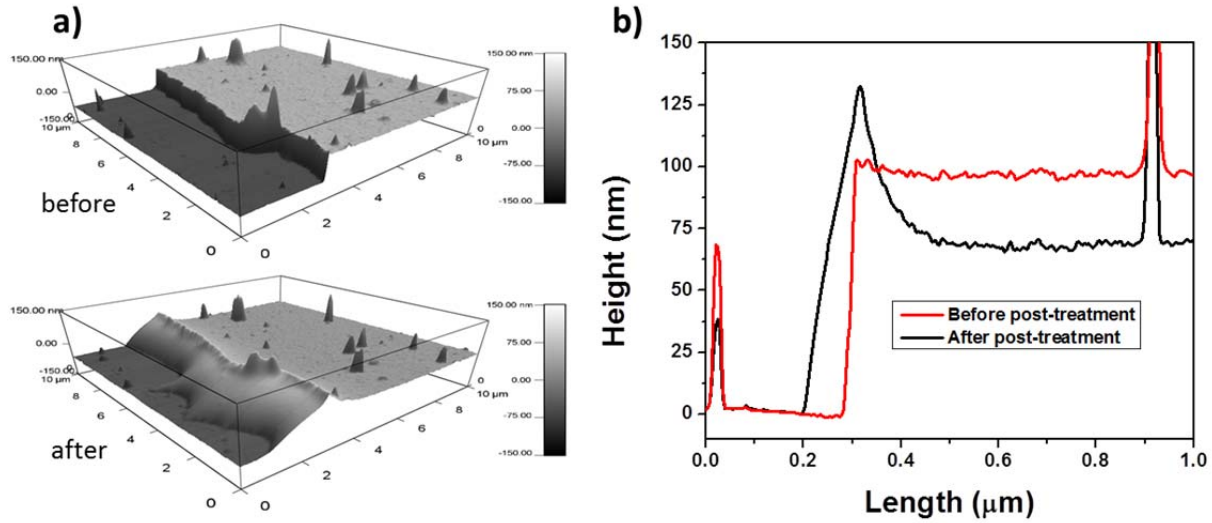

Figure 3.7: a) AFM perspective images for a scratched area of the PEDOT:PSS film (10×10 μm^2) before (upper) and after post-treatment (lower). The smooth material along the edge for the post-treated film is the accumulation of PSS. b) Line scans along the films showing a 33% decrease in height (thickness) for the post-treated film .

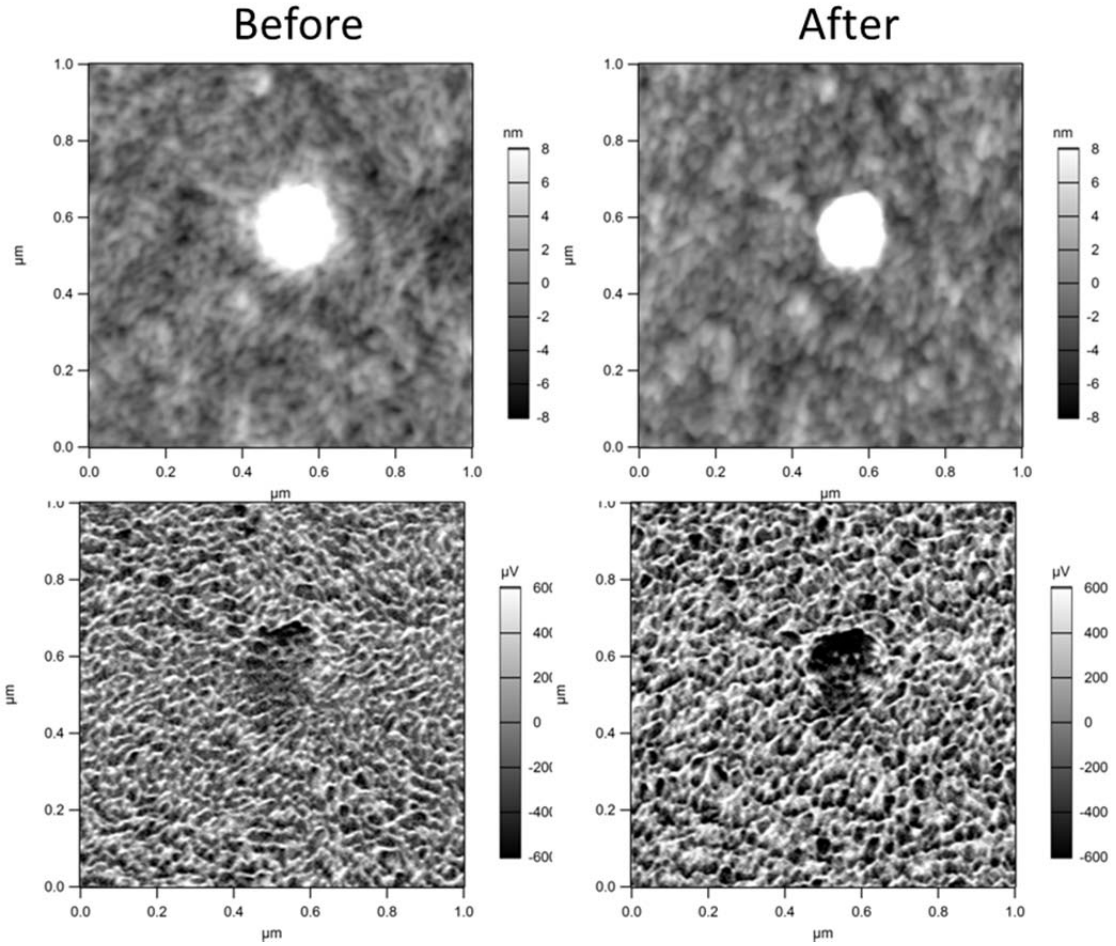

Figure 3.8: Amplitude (left) and phase (right) AFM images of an 1×1 µm^2 area before (upper row) and after post-treatment (lower row). Center feature is an agglomeration of PEDOT:PSS.

PEDOT:PSS films on silicon can be easily removed by agitation in a solution of water. What remains is a thin hydrophilic residue on silicon. Figure 3.9 shows the residue on the silicon surface before and after post-treatment at the same location where the film was removed. The surface is significantly cleaner after post-treatment with the RMS decreasing from 0.9 nm to 0.6 nm following the removal of PSS but major features are still identifiable. These features are isolated PEDOT:PSS micelles described above and they stand apart from the silicon background and PSS residue appearing as dark regions of low energy dissipation. Particle analysis selected for these features revealed that the average height reduced by a third, from 3.0 to 2.1 nm, (Figure 3.10 a) and the volume decreased from 5030 to 4040 nm^3, while the average area and aspect ratio increased from 1520 to 1760 nm^2 and from 0.63 to 7.3, respectively. These flat pancake-like structures are consistent to STM studies by Nardes *et al.*[105]

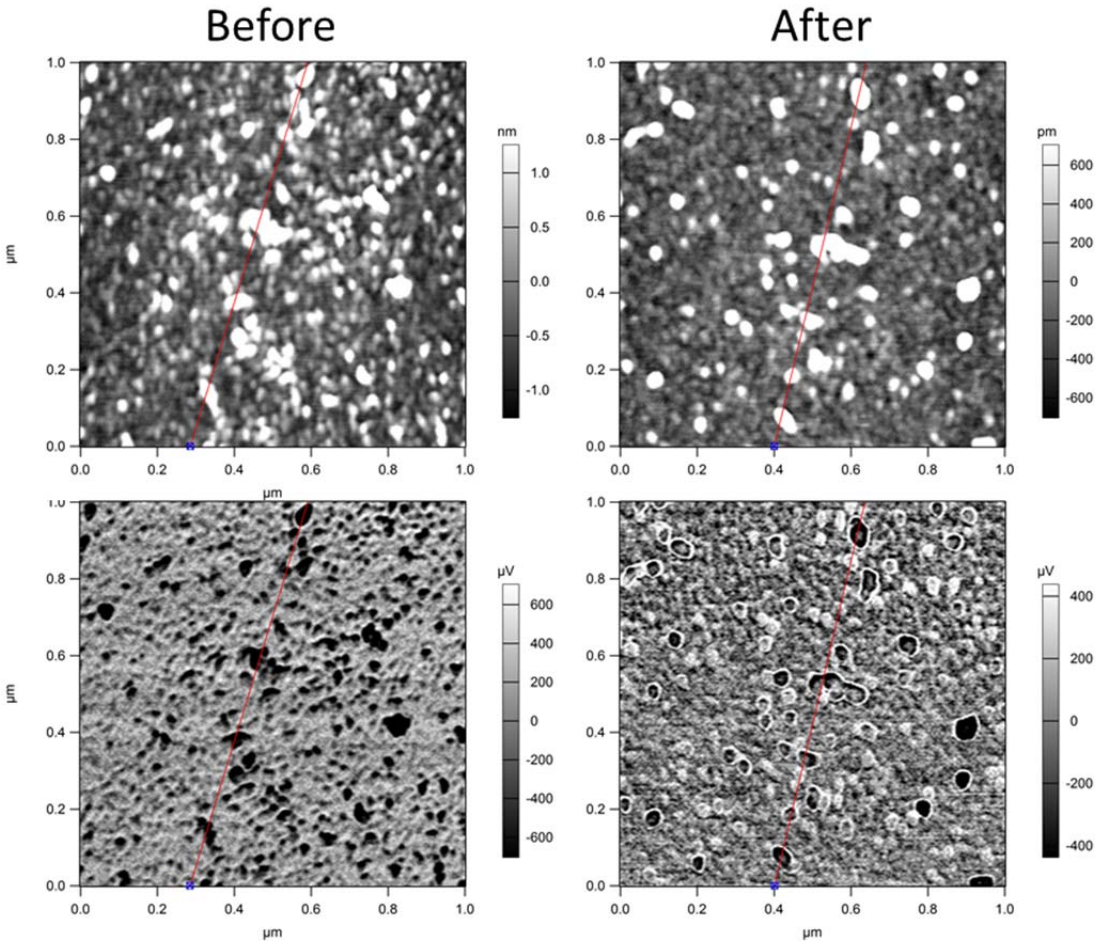

Figure 3.9: a) 1 µm x 1 µm topography AFM images (left) and energy dissipation maps (right) of the PEDOT:PSS residue on silicon before and after post-treatment (top and middle rows, respectively).

This compression and rounding out of PEDOT:PSS micelles are indicative of the rearrangement of the internal structure as a result of post-treatment and we can evaluate chain alignment with respect to the substrate. Given that the PEDOT:PSS weight ratio of Clevios PH1000^{TM} is 1:2.5 and the molecular weights range from 1000 to 2500 for PEDOT and from 75000 to 400000 for PSS, their chain lengths are expected to be 3-7 nm and 250 – 800 nm respectively.[52,104,106] The length of PEDOT and its linear conformation, which is supported by its stiff conjugated bonding and the change in Raman spectra, entails that the PEDOT chains lie parallel to the substrate and are stacked by one or two layers to give rise to a 2 nm high feature. The confinement of PEDOT chains in two dimensions, horizontal to the substrate plane, increases the density of conducting chains and π-to-π orbital overlap within the micelle schematically shown in Figure 3.10b).

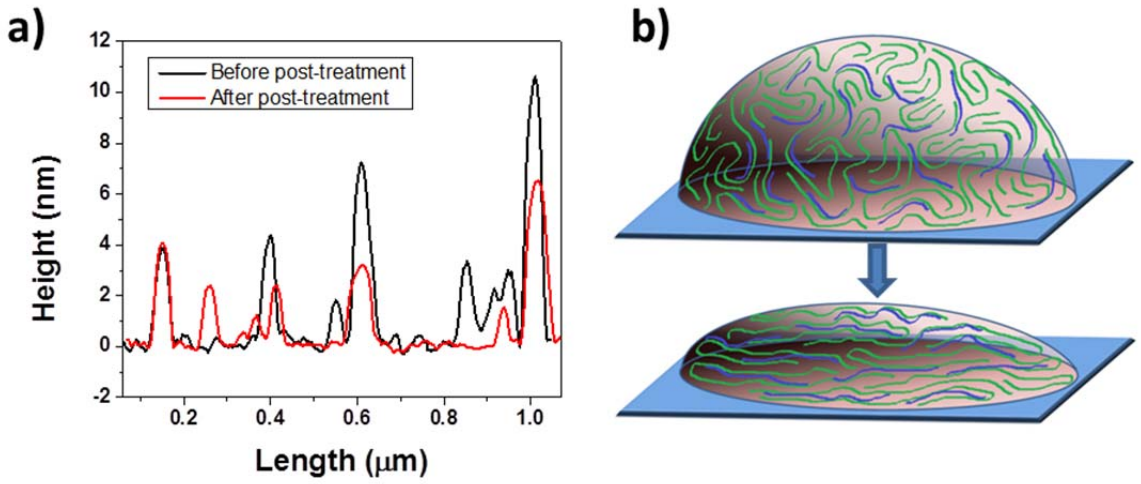

3.10: AFM height line scan of micelles before and after post-treatment. c) Schematic representation of the change in micellar domain after post-treatment with the PEDOT chains lying parallel to the surface.

3.3.3. Effect of Solvents on Post-treatment

A way to induce molecular motion in the chains and to change the rheological properties, without heating, is by increasing the free-volume through swelling. This will allow the chains to undergo structural relaxation toward equilibrium, and to change to a more linear conformation and cause the preferred orbital overlap of the thiophene rings. Hydrophilic PSS readily absorbs water and polar organic solvents into the film, saturating the sulfonic groups and causing them to swell. The degree of swelling of the annealed films was measured by AFM equipped with a micro-fluidic cell. A trench was cut in the film, and the film was measured initially in air under normal conditions and then placed in the cell that was filled with water or an EG-MeOH mixture to measure the increase in swelling. From the swelling experiments done by AFM in solution, the film thickness was found to increase remarkably 8.6 times its original thickness in water and only 3.7 times when in an EG-MeOH mixture (Figure 3.11). The lower swelling in EG-MeOH is due to the removal of PSS from the matrix and to the increased van-der-Waals interaction between the non-soluble PEDOT chains. An analogy would be the Mullins effect with reinforcing fillers that make elastomers stiffer, the EG-MeOH would increase the concentration of PEDOT chains acting as a reinforcing filler.

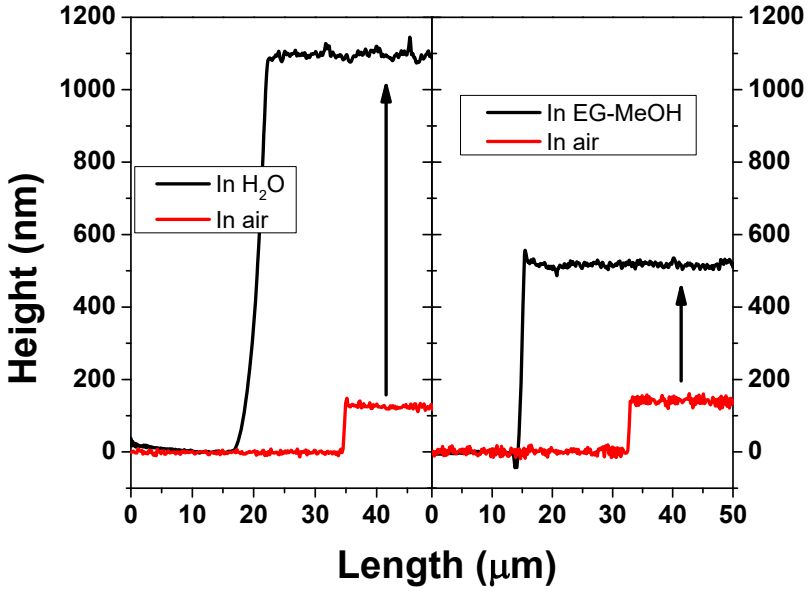

Figure 3.11: AFM line scans of PEDOT:PSS films before and after swelling in water (left) and an ethylene glycol-methanol mixture (right).

The large degree of swelling and the deviation from ideal behavior with a 1:1 MeOH-EG mixture, observed from conductivity measurements, thickness measurements, UV-Vis spectroscopy and Raman spectroscopy, are the result of lower viscosity than pure ethylene glycol and higher dielectric constant and charge screening ability than pure methanol.[107] The mixture readily interacts through hydrogen bonding with the sulfate group of PSS or with the oxygen atoms of the PEDOT monomer. The charge screening effect between PEDOT and PSS reduces the interchain interaction and the activation barrier for the reorientation of the respective chains. The binary mixture has been shown to form a nearly regular solution at ~1:1 MeOH-EG at room temperature,[108] as is commonly found when alcohols are dissolved in non-polar solvents. This mixture is, however, less stable with possible partial clustering, and that the hydrogen bond strength increased with ethylene glycol concentration, MeOH-MeOH < MeOH-EG < EG-EG[108,109] similar to water-EG mixtures.[110] The non-zero enthalpy of mixing is expected to increase the segregation between PEDOT and PSS, allowing the bulkier ethylene glycol molecule to intercept and obstruct the ionic attractions and to further promote chain reorientation. There are also significant Marangoni eddies when the EG-MeOH solution is added onto the polymer surface because of the mixture of high and low vapor pressures. The agitation likely further disentangles the PSS, allowing PSS to move around the PEDOT more so than any pure solvent.

Unlike PEDOT, the PSS component is highly soluble, allowing the chains that are not entangled in the matrix to be readily removed with the solution, which accounts for a small reduction in thickness as observed even with water. The much shorter PEDOT chains act as a molecular binding agent pinning the PSS chains at different points, stiffening the films, similar to the effect of cross-linking agents. Thickness studies were done with sulfuric acid and NaOH to examine the effect of acidity on the removal of PSS, as it is expected that the neutralization of PEDOT:PSS would reduce their attraction and result in a large decrease in the film thickness. However, the observed decrease, for both acid and base, was similar in magnitude to that for pure water (~12%), indicating that it had little effect on the removal of material. The reason that the oxygenates were so much more effective than water has to do with their greater molecular volume and the fact that they can be easily electronically polarizable (with higher London dispersion forces), despite not necessarily having a large orientational polarizability especially in the case of ethylene glycol. The effectiveness of oxygenates at removing PSS is the cause of the smaller swelling seen in the solution-AFM measurements and those chains not contributing to the film distortions.

3.3.4. Cell Performance

A collection of 72 HSCs have been constructed and their performance data are analyzed to provide relevant comparison between treatments shown in Figure 3.12 with the top performing cells. Evidently, the V_{OC} for the cells with post-treated PEDOT:PSS films (average 0.49 V) is found to be slightly higher and with a smaller distribution than those for the cells with co-solvent-added films (0.48 V) and pristine films (0.35 V). The fill factor is also consistently higher after post-treatment. The swelling and chain rearrangement during post-treatment allows for the reduction of defects in the film and at the PEDOT:PSS/n-Si interface. This leads to greater charge transfer across the junction and the larger average V_{OC} and fill factor.

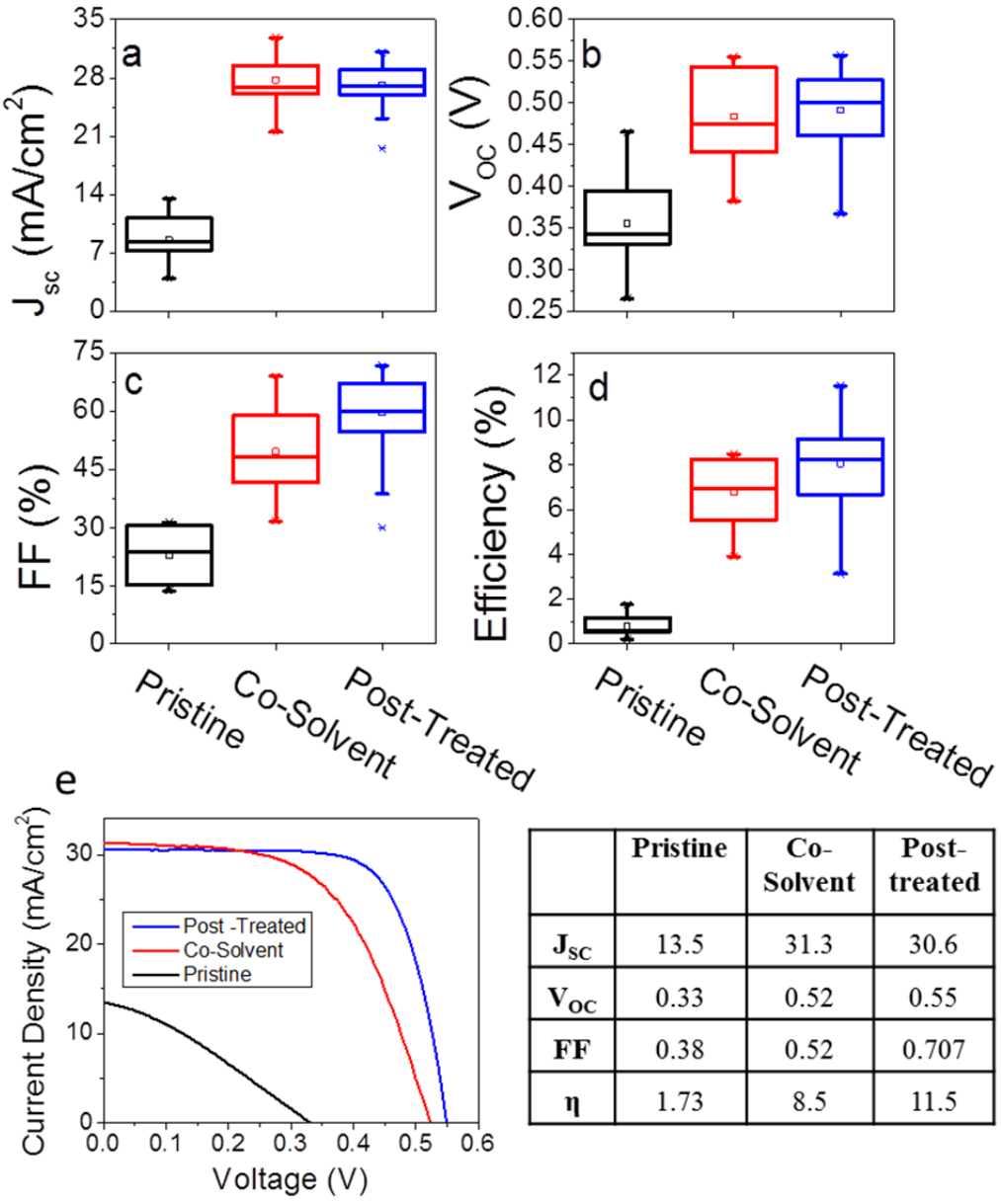

	Pristine	Co-Solvent	Post-treated
J_{SC}	13.5	31.3	30.6
V_{OC}	0.33	0.52	0.55
FF	0.38	0.52	0.707
η	1.73	8.5	11.5

Figure 3.12: Box plots for (a) short-circuit current J_{SC}, (b) open-circuit voltage V_{OC}, (c) fill factor FF, and (d) photoconversion efficiency for the 72 HSCs obtained with pristine, co-solvent-added and post-treated PEDOT:PSS films.(e) top performing cells obtained

The removal of PSS and the enhanced conductivity with post-treatment are expected to have a positive effect on the short-circuit current density as reported in other devices.[16,85,68] Interestingly, careful examination reveals this not to be the case for our HSCs. The average J_{SC} are 8.58, 27.73, and 27.15 mA/cm^2 for HSCs with pristine, co-solvent-added and post-treated films, respectively. To further

investigate this unexpected result, external quantum efficiency (EQE) measurements were performed on the HSCs and used to determine J_{SC}. As EQE corresponds to the number of electrons collected per incident photon entering the device,[18,28,111,112] EQE measurement can reveal the optical origins of the electronic process occurring in the cell, allowing the determination of a more accurate and reproducible value for $J_{sc.}$[28] The EQE curves for HSCs with the pristine, co-solvent-added, and post-treated films (85 nm thick) are shown in Figure 3.13 a). The EQE curves for HSCs with the pristine and co-solvent-added films are similar, while those with the post-treated film are discernibly lower. The corresponding J_{SC} calculated from EQE for HSCs with the pristine, co-solvent-added and post-treated films are 28.2, 28.4, and 25.5 mA/cm^2, respectively.

The lower EQE for the HSC with the post-treated film is the result of increased absorbance in the visible and near IR region as shown for the 85 nm thick films in Figure 3.13b). The PSS features at 293 and 225 nm incrementally decrease in intensities from pristine, to co-solvent-added and to post-treated films. However, the overall visible absorbance not associated with PSS increases in intensity solely for the post-treated film (Figure 3.13b) inset), which is indicative of an increased concentration of PEDOT.[89] There is also significantly higher absorbance in the IR region attributed to free charge carrier absorption related to redistribution of charge as a result of secondary doping.[16,82,88,65] The band near 850 nm corresponds to the high-energy bipolaron transition.[16,88]

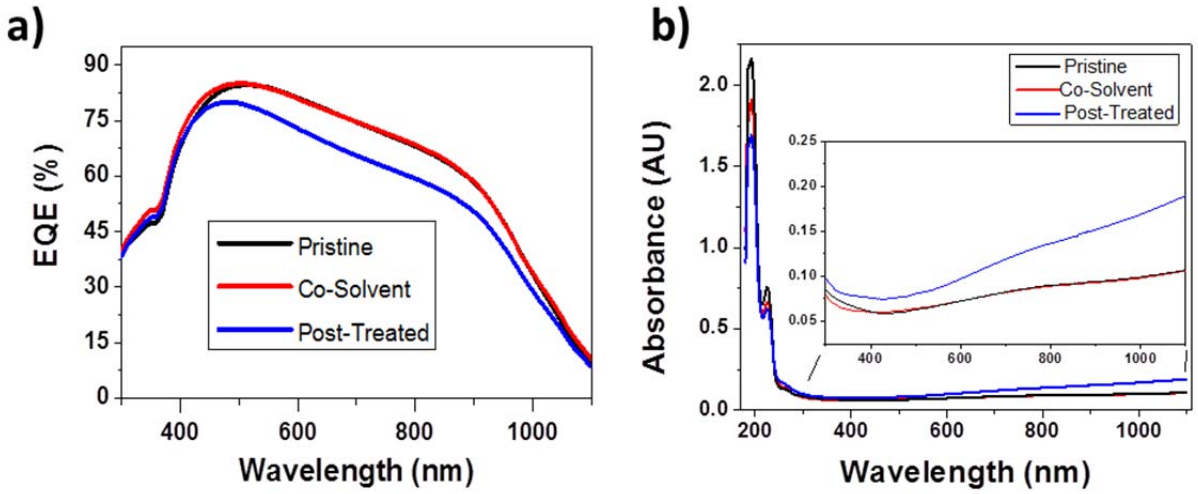

Figure 3.13: a) EQE spectra of HSCs with 85 nm thick pristine, co-solvent-added, and post-treated PEDOT:PSS films, and b) absorbance spectra of the respective PEDOT:PSS films deposited on quartz substrates.

The changes in the conductivity (Figure 3.4a), Raman spectra (Figure 3.4b), and AFM images (Figure 3.6*Figure*) reported here are found to incrementally change when going from pristine to co-solvent-added to post-treated films. In contrast, UV-Vis and EQE results for the post-treated films are discernibly different from both pristine and co-solvent-added films. Compared to the pristine and co-solvent-added films, the post-treated films have been subjected to an additional cycle of swelling and rinse with the MeOH-EG mixture followed by curing treatment at 110 °C. As confirmed by UV-Vis (Figure 3.3a) and FTIR (Figure 3.5b) results, the segregation and removal of PSS produce a higher composition ratio of PEDOT to PSS chains in the post-treated films compared to the pristine and co-solvent-added films. This higher density of PEDOT chains leads to the higher absorbance in the visible range by the film.

The higher PCE found for the HSCs with the post-treated films is due to the higher V_{OC} and FF. The dismal performance of the pristine films follows from the poor J_{SC} and FF and is the result of light-induced structural change of the benzoidal PEDOT structure.[111] Kinks and imperfections that are more prevalent in the pristine films cause changes in the conjugation and the amount of free radicals, and they impede hole transport. This is consistent with the higher J_{SC} value found in the EQE measurements because of the significantly lower light intensity used (1 mW/cm^2) when compared to those employed in standard IV measurements (100 mW/cm^2).

Overall, the HSCs with the post-treated films show a higher average PCE, with the maximum recorded being as high as 11.5%. While the so-called champion-data cells, i.e. those with the best performance, can be achieved, the HSCs with the post-treated films reported here represent “production-ready” cells with easily achievable performance.

3.4. Conclusion

A novel method of secondary doping was developed for improving PEDOT:PSS in HSCs by using a post-treatment method that employs a 1:1 MeOH:EG binary mixture to remove PSS from the film and hence to increase the conductivity. The changes induced in the films using these oxygenates were studied and the results suggest that the low viscosity and polarizability caused a charge screening effect between PEDOT and PSS, freeing and removing the soluble PSS from the film. These solvation driven changes increased the quinoidal nature of PEDOT, the anisotropy, and conductivity parallel to surface. Three large sets of cells with the PEDOT:PSS films are found to exhibit vastly different conductivities: pristine (0.8 S/cm), co-solvent-added (637 S/cm) and post-treated films (1334 S/cm). With over a 10%

gain in the conductivity obtained for post-treatment with the present binary mixture when compared to single-solvent post-treatment, post-treatment with a binary mixture offers an improved method for enhancing the conductivity. In addition to the increase in the sheet conductivity, the post-treatment also results in greater V_{OC} through stronger interface interaction and charge transfer at the junction, offsetting the observed fdecrease in J_{SC} and ultimately increasing the PCE. This work shows a delicate balance when employing PEDOT:PSS for optoelectronic devices and other applications and that gains in conductivity should not come at the expense of other properties such as absorbance.

4. Hybrid Solar Cell Optical Properties

4.1. Introduction

Optoelectronic devices such as LEDs and solar cells that are based on organic materials offer opportunities to reduce the cost, increase efficiencies, and expedite production compared to conventional devices based on inorganic materials. One major challenge with these devices is that highly conductive electrodes need to be transparent to allow visible light in and out. Poly(3,4-ethylene-dioxythiophene) and poly(styrenesulfonate) (PEDOT:PSS) films can function as a transparent conducting electrode, however its thin-film, and optical, and electrical properties will greatly influence device performance and are thus examined closely in this Chapter.

As discussed in Chapter 3, the post-treatment method can be used to remove material, providing a novel way of achieving a very small film thickness. The film thickness could directly affect the short-circuit current density (J_{sc}) by modifying three main properties: (1) The resistivity and path-length (that the photogenerated holes have to travel to reach the electrodes) will decrease with smaller film thickness;[113] (2) the optical properties, particularly anti-reflective properties of the film where reflectance is minimized through constructive and destructive interference arising from the wave nature of light; and (3) the extent of photoexcitation of molecules in the film medium or lattice (phonon) vibrations. This absorption by the material with a thickness d follows the Beer-Lambert law:

$$I(d) = I(0)e^{-\alpha d} \tag{4.1}$$

where α is the absorption coefficient, and d is the thickness which is related to the imaginary part κ of the refractive index by

$$\alpha = 4\pi\kappa/\lambda \tag{4.2}$$

Reducing the film thickness would lead to lower parasitic absorption by the film and increase the probability of absorption at the interface or in the silicon base. It is therefore vitally important to optimize the film thickness of the PEDOT:PSS film to achieve a high-performance solar cell.

Here, we focus on the important role of both conductivity and film thickness of PEDOT:PSS specifically on the performance of HSCs. The optical properties of the films are examined

spectroscopically and used to simulate the optical behavior of the solar cells. The complex indices of refraction of the films are determined from absorption and reflectance measurements and used to model the reflectance with respect to thickness, which is then applied to the external quantum efficiency (EQE) measurements used to determine the optical efficiency of HSCs. In these EQE measurements, the electrical current is accurately measured as a function of wavelength at a well-defined incident light intensity, from which J_{sc} can be calculated. Using internal quantum efficiency calculations for the silicon base, the carrier generation and collection efficiency is studied as a function of thickness to identify how resistivity of the film is related to the performance. Finally, the loss mechanisms for an optimized cell are identified. This method of using perpendicular beam absorption, reflectance and transmittance to study and obtain the optical parameters of these HSCs has advantages over elipsometry since it will not be affected by the anisotropy of the film, or require a predefined model to account for multi-stake layer interference.

Three sets of films with different conductivities were studied: (a) films obtained from as-received PEDOT:PSS solution with 0.25 vol% of fluorine surfactant to aid adhesion to silicon (referred here as pristine); (b) films obtained from co-solvent enhanced PEDOT:PSS solution with 7% EG (co-solvent-added); and (c) co-solvent-added films after an optimized post-treatment consisting of 1:1 MeOH/EG to increase the conductivity and to facilitate the removal of PSS (post-treated). These three different sets of films are studied over a range of thickness to determine the role that PEDOT:PSS film thickness plays on short-circuit current density, open-circuit voltage and, ultimately, device performance.

4.1.1. Reflectance

The interaction of light with matter is best described by the propagation of an electromagnetic wave.[†] For any interaction, the photon energy $E = \hbar\omega$ (where $\hbar$ is the square of Planck constant over 2π, ω is the frequency). Given the complex dielectric function $\varepsilon(\omega) = \varepsilon_1 + i\varepsilon_2$ is physically relevant, the propagation of light through a media is best described using the complex refractive index, which is related to the dielectric function through the Maxwell's relation,

---

[†] Since this work uses light that is incident normal to the surface it does not contain a description of electromagnetism. If ellipsometry measurements were used and the polarization state was considered it would be more relevant. A good explanation can be found in Introduction to Electrodynamics, by David J. Griffiths.[162]

$$n + i\kappa = \sqrt{\varepsilon_1 + i\varepsilon_2} \tag{4.3}$$

where n and κ are the real and imaginary components of the complex refractive index.[114]

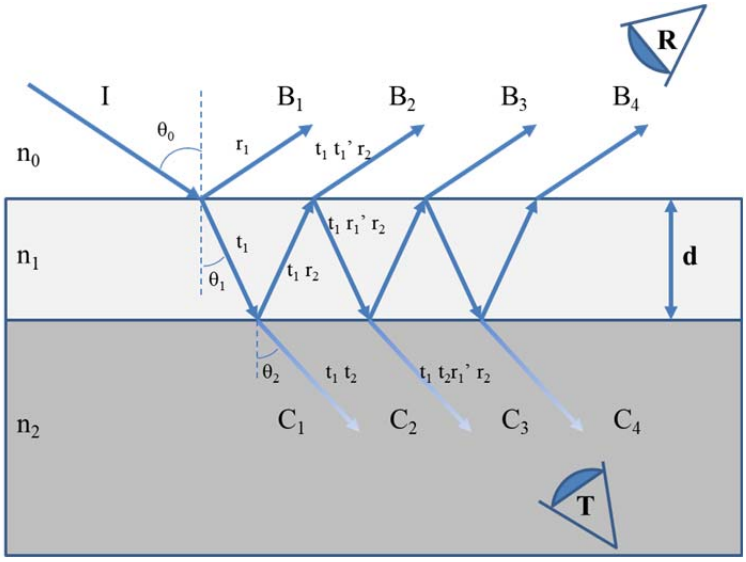

Figure 4.1: Ray diagram of an incident light beam I interacting with a thin film of index n_1 and of thickness d on an absorbing substrate of index n_2. The r's and t's are the Fresnel coefficients, the primes (`) represent the second reflection or transmission off a surface, the B's and C's are the respective higher-order reflections and transmissions, and R and T are the measured total reflection and transmission, respectively,

Electromagnetic radiation incident upon an interface of different refractive indices will undergo reflection off the surface at an angle equal to the incident beam. A proportion will also be refracted into the medium according to Snell's law: $n_1(\lambda)\sin(\theta_1) = n_0(\lambda)\sin(\theta_0)$ (Figure 4.1). The reflectance and the refracted portion of the light are determined by several optical parameters: refractive indices of surrounding media, angle of incidence, and polarization. The amplitude coefficients of the reflected, r, and refracted, t, portions of the electric filed vector for an incident beam at an angle θ_0 from the surface normal comprising of refractive indices n_0 and n_1, are given by the Fresnel equations:[115114]

$$r_p = \frac{n_0 \cos\theta_0 - n_1 \cos\theta_1}{n_0 \cos\theta_0 + n_1 \cos\theta_1} \tag{4.4}$$

$$r_s = \frac{n_1 \cos\theta_0 - n_0 \cos\theta_1}{n_1 \cos\theta_0 + n_0 \cos\theta_1} \tag{4.1}$$

$$t_p = \frac{2n_1 \cos\theta_0}{n_0 \cos\theta_0 + n_1 \cos\theta_1} \tag{4.2}$$

$$t_s = \frac{2n_1 \cos\theta_0}{n_1 \cos\theta_0 + n_0 \cos\theta_1} \tag{4.3}$$

where θ_0, and θ_1 are the angle of incidence and reflected angle, and the s and p subscripts label the perpendicular and parallel plane-polarized components of the electric field vector. Reflectometry measures the spectral reflectance or the ratio of reflected energy to incident energy reflected at normal incidence of the film over a range of wavelengths. Recalling that the intensity I is $I = |E|^2 = E \times E^*$ where E is the electric field vector of the electromagnetic wave and * denotes its complex conjugate, then the intensities of the reflection and refraction off an interface are given by $R = rr^*,$ and $T = \frac{n_o}{n_1} tt^*$ since for T the two beams are in different media. Energy is conserved across the boundary and for an incident beam normal to the surface R+T=1. The reflectivity (R) normal to a single absorbing interface can be written in terms of the complex refractive index:

$$R = \frac{(n_1 - n_0)^2 + \kappa_o^2}{(n_1 + n_0)^2 + \kappa_o^2} \tag{4.4}$$

for non-absorbing substrate $\kappa = 0$.[114,116]

For beams penetrating into thin films, Snell's law dictates that reflection and refraction will occur at each interface with a decreasing proportion propagating within the film. The proportion of light reflected from a single isotropic film of refractive index n_1 on a substrate of n_2 is obtained through a linear superposition of all reflected beams, each normalized to the intensity of the preceding incident beam.[114] Considering the first interference of beams reflected once off each surface (B_1 and B_2 in Figure 4.1), the reflectance with respect to thickness, *d*, and wavelength, λ, is: [114,117]

$$R = R_{01}(\lambda) + R_{12}(\lambda)\left(1 - R_{01}^2(\lambda)\right) + 2\sqrt{R_{01}(\lambda)R_{12}(\lambda)\left(1 - R_{01}^2(\lambda)\right)}\cos\left(\frac{4\pi n_1(\lambda)d}{\lambda} + \phi(\lambda)\right) \quad (4.5)$$

where R_{01} and R_{12} are the reflectances off the exposed thin film, and off the film–substrate interface, respectively, and ϕ is the phase shift (which is zero for nonadsorbing substrates). The normal reflectance with respect to thickness is oscillatory at each wavelength. When the film has an index of refraction between those of air and the substrate [i.e., $n_0 \gtrless n_1 \gtrless n_2$, which is the case for a polymer (<1.77)[118] on silicon (3.98)[119]], the thickness is related to the positions of maximum and minimum reflectance as follows:[116]

$$R_{max} = \left(\frac{n_2 - n_0}{n_2 + n_0}\right)^2 \text{ at } \lambda_{max} = \frac{2n_1 d}{j} \quad (4.6a)$$

$$R_{min} = \left(\frac{n_1^2 - n_0 n_2}{n_1^2 + n_0 n_2}\right)^2 \text{ at } \lambda_{min} = \frac{4n_1 d}{2j+1} \quad (4.8b)$$

where j is an integer. Each normalized higher-order interference (m) will decrease in magnitude by $\left(\sqrt{R_{10}R_{12}}\right)^{1-m}$.[‡] [120] Absorption in films causes the magnitude of the reflected signal also to decrease in accordance to Equation 4.1. Furthermore, any surface roughness causing scattering could also lower the total reflectance. Taking into account absorption and the multiple higher-order beam interference ($B_1 + B_m$ with m = 2, 3, 4…) for normal incidence, the reflectance for the film becomes:[120]

$$R = \frac{\left(R_{01}(\lambda) + R_{12}(\lambda)\exp\left(-\left(\frac{8\pi}{\lambda}\right)\kappa d\right) + 2\sqrt{R_{01}(\lambda)R_{12}(\lambda)}\exp\left(-\left(\frac{4\pi}{\lambda}\right)\kappa d\right)\cos\left(\frac{4\pi n_1(\lambda)d}{\lambda} + \phi(\lambda)\right)\right)}{\left(1 + R_{01}(\lambda)R_{12}(\lambda)\exp\left(-\left(\frac{8\pi}{\lambda}\right)\kappa d\right) + 2\sqrt{R_{01}(\lambda)R_{12}(\lambda)}\exp\left(-\left(\frac{4\pi}{\lambda}\right)\kappa d\right)\cos\left(\frac{4\pi n_1(\lambda)d}{\lambda} + \phi(\lambda)\right)\right)} \quad (4.7)$$

[‡] Higher-order reflectance interferences (m>3) can be assumed to be insignificant for a film like PEDOT:PSS on silicon because of the already high refraction at the PEDOT:PSS/air interface.

The proportion of light transmitted through a film into the substrate follows the same oscillating pattern but opposite.[120]

$$T = \frac{T_{01}(\lambda)T_{12}(\lambda)\exp\left(-\left(\frac{8\pi}{\lambda}\right)\kappa d\right)}{1+R_{01}(\lambda)R_{12}(\lambda)\exp\left(-\left(\frac{8\pi}{\lambda}\right)\kappa d\right)+2\sqrt{R_{01}(\lambda)R_{12}(\lambda)}\exp\left(-\left(\frac{4\pi}{\lambda}\right)\kappa d\right)\cos\left(\frac{4\pi n_1(\lambda)d}{\lambda}+\phi(\lambda)\right)} \quad (4.8)$$

where T is the proportion of transmitted light intensity at each surface $T = (1 - R)$ and the subscripts 01 and 12 denote the thin film and substrate interfaces, respectively. For these calculations, it is assumed that all the light is absorbed by the silicon wafer. It should be clear that the oscillatory behavior of the reflectance and transmittance can be exploited to determine not only the thickness but also the optical constants of the thin films.

4.2. Experimental Details

The HSCs were prepared on 10×10 mm^2, n-type phosphorus-doped Si(100) substrates with resistivity of 1-2 Ω cm and thickness of 200 μm (Virginia Semiconductor Inc.). The substrates were cleaned by sonication in acetone and in isopropyl alcohol, and then washed with filtered high-resistivity (18.2 MΩ) water. The native silicon oxide layer on the Si substrate was removed with hydrofluoric acid (2 vol%, Sigma Aldrich) and then the Si substrate was exposed to air for 2 hours to obtain a stable oxide layer with a reproducible thickness. Aluminum was sputter-coated on the back side of the substrate to form the bottom electrode by using a magnetron sputtering system (EMS575X). Pristine films were prepared from a PEDOT:PSS (Clevios^{TM} PH1000) solution added with a fluorosurfactant (0.25 wt%, Sigma Aldrich) to increase adhesion to the Si substrate. Co-solvent-added films were prepared from the pristine solution by adding ethylene glycol (7 wt%, VWR, ≥99.0%) to enhance the conductivity.[93,95] To control the thickness, a PEDOT:PSS aliquot was spin-coated onto the Si substrate (between 1000 – 12000 RPM to control the thickness), allowed to relax for 5 minutes and then placed on a hot plate at 110 °C for 10 minutes. Post-treatment was performed by adding 80 μL of a binary mixture of methanol (Sigma Aldrich, ≥99.9%) and ethylene glycol with known volume fractions onto the co-solvent-added film. The mixture was drop-casted on and allowed to penetrate the film for 2 minutes before it was spin-coated at 6000 RPM for 2 minutes, allowed to relax for 5 minutes and then to cure on a hot plate at 110 °C for 10 minutes. Finally, the top silver electrode was sputter-coated onto the film using a comb-pattern shadow mask.

Absorbance/transmittance measurements were performed by using a Perkin Elmer Lambda 1050 UV/Vis/NIR spectrophotometer on films supported on 10×10 mm^2 quartz substrates (1 mm thick, SPI Supplies). A Filmmetric F40-UV thin film analyzer was used to collect reflectance spectra and to determine the film thicknesses of the films supported on silicon substrates. The film thickness was verified by using a KLA Tencor P6 profilometer. EQE measurements were performed by using a PV Measurements QEX10 system. The performance of the solar cells were tested with a 4×4 mm^2 illumination area under 1 Sun condition (100 mW/cm^2) using a PV Measurements IV5 solar simulator (equipped with an AM 1.5G filter).

4.3. Results and Discussion

The optical properties of solar cells need to be carefully monitored and controlled to optimize performance. Here, an in-depth look at the different optical properties influencing hybrid solar cells is examined and optimized with thickness and conductivity of the film. The removal of the PSS and the enhanced conductivity with post-treatment are expected to have a positive effect on the short-circuit current density, post-treatment should therefore increase the efficiency, as shown in other devices.[16,85,68] In Chapter 3, it was shown that this was not the case for HSCs and in fact the co-solvent method had produced devices with statistically higher J_{sc} while post-treatment had led to better overall device performance because of higher open circuit voltage likely resulting from improvements to the heterojunction. To further investigate this discrepancy, absorbance, reflectance and external quantum efficiency measurements were analyzed in order to maximize the number of photon-generated electrons. As EQE corresponds to the number of electrons collected per incident photon entering the device, EQE measurement provides the amount of charges collected after optical and recombination losses, allowing the determination of a more accurate and reproducible value for $J_{sc.}$ [18,28,111, 112]

4.3.1. Absorbance/Transmittance

In Chapter 3, the difference between PEDOT:PSS post-treated films and those not treated was found to be related with the optical properties of the cells. To further investigate this, the absorption coefficient (α), extinction coefficient (κ), and refractive index (n) were calculated from UV-Vis measurements of films supported on quartz substrates.[†] The absorption spectra of films with 7 different thicknesses were

[†] Quartz is used because it has no absorption, $\kappa = 0$, over the spectral region of interest.

collected. The UV-Vis spectrophotometer was operated in a double-beam configuration with one film in the path of the reference beam and the thicker film in the sample beam path. In this setup, the effects of surface-reflection at the film-substrate interface can be removed and the absorption will be due only to the difference in the film thickness.

The extinction coefficient and refractive index of PEDOT:PSS were determined using the transmittance spectra and applying a Lavenberg-Marquardt least squares algorithm (Appendix 2). The function for total transmittance, $T = T_{front} \times T_{rear} \times A_{film}$, is derived from the Fresnel equations (Eq 4.4-4.7):[116]

$$T = \frac{16n_2(n_1^2 + \kappa_1^2)\exp\left(-\frac{4\pi\kappa_1 d}{\lambda}\right)}{[(n_1+1)^2 + \kappa_1^2][(n_2+n_1)^2 + \kappa_1^2]} \tag{4.9}$$

Figure 4.2 shows the extinction coefficient and refractive index as functions of wavelength for films with the three different treatments. The post-treated film generally displays a higher extinction coefficient and a lower refractive index than the other films over the whole spectral range. The inflection points of the extinction coefficient correspond to the maximum/minimums of the refractive index as demanded by Kramers-Kronig analysis.[115,120] A higher extinction coefficient is expected to give rise to an increased conductivity. The discernibly higher extinction coefficient in the IR region is attributed to the free charge carrier absorption related to charge redistribution as a result of secondary doping and to the quinoidal conformation of PEDOT.[16,82,65] The increase in the visible r

ange can be associated with the greater concentration of PEDOT relative to the PSS chains, which have a greater absorbance in that region. Concomitantly, the refractive index curve for the post-treated film generally lies lower than the other films, which is consistent with the reduction in the concentration of the higher-index PSS. The latter has been reported for PEDOT:PSS films with PEDOT:PSS concentration ratios of 1:6 and 1:20. [39,82] Interestingly, no significant change is seen in the extinction coefficient between the co-solvent-added and pristine PEDOT:PSS films, despite the increase in the conductivity found the co-solvent-added film. IR absorbance as the result of mid-gap states could cause the observed red shift in the absorption maximum.[82]

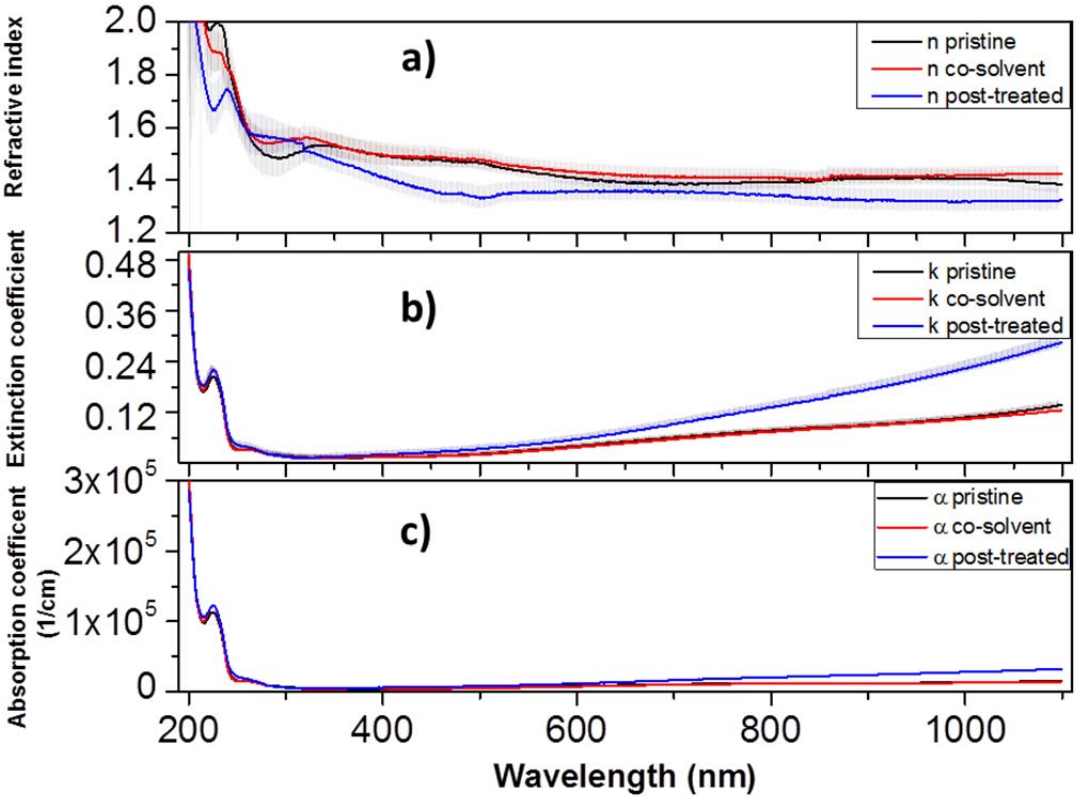

Figure 4.2: (a) the refractive index n, (b) extinction coefficient k, and (c) absorption coefficient α for pristine, co-solvent-added and post-treated PEDOT:PSS films as functions of wavelength The error bars indicate standard deviations.

4.3.2. Reflectance

The reflectance spectra of PEDOT:PSS on planar Si, with light incident normal to the surface, for different PEDOT:PSS film thicknesses are given for both experimental curves (red) and simulated curves (black) in Figure 4.3. The shifts in maxima and minima with thickness and wavelength caused by constructive/destructive interferences as expected from Equation 4.9, are evident. The reflectance of hybrid solar cells was optimized under standard surface conditions, air mass 1.5G, for peak power in the visible/NIR (300 – 1100 nm) range. The thickness at which the greatest anti reflective behavior occurs for this range is 102 nm. This reflectance profile is important when optimizing cells for different conditions,

like for indoor use where the incoming irradiation spectrum is different. Moreover by tailoring the thickness to minimize reflectance at desired wavelengths, these cells can easily be made into photodetectors.

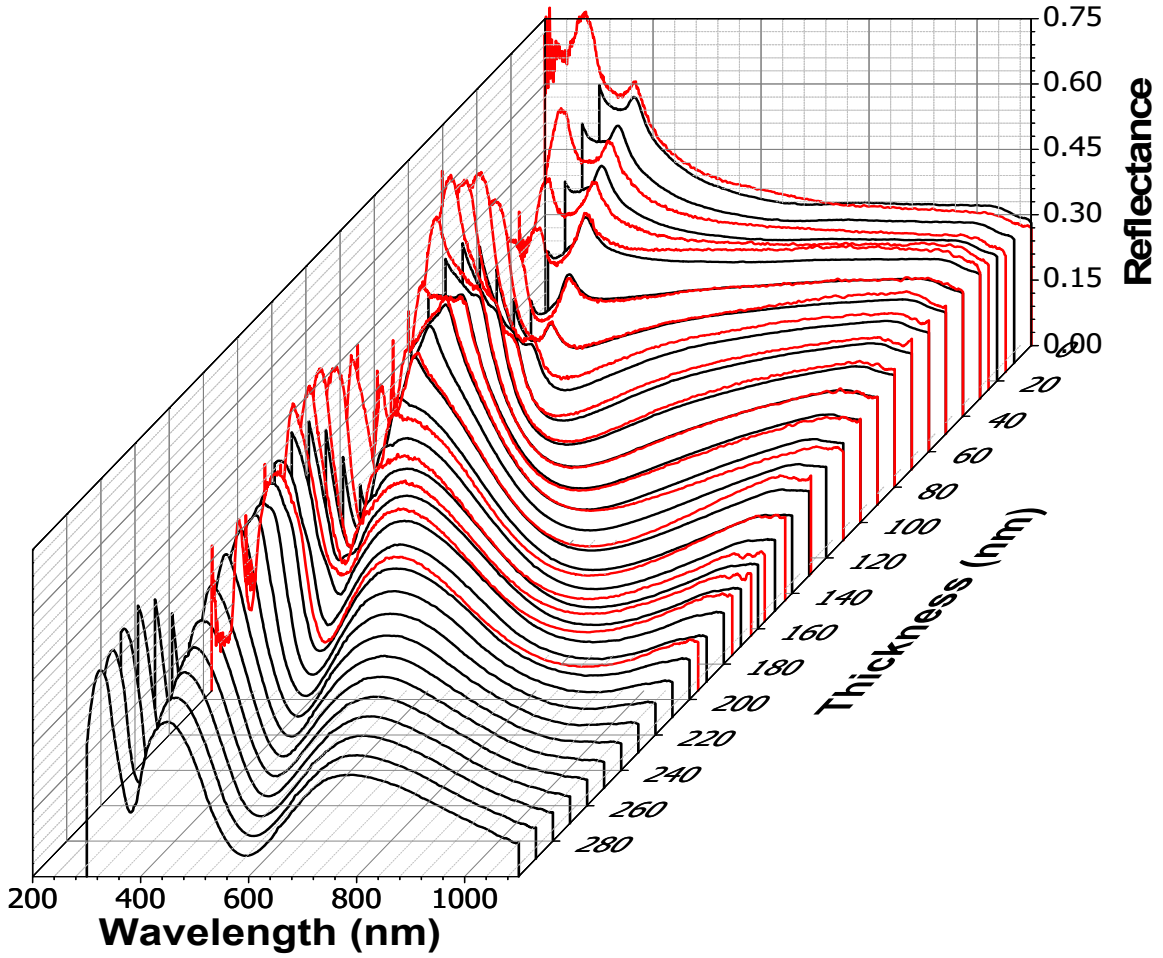

Figure 4.3: Experimental (red) and simulated (black) reflectance spectra for the post-treated PEDOT:PSS film as a function of film thickness and wavelength. The oscillatory behaviour of the spectral intensity with respect to wavelength and thickness is evident.

Film thickness is usually determined from the numbers of maxima and minima in the oscillating pattern with respect to wavelength.[120] However, the small thicknesses of the spin-coated films make it difficult to fit and obtain other optical properties because full oscillations cannot be observed until a film thickness of ~150 nm. Further complicating the analysis is the large extinction coefficient of the silicon substrate. Silicon becomes more transparent at longer wavelengths with a sharp onset in transparency for wavelengths of lower energy than the band-gap (1.12 eV; 1107 nm). Indeed the wavelength for which the

signal-to-noise ratio becomes larger than the detection of the reflectance amplitude is ~875 nm for a 200 um silicon wafer.[119] This causes interference from refraction out of silicon and a multiple stack layer would be needed in the model, which greatly complicates the calculations. Therefore an assumption must be made that internal refraction within silicon does not affect the reflectance of spectra and that all light is absorbed by the silicon. This is valid since the Lambertian textured rear side of the silicon wafer will scatter the light reaching it and very little will be reflected directly back.

The spectra were modeled with respect to the film thickness, using a Lavenberg-Marquardt least squares algorithm (Appendix 2) with the extinction coefficient calculated from the transmittance analysis discussed above. The PEDOT:PSS refractive index, phase shifts and reflectance off the air/PEDOT:PSS interface and off the PEDOT:PSS/silicon interface were obtained by fitting the reflectance spectra of 150 pristine, co-solvent-added and post-treated films. The fitting parameters are shown in Figure 4.4. The reflectance off the PEDOT:PSS/silicon interface contains the characteristic interband transitions expected at 365 nm and the broader shoulder of the 288 nm peak (R_{12}, Figure 4.4a).[‡] The reflectance of the PEDOT:PSS film is small and is under 5%. The index of refraction and the phase shift both show a generally decreasing trend with increasing wavelength. [82,121]

[‡] Transitions associated with the electronic band structure of Si where the vertical transitions, at wavevector $\boldsymbol{k} = 0$, occur.

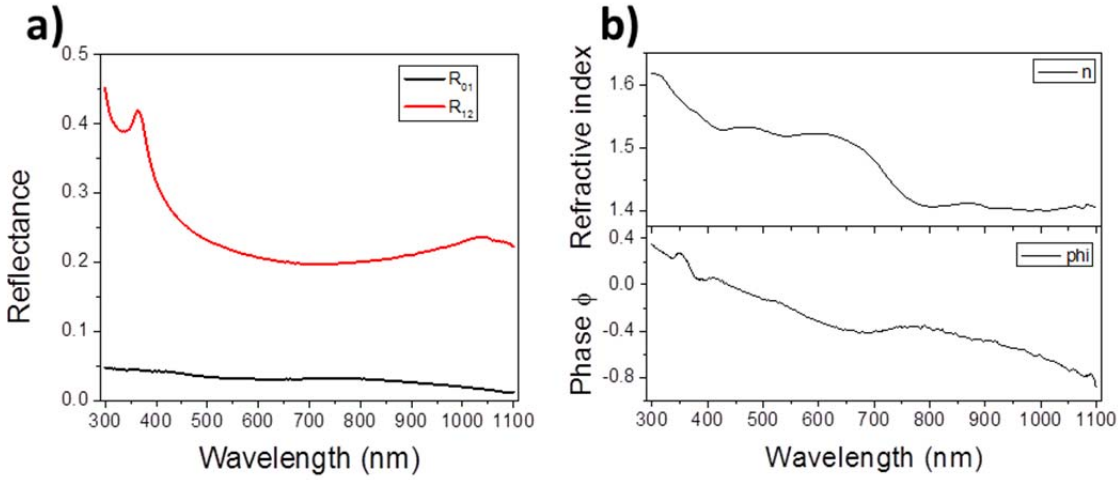

Figure 4.4: (A) Simulated reflectance spectra off the top PEDOT:PSS surface (R_{01}) and the silicon interface (R_{12}). (B) Simulated refractive index (n) and phase shift ($\boldsymbol{\phi}$) as functions of wavelength.

4.3.3. Quantum Efficiency

The external quantum efficiency curves for the pristine, co-solvent-added, and post-treated films of different thicknesses are shown in Figure 4.5. The EQE profiles for both the pristine and co-solvent-added films are similar at equivalent film thicknesses, while the EQE profiles for the post-treaded films appear to lie lower than the others. The differences between the post-treated films and the others become greater at larger wavelengths. For practical solar cell application, the EQE should be maximized in the visible spectrum in order to maximize the efficiency.

As shown in Figure 4.6, the EQE at any given wavelength appears to follow a sinusoidal behavior with respect to film thickness, which is the opposite trend of the reflective behavior of the films. It is evident that post-treatment reduces the overall EQE but it does not change the reflectance significantly.[‡] The change in *n* after post-treatment noted in the transmittance analysis (Section 4.3.1) causes a decrease

[‡] For multiple interference to take place, the condition $d = m\lambda/4$ for m>2 is only satisfied for film thickness above 150 nm for the wavelengths considered. Moreover, the condition $\kappa^2 \ll (n-1)^2$ does not hold for PEDOT:PSS and the optical properties and effects are difficult to be observed with normal incidence.[163,164]

in the maxima of EQE and a red shift in peak positions in accordance with Equation 4.10, although such a significant decrease especially at larger wavelength is unexpected. The lower EQE could result from changes in the complex refractive index and series resistance in the PEDOT:PSS film, which will be discussed further below. For wavelength above 875 nm, the amplitudes of EQE curves all follow a decreasing trend with respect to wavelength and they appear not dependent on changes in the film thickness. In this wavelength region, the 200 μm silicon wafer is too thin to absorb these low energy wavelengths and produce photoelectrons.

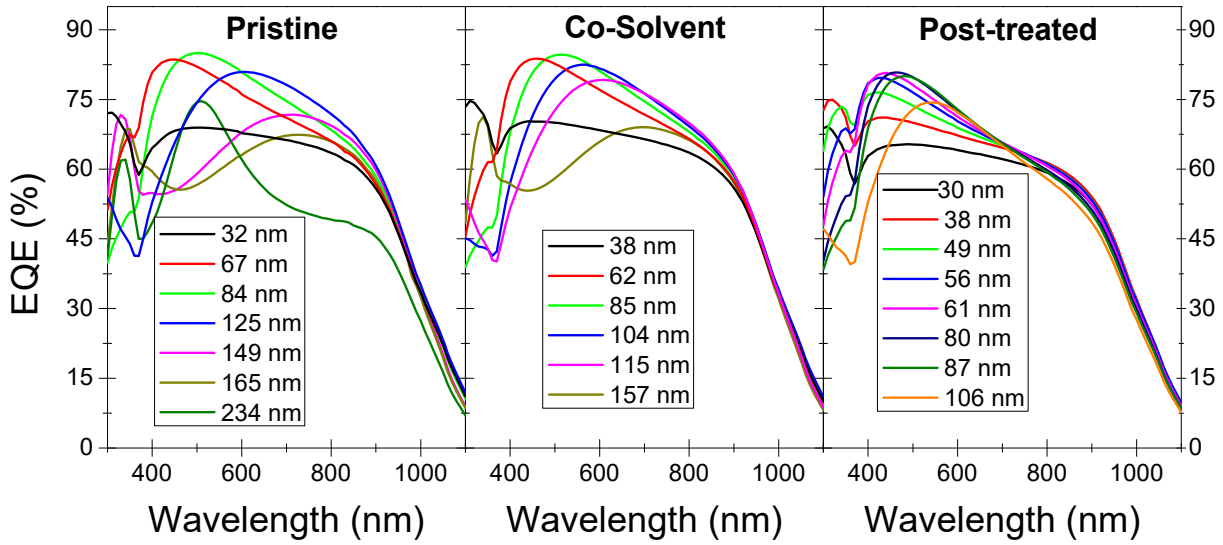

Figure 4.5: EQE spectra of pristine, co-solvent-added, and post-treated PEDOT:PSS films at selected film thicknesses.

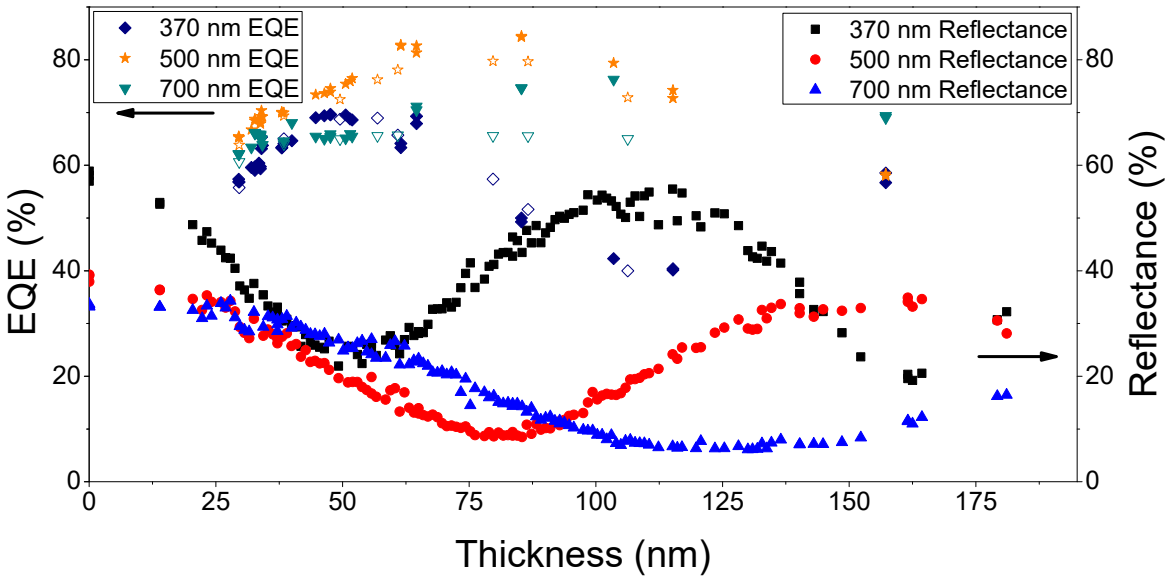

Figure 4.6: Quantum efficiency and reflectance at selected wavelengths, all following the inverse sinusoidal behavior with respect to film thicknesses. The solid symbols correspond to EQE of pristine and co-solvent films whereas the open symbols are EQE of the post-treated films.

Quantum efficiency data can be perceived as the proportion of energy transmitted into the silicon substrate which produces charge carriers. As discussed in Chapter 3, it is a safe assumption that no charge carriers are produced in the PEDOT:PSS emitter layer. The quantum efficiency data with respect to thickness was simulated similarly to the reflectance measurements however using transmittance into a substrate from a single layer, Equation 4.10. Assuming, for a moment, that all the photons absorbed by the silicon produce electron-hole pairs (neglecting the absorbance, especially at the longer wavelength, by free carriers caused by dopants in Si), then the number of photocarriers generated in the 200-µm-thick silicon substrate base is proportional to the absorbance given by Beer-Lambert law: $I(200\mu m) = T_{12}\exp(-\alpha_{Si} \times 200\mu m)$ where the macroscopic absorption coefficient, $\alpha_{Si}(\lambda)$, refers to the attenuated light, and corresponds to the fraction of absorbed light upon passing through the silicon wafer. T_{12} is the proportion of light refracted at the PEDOT:PSS/Si interface, $T_{12} = \left(1 - R_{12}\exp\left(-\frac{4\pi\kappa_{Si}d}{\lambda}\right)\right)$ where κ_{si} is the extinction coefficient for silicon. Therefore, to model the EQE with respect to the film thickness, a multiple layer stack should be used and a third term G(λ) is added. G represents the generation and collection of carriers by the silicon base, which from here on is referred to as Si-Generation. EQE in relation to the PEDOT:PSS film thickness was modeled using:

$$EQE(d) = \frac{(1-R_{01}(\lambda))\left(1-R_{12}(\lambda)\exp\left(-\left(\frac{8\pi}{\lambda}\right)\kappa d\right)\right)G}{1+R_{01}(\lambda)R_{12}(\lambda)\exp\left(-\left(\frac{8\pi}{\lambda}\right)\kappa d\right)+2\sqrt{R_{01}(\lambda)R_{12}(\lambda)}\exp\left(-\left(\frac{4\pi}{\lambda}\right)\kappa d\right)\cos\left(\frac{4\pi n_1(\lambda)d}{\lambda}+\phi(\lambda)\right)} \quad (4.10)$$

The simulated EQE spectra from fitting the pristine and co-solvent-added spectra using R_{01}, R_{12}, and ϕ obtained from the reflectance model, and n_1 and κ calculated from the absorption of the co-solvent-added films are shown in Figure 4.7.

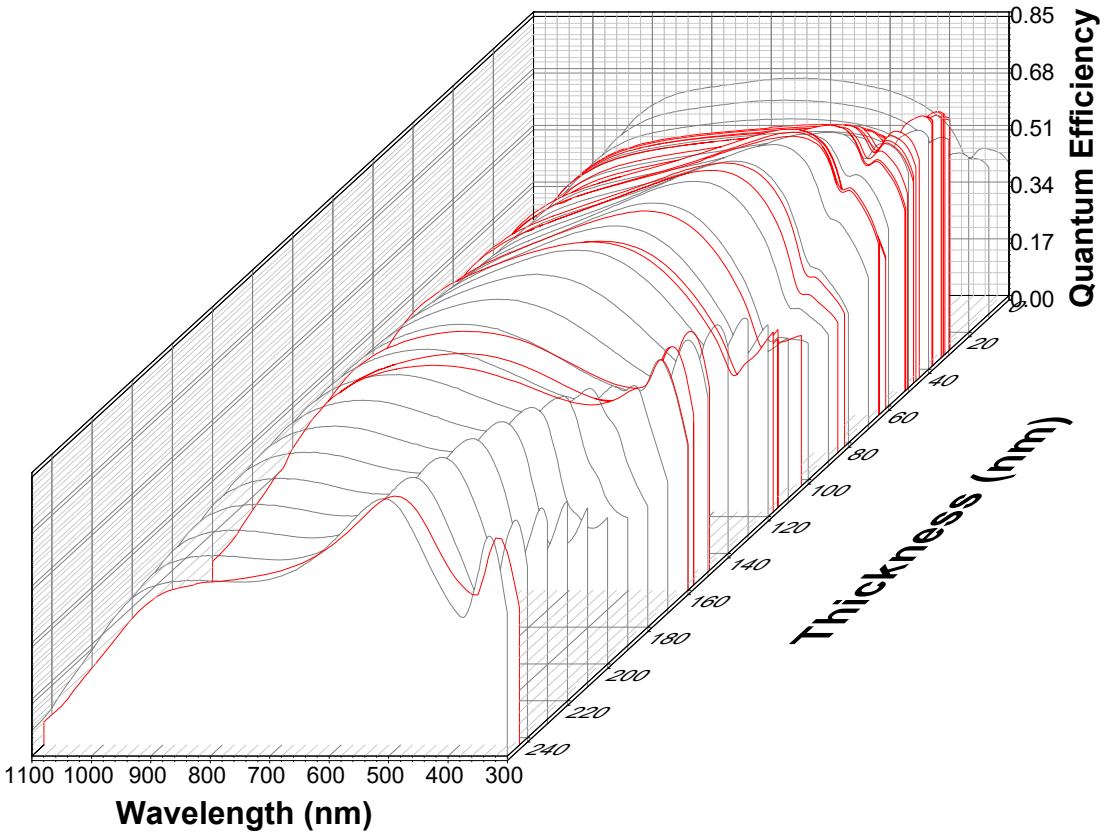

Figure 4.7: Experimental (red) and simulated (gray) EQE spectra at different thicknesses.

Using equation 4.12 and the assumptions that all the light transmitted into the silicon base is captured and no charge carriers are produced in the PEDOT:PSS layer results in a simulated EQE in good agreement with experimental results. Analytical simulations of any solar cell is difficult since both electrons and holes usually contribute to both transport and recombination making decoupling the optical and electronic parts of the EQE difficult.[90] Since hole minority carriers are only produced in the silicon base

and are the relevant carrier in HSCs the optical absorption and electronic properties are easily to discernable and a solution to the continuity equation exists. The goodness of the fit between simulation and experiment depends on the correct accounting of the optical and electrical loss mechanisms in the simulation. The simulation of EQE allows for precise optimization of the film thickness of HSCs and a method to tailor the cells for specific lighting conditions. With this equation the EQE and film thickness can be obtained in a rapid single measurement. It can be easily modified to fit other PEDOT:PSS optoelectrical devices or other transparent conductive films with only knowledge of their indexes of refraction and base substrate.

4.3.4. Short-Circuit Current Density

External quantum efficiency is the number of electrons collected per incident photon entering the device.[18,28,111,112] It reveals the optical origins of the electronic processes occurring in the cell that account for reflectance and recombination losses, allowing the determination of a more accurate and reproducible value for J_{sc}.[28] Using the entire EQE spectrum, J_{sc} can be obtained by using the equation:

$$J_{sc} = q \int EQE \, d\phi = \int_{\lambda min}^{\lambda max} Rs \times Sr \, d\lambda \tag{4.11}$$

Where $d\phi$ is the incident photon flux in units of $cm^{-2}s^{-1}$, Rs is reference spectrum of the sun under the AM 1.5G condition (Figure 2.9), and Sr is the spectral response of the cell. Sr corresponds to the current generated per unit power of the incident light on the device in [A/W] and is given by:.

$$Sr = \frac{q\lambda}{hc} EQE \tag{4.12}$$

The corresponding J_{sc} calculated for HSCs of different thicknesses are given in Figure 4.8, along with that calculated from the modeled EQE extended to film thickness up to 250 nm. Experimentally, J_{sc} reaches its maximum values of 28.3 mA/cm^2 for film thickness of 85 nm for both pristine and co-solvent-added films but 26.2 mA/cm^2 at 63 nm for the post-treated films. Interestingly, the J_{sc} values for the non-treated cells, despite having higher sheet resistance, are discernibly higher (by ~8%) than HSCs with post-treatment, all compared at the optimal film thicknesses. To calculate the J_{sc} of the post-treated films, optical properties n and k from the transmittance study were used. Evidently, the calculated J_{sc} was higher than those found experimentally, indicating that the decrease for film thickness greater than 60 nm could

be due to not just a change in optical properties but also electrical properties. Cells with film thickness below 35 nm stop adhering to the model, likely because the decrease in the built-in-potential, and the increased likelihood of shorting the device with the sputtered silver top grid.

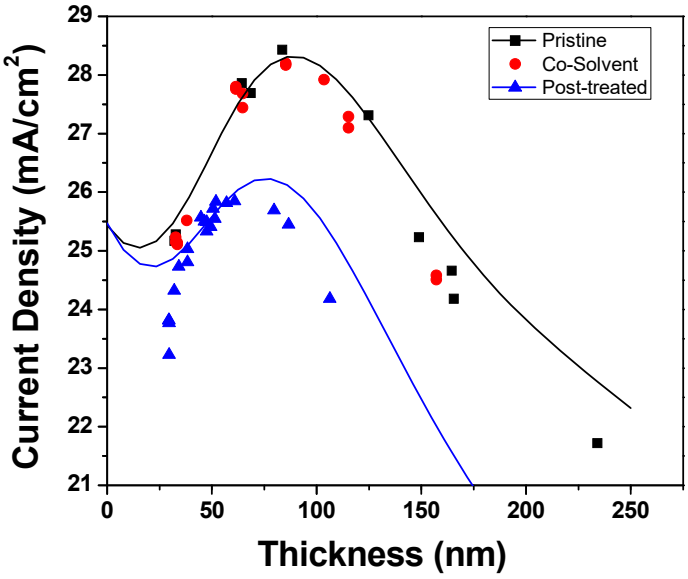

Figure 4.8. Experimental short-circuit current density obtained from EQE data for pristine, co-solvent-added and post-treated PEDOT:PSS films with different film thicknesses, and simulated J_{sc} for pristine and co-solvent-added films (black line) and post-treated films (blue line). The maximum occurs at an optimal film thickness that provides a balance between decreasing reflectance and increasing absorbance and emitter resistance.

An advantage that these cells have over organic heterojunction solar cells is their broad absorption spectrum and long electron-hole diffusion length. For bulk heterojunction solar cell, Mourle et al. observed a similar oscillatory behavior as that shown in Figure 4.7. in the reflectance and EQE with respect to thickness, which was replicated in the measured J_{sc}.[122,123] This oscillatory behavior of J_{sc} is not found in HSC even extending the model to 500-nm-thick films since these HSCs are not as sensitive to the shot diffusion lengths of excitons and localized absorption at the junction. Optimizing the film thickness to maximize the light intensity for desired wavelengths at the heterojunction is therefore not as necessary for HSCs while instead these cells can be optimized to the solar irradiance on earth.

4.3.5. Internal Quantum Efficiency

As photon-generated electrons and holes are produced in the silicon base in HSCs, all the remaining photons not reflected are assumed to pass into the silicon, such that the absorbance is given by $A = 1 - R$. The internal quantum efficiency (IQE) corresponds to the total number of electrons produced per photon passing into the silicon:[28,112]

$$IQE = \frac{EQE}{(1 - R)} \tag{4.13}$$

Substituting Equation 4.9 for reflectance and Equation 4.12 for EQE, IQE is found to be equivalent to Si-generation, *G*, introduced above in Section 4.3.3. *G* can be considered the internal quantum efficiency of the silicon base layer or the effectiveness of this layer at generating photocurrent. It is a function of the generation of carriers (g) in the material and the collection probability (f_c) , $G(\lambda) \propto \int_0^x g(\lambda, x) f_c(x) dx$, where x is the depth inside the silicon wafer.[25,28] The percentage of light captured by a 200 μm silicon substrate is given by the transmittance using the absorption coefficient of intrinsic silicon at 300 K that was taken from Green *et al.*[124,125] Si-generation, the transmission through of a 200-μm-thick silicon substrate, along with the calculated collection probability is shown in Figure 4.9. Comparing *G* to the transmission through silicon shows that the cells have a lower than expected collection probability for short wavelength likely due to surface recombination. Collection probability for wavelengths between 600 nm and 1050 nm decreases, which is caused by the indirect band-gap of silicon and recombination in the bulk and rear of the cell (where carriers are generated more than one diffusion length away from the junction often seen in optical devices).[126] The increase in collection probability for wavelength over 1050 nm is the result of the textured Lambertian rear surface that scatters the light, increasing the probability of absorption. since the calculated transmittance assumes two sided polished surface it underestimates the absorbance in the region.

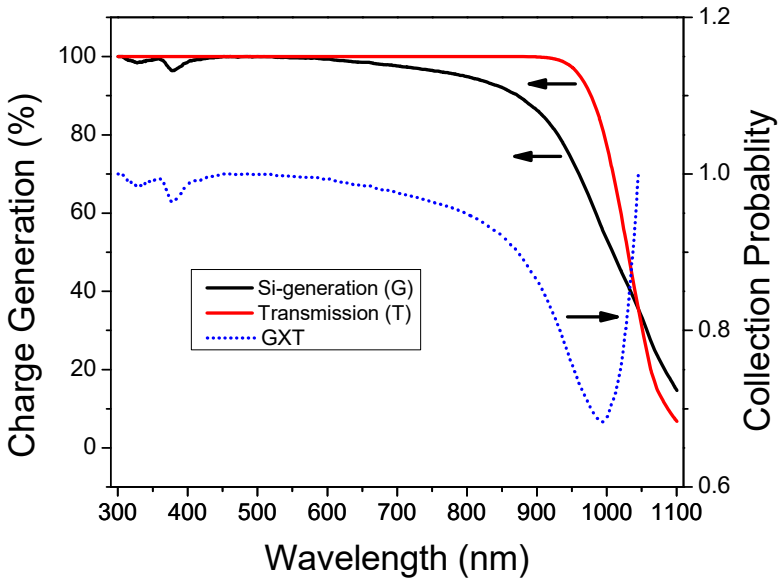

Figure 4.9: Si-Generation (black), transmittance spectra of silicon (red) and collection probability (blue) with respect to wavelength.

The experimental IQE profile for pristine, co-solvent-added and post-treated films with several different thicknesses are shown in Figure 4.10. Evidently, the IQE curves for all cases are found to decrease with increasing film thickness, and since the optical effects have been eliminated the decrease can be associated with electronic mechanisms (recombination and resistivity). The post-treated films with the reported film thicknesses all exhibit a relatively flat IQE in the 300-400 nm (blue) range, in marked contrast to those of pristine and co-solvent-added films. This is likely the result of less interface recombination and overall better surface passivation as discussed in Chapter 5.

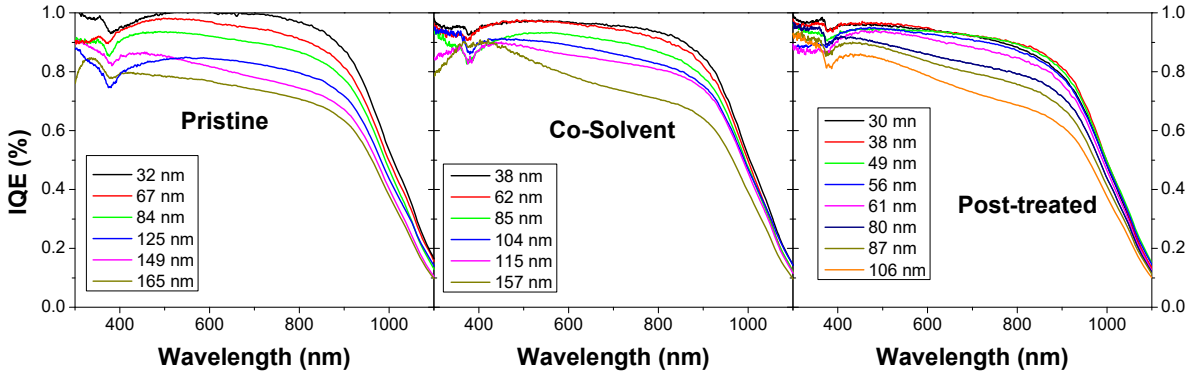

Figure 4.10: Internal quantum efficiency of pristine, co-solvent and post-treated films of different thicknesses.

By integrating under the IQE curves – similar to the treatment of the EQE – we can obtain the Total IQE or the Si-generation over the whole solar spectrum with respect to film thickness. Normalizing it to the expected 100% collection efficiency of the entire spectrum gives the ratio of current generated to incident photon flux (assuming each photon produces a photon-generated electron).

$$Total\ IQE = \int_{\lambda_{min}}^{\lambda_{max}} Rs \times \frac{q\lambda}{hc} IQE d\lambda \tag{4.14}$$

For all films, the Total IQE is found to decrease for film thickness greater than ~35 nm (Figure 4.11), as expected since the resistance through the film will increase with thickness. From this a comparative measure of the resistivity of the films can be surmised. The reflection-eliminated, normalized current density can be fitted using the a modified single diode equivalent circuit model for a solar cell (Figure 2.8). The resistivity can be approximated according the following semi-empirical equation derived from Equation 2.9 under short circuit conditions assuming constant shunt resistance:

$$Total\ IQE(d) \propto \frac{J_l}{1 + \rho d} \tag{4.15}$$

where ρ is the resistivity (Ω) and J_l is the light-generated current density.[‡] As shown in Chapter 3, there is little to no change in the resistivity between the pristine and co-solvent-added films, both of which have very different sheet conductivities; and an increased resistivity in the post-treated samples that exhibited the highest sheet conductivity (Figure 3.4). The calculated resistivity of the post-treated film (1.01×10^3 Ω/cm) was 75% and 64% more than that of the pristine (5.77×10^2 Ω/cm) and co-solvent-added (6.15×10^2 Ω/cm) films, respectively. These anomalous results arise from anisotropy differences between the treatments as identified in Chapter 3. The post-treatment causes PEDOT chains to lay parallel to the surface because of the removal of the PSS scaffold and the secondary spinning process (to which they are subjected) impeding current movement normal to the surface. The light generated current density should theoretically be constant and be related to the Total IQE for the Si-generation curve, however J_l increases from pristine (41.89 mA/cm) to co-solvent-added (42.90 mA/cm) and post-treated films (43.87 mA/cm), this change could be related with a higher open-circuit voltage and lower shunt resistance as noted in Chapter 3.

[‡] The light-generated current density is the maximum current produced from the silicon while taking the limit to a film thickness of zero or zero resistivity, and is related to Si-Generation (G) and the collection probability (*fc*) by $J_l = q\int_0^d G[number\ of\ photons/cm^2]fc(x)dx$. [25,28]

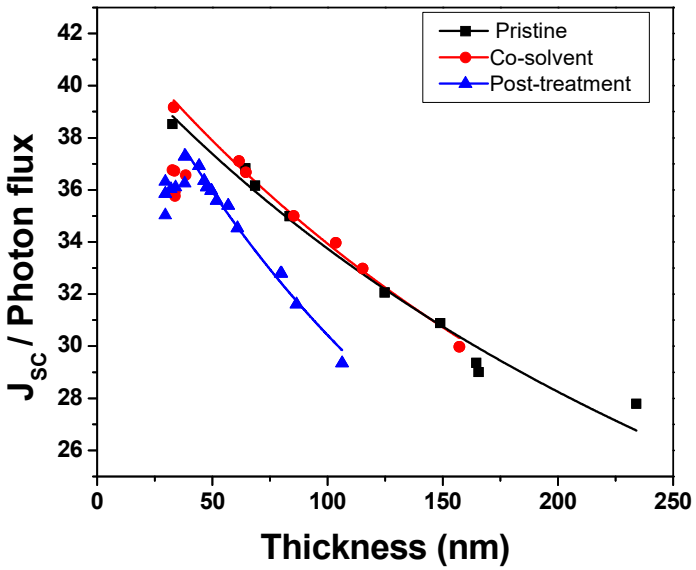

Figure 4.11: Total IQE for pristine, co-solvent-added and post-treated PEDOT:PSS films. The rate of decent of the curves of best fit is related to the optical transparency, and the resistivity of the set of films as well as charge transfer at the interface.

The maximum J_{sc} occurs at a thickness where the decreasing total reflectance of the cell, which follows a sigmoidal shape (Figure 4.8), is not overwhelmed by the linearly increasing total absorbance and resistivity of the film. The position of this maximum depends on the transparency and conductivity of the film, with greater values leading to larger maxima for the thicker films. From analysis of the reflection data alone (Figure 4.3) in the absorption window of these HSCs (300 – 1100 nm), it can be concluded that a thickness of 102 nm results in the greatest anti–reflective behavior. It is thought that if film transparency could be increased and resistivity decreased, a higher J_{SC} maximum could be archived experimentally with a film thickness approaching 102 nm .

Using the calculated absorbance, reflectance, and quantum efficiency from the models above, we can make a full representation of the generation and loss mechanisms in HSCs for the cells with the best J_{sc}, involving 85-nm-thick, co-solvent-added films over the optical window studied. These cells convert a commendable 61.5% (calculated from simulated EQE) of incoming light to photon-generated electrons, which corresponds to a short-circuit current density of 28.3 mA/cm^2. Optical losses result in the largest reduction to the current, 22.2% through reflectance (calculated from simulated reflectance), followed by

6.9% through PEDOT:PSS absorption (calculated from simulated transmittance), both of which cause photons to never reach the silicon base to produce the charge carriers. Of the energy entering the silicon, 2.7% is absorbed by the rear aluminum electrode (calculated from experimental transmittance.[†] Finally, the remaining energy associated with the recombination processes at the front, in the bulk and at the rear of the cell makes up 6.7% of the energy lost.

This maximum short circuit current density is within the range of conventional planar silicon solar cell which tends to be between 28 – 37 mA/cm^2.[14,127,128] The hybrid solar cells tested here are producing similar current densities using very simple processing methods, at low temperatures and only using an organic polymer as the emitter layers making them an ideal replacement to expensive conventional solar cell.

[†] this proportions are slightly higher than the actual, because they were experimentally obtained on a two-sided polished wafer with a 85-nm-thick PEDOT:PSS film and not one with a lambertian rear surface as used in the hybrid solar cells

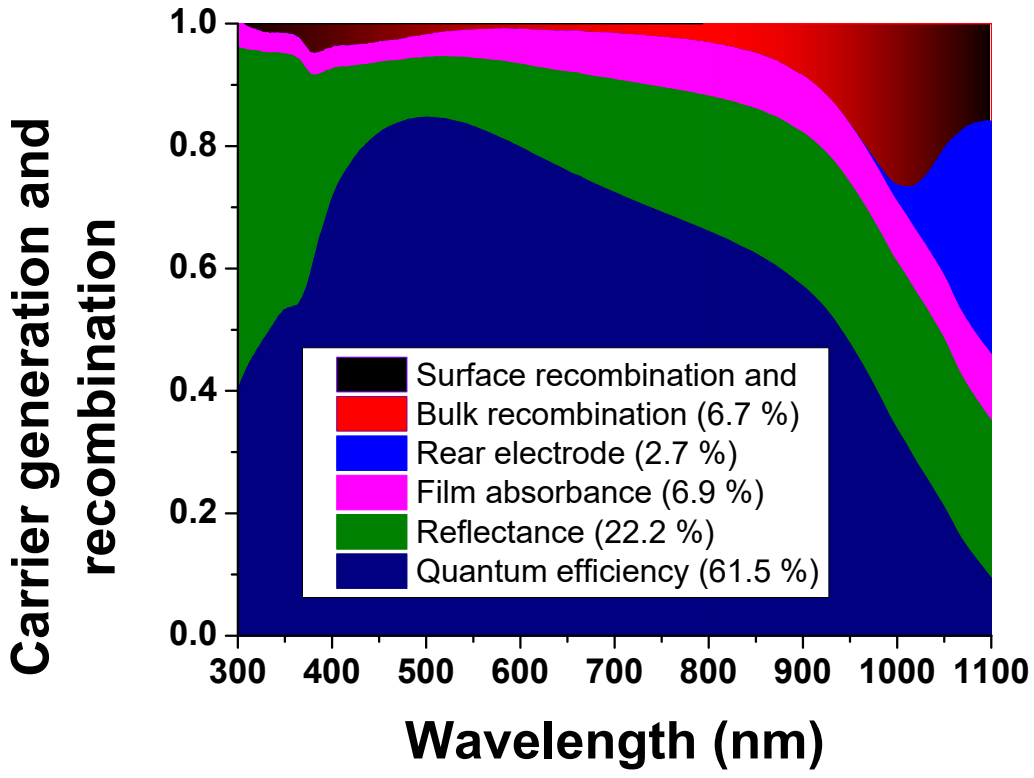

Figure 4.12: Optical generation, and optical and electrical loss mechanisms affecting the current density inside a hybrid solar cell.

4.3.6. Solar cell performance

The J-V solar simulator measurements of the cells used above in the EQE measurements were tested and compared (Figure 4.13). The higher efficiency found for the post-treated films is due to the higher V_{OC}, which results from the improved PEDOT:PSS/n-Si interface as mentioned above. The trends in J_{sc} are not duplicated in the J-V curves, which shows the difficulty in using this measure to produce meaningful conclusions associated with the current. The solar simulated curves suffer from uncertainties that are greatly reduced or non-existent using EQE measurements, including: errors associated with improper measurement of the surface area, increased probability of interface defects such as micropores and impurities that can increase the number of microshunts due to the larger area exposed, and influences such as temperature, humidity, differences in spectral response between the silicon calibration cell and the test cells, and changes in the potential barrier under low-intensity monochromatic illumination and

AM1.5G illumination. [28,129] The poor performance of the pristine films follows from the lower J_{sc} and FF values, and is a result of the light-induced structural change.[111] Kinks and imperfections that are more prevalent in the pristine films cause changes in the conjugation and the amount of free radicals, which impede hole transport. With the injection of light-induced charge carriers and the presence of polaron modes, PEDOT chains are distorted and must rearrange themselves often resulting in a new geometry and a change in the electronic energy levels. This effect is not seen in the EQE measurements because of the low light intensity used (1 mW/cm^2). Secondary doped films are not affected because the linear conformation changes to the longer quinoidal structure, which leads to greater stability, delocalization of charges associated with bipolarons, and better hole transport. Overall, the post-treated cells showed higher efficiencies, with the highest being 11.2% for a cell with an optimized film thickness of 87 nm, and the V_{OC} followed a similar trend. However, as shown in the simulated J_{SC}, it would be expected that this higher efficiency would not be maintained for thicker films since the J_{sc} values for the post-treated cells decrease rapidly with increasing film thickness because of real increases in the film absorbance and resistivity.

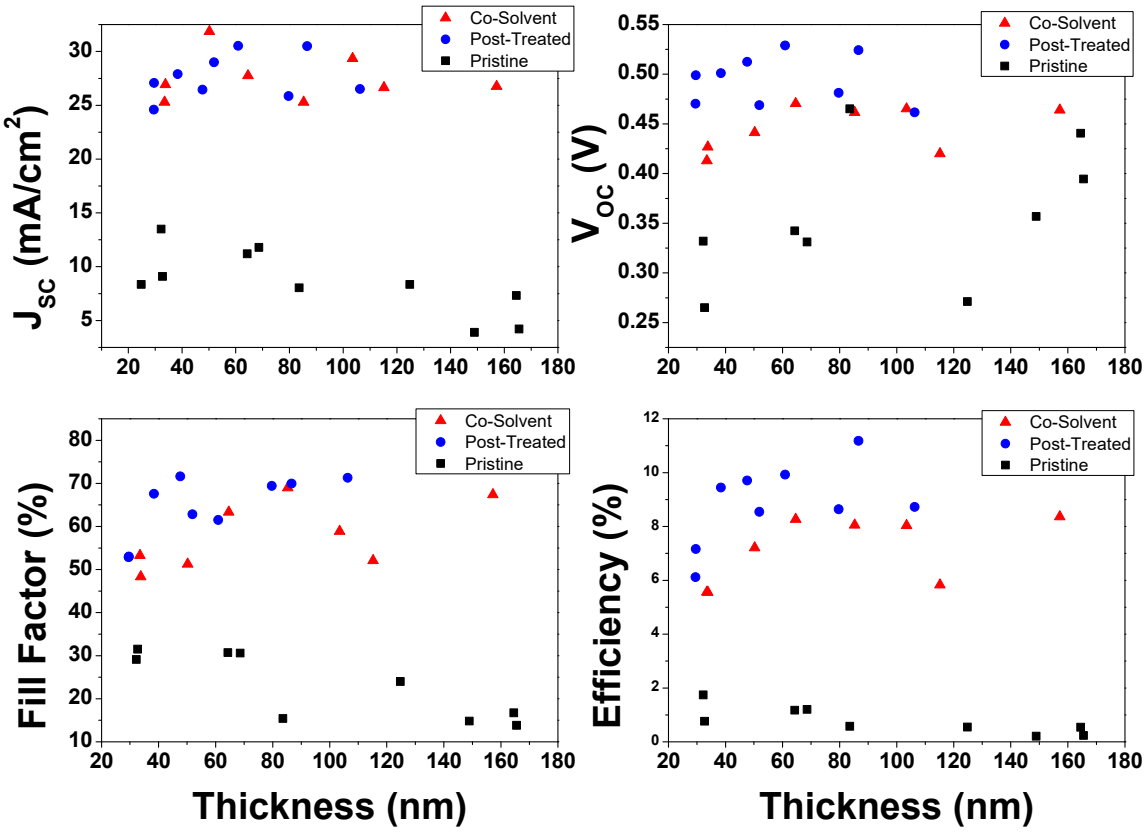

Figure 4.13: I-V characteristics for pristine, co-solvent-added, and post-treated films at different thicknesses: Short-circuit current density (J_{sc}); open-circuit voltage (V_{OC}); fill factor; and efficiency.

4.4. Conclusion

The effect of PEDOT:PSS film thickness on hybrid solar cells with PEDOT:PSS films secondary doped using different methods: co-solvent-added and post-treated cells was examined, together with HSCs with pristine PEDOT:PSS films. It was found that the optical properties for pristine and co-solvent-added films were similar, but the post-treated films had a lower index of refraction and a higher extinction coefficient (indicating higher absorption) than the other two films, as a result of a change in stoichiometry between PEDOT and PSS. Through modeling the reflectance spectra at different thicknesses and obtaining the reflectance of the air/PEDOT:PSS and PEDOT:PSS/silicon interface, the quantum efficiency could be simulated. This simulation is significant in the optimization PEDOT:PSS/silicon

HSCs and in precisely uncovering how different properties influence the performance. It was identified that after post-treatment the EQE decreases significantly due to absorption and resistive effects of the film. After analyzing the J_{sc} determined from EQE measurements, J_{sc} was found to decrease after post-treatment despite its higher sheet conductivity shown in Chapter 3. The optimal J_{sc} occurred at a film thickness where decreasing reflectance was overcome by increasing absorbance and perpendicular resistance of the film. Using internal quantum efficiency to separate the electronic loss mechanisms from the optical measurement showed that the perpendicular resistivity of the post-treated film was 75% and 64% higher than the pristine and co-solvent-added films, respectively. This work therefore shows a delicate balance when applying PEDOT:PSS to optoelectronic devices and that there is a large anisotropy between PEDOT:PSS sheet and vertical resistivity through the film. The present analysis exemplifies the insensitivity of solar simulated JV curves and difficulty in detangling and identifying properties associated in changes seen in performance. Moreover that the conductivity of the PEDOT:PSS film does not significantly increase the collected photocurrent or the short-circuit current, and the observed efficiency improvement is the result of other processes, such as changes in absorbance, and open-circuit voltage as will be discussed in Chapter 5. The models used in this chapter can be easily applied to other systems of inorganics simply by obtaining the reflectance of the material, or used with other polymers by obtaining the complex index of refraction though transmittance measurements. This method provides a computational method to disentangle the optical and electronic properties of heterojunction solar cells which is very difficult through other methods and should be the first phase in optimizing or testing new systems.

5. PEDOT:PSS – n-Silicon Heterojunction properties

5.1. Introduction

The interface between the p-type material and n-type material is the most important feature of the solar cell circuit. It is at this critical junction where the built-in-potential exists, causing the electromotive force that powers the circuit, and where electron-hole pairs are separated to produce photo-carriers. In heterojunctions this sensitivity is magnified since there are usually changes in lattice constants that cause anomalies in the bonding at the junction and possible dislocations contributing to surface states and trap-assisted-carrier recombination.[24] Heterojunction materials also differ in electron affinities and band-gaps that lead to conduction and valence band offsets where highly localized electric fields and charge densities exist. A consequence of this is that photogenerated electron and hole charge carriers can experience unequal potential barrier heights and charge transfer kinetics. Precise control of the choice of material and fabrication processes can help to limit these impediments, and the benefit of having controlled light absorption at the junction and material choice (offered by the heterojunctions) often outweighs the depredating effects. In this Chapter, the interface between PEDOT:PSS and n-silicon is examined with the goal to obtain higher open-circuit voltages. Three different approaches were used to determine the influences on HSCs: (1) the introduction of a passivating silicon oxide layer with different thickness; (2) post-treatment and the removal of PSS to effect changes in effective density of acceptor states, N_A, of the emitter; and (3) the placement of a chromophore and semiconducting polymer at the interface.

In a solar cell, the strength of the electric field at the junction is the force (per unit charge) that provides the potential to drive the photocurrent through a resistive load in a reverse-bias direction. The strength of this build-in-potential can be determined at zero current flow, or when an applied forward bias is of equal strength. This open-circuit potential, V_{OC}, is given by: [14,23,25]

$$V_{oc} = \frac{mkT}{q} \ln\left(\frac{J_{sc}}{J_0}\right) \tag{5.1}$$

where J_{sc} is the short-circuit current density (the current under illumination when the applied bias is set to zero), q is the charge of an electron, m is the ideality factor , k is the Boltzmann constant, T is the temperature, and J_o is the dark saturation current which depends directly on the junction characteristics. In the inorganic-organic heterojunction solar cell, the organic layer acts as a p-type layer analogous to p-doped

silicon in a conventional solar cell. However, the highly doped nature of PEDOT:PSS makes it act as a hole transport medium and the PEDOT:PSS is often described as quasi-metallic. Conceptually, the junction with n-type silicon is more similar to a Schottky junction than an ideal p-n junction.[130] Schottky diodes tend to have a higher dark saturation current than ideal diodes causing a lower open-circuit voltage, and they cannot adequately explain the high V_{OC} seen in HSCs.

The Schottky junction formed when a n-type semiconductor is brought into contact with a conductor results in the migration of electrons across the junction into the conductor to minimize the potential energy of the system as described in Chapter 1. In so doing, the electrons create an electric filed at the surface and leave the donor atoms, located about one diffusion length away from the surface, positively ionized opposite to those of the bulk silicon. The resulting space charge region in silicon, if strong enough [band bending, $q\psi_{bi} > E_g\text{-}2(E_c\text{-}E_F)$, where], is referred as a strong inversion layer that effectively generates a depletion region existing solely within the semiconductor.[23] In this region, the field is especially strong, and transport across this field is dominated by minority carriers (holes in the case of n-type silicon). However, such inversion layer does not typically form in a silicon-metal junction due to defects, causing a high density of surface states in the semiconductor band-gap and Fermi-level pinning limiting the band bending to $E_g/2$.[131,132] Despite this, this inversion layer have been identified in a PEDOT:PSS-n-Si hybrid solar cell.[130]

The nature of the Schottky junction depends on the work function of the conducting material, ϕ, electron affinity of the semiconductor, χ, and the amount of band bending, ψ_{bi}, (difference between Fermi-level and conduction band). The reverse saturation current is limited by thermionic emission, J_e, introduced in Section 2.2, Equation 2.1, and is only slightly dependent on the diffusion length, L_p, mobility, μ_p, and doping concentration N_D.[13] This Schottky junction model alone cannot account for the high open-circuit voltages seen in these HSCs and therefore they must not be limited by thermionic emission or recombination.[13,133] Jackle *et al.* identified a relation between silicon doping concentration and the reverse saturation current in HSCs and they found that it was better modeled using a p^+-n (where the $^+$ denotes heavy doping) junction and the ideal diode equation. For an ideal diode or solar cell, the saturation current J_{diff} is dominated by the diffusion of minority carriers.[14]

$$J_{diff} = q\left(\frac{D_n}{L_n}n_p + \frac{D_p}{L_p}p_n\right) \tag{5.2}$$

where L_n and L_p are the diffusion lengths for electrons and holes respectively, and n_p is the equilibrium concentration of electrons in the p-doped layer and p_n is the equilibrium concentration of holes in the n-doped layer, D_n and D_p are the diffusion constants for electrons and holes respectively and they are related to the respective mobility μ_n or μ_p through the Einstein relation.

$$\frac{D_{n,p}}{\mu_{n,p}} = \frac{kT}{q} \tag{5.3}$$

PEDOT:PSS is a hole transport medium with a large LUMO and effectively no conduction electrons. Equation 5.2 can be rewritten as: [13,133]

$$J_{diff} = \frac{n_i^2 \mu_p kT}{L_p N_D} \tag{5.4}$$

where k is the Boltzmann constant, μ_p is the hole mobility, n_i is the intrinsic carrier concentrations, and N_D is the donor doping concentration. Unlike thermionic emission, it can be seen that the diffusion current is inversely proportional to the doping of silicon.

For a Schottky junction, the saturation current is driven by thermionic emission, J_e as described in Chapter 2. The electrons flow from the semiconductor to the metal through electron drift in a similar relationship as a respective heavily p-doped side and normally n-doped side (p^+-n junction), such that the ideal diode equation can be applied for both types of junctions by substituting either J_e, or J_{diff} for the appropriate junction.[14,133]

$$J = J_{e,diff}\left(\exp\left(\frac{qV}{mkT}\right) - 1\right) \tag{5.5}$$

where kT/q is the thermal voltage and m is the ideality factor. In a typical J-V test, the value of J_o can be determined by linear extrapolation of dark J(V) curve to V=0 and the ideality factor can be obtained from the slope of V vs natural log of J.[13,19,130,133] Under ideal conditions, the ideality factor is unity (i.e. m=1) for all voltages, which indicates that the net current flow is dominated by drift of thermally generated minority carriers and it should be proportional to the radiative-recombination rate R that is material and dopant dependent ($R \propto np$) where n and p are the number of electron or hole chare carriers respectively.

However, typically Shockley-Read-Hall recombination occurs in heterojunctions when defects in the band-gap and surface states in the space charge region are involved, assuming that the mid-gap state recombination rate scales with $R = \frac{np-n_i}{(n+p)\tau}$, where τ is the carrier lifetime, n_i is the intrinsic carrier consentation, and n and p are the carrier concentrations.[28] These other pathways allow for an increased recombination, a decrease in shunt resistance, and an increase in the dark saturation current, causing *m* to increase and to approach 2 under strong recombination in the space charge region. In the heterojunction, the ideality factor can be greater than 2 where recombination can be increased by tunnelling enhanced by local electric field.

Experimentally, different values of *m* are observed at different voltages. At higher voltages carriers are injected across the boundary, bulk radiative recombination dominates, and $m \rightarrow 1$. At low voltages, the current is driven mostly by recombination in the space charge region at the junction, and the ideality factor increases. In this low-voltage regime, a cell with a low shunt resistance will have increased current density. Because of the two different processes driving the observed current, a two-diode model is used:

$$J_d = J_o\left(\exp\left(\frac{qV}{m_1 kT}\right) - 1\right) + J_{scr}\left(\exp\left(\frac{qV}{m_2 kT}\right) - 1\right) \tag{5.6}$$

Where m_1 and m_2 are the ideality factors for both high and low voltage regimes respectively and J_{scr} is the recombination current within the space charge region and is given by:

$$J_{scr} = \frac{qn_i w_n}{\sqrt{\tau_n \tau_p}} \tag{5.7}$$

where $\mathcal{W}_n$ is the width of the depletion region in silicon. In conventional cells, the dark saturation current density can be as low as 10^{-14} A/cm^2 allowing for high V_{oc} (0.8 V) and high efficiencies, whereas for Schottky solar cells, the dark current density is ~10^{-7} A/cm^2, resulting in a low V_{oc} of ~0.3 V.[25,28,72]

The low-temperature processing of PEDOT:PSS–n-Si solar cells allows greater interface control and the accommodation of molecular passivation layers such as oxides[134] or methyl/allyl termination.[135,136] The termination of dangling bonds is dramatically reduced through covalent bonding between the silicon surface atoms and the passivation layer, which generates upward band bending and stops the Fermi-level pinning effect.[27,136] PEDOT:PSS–n-Si is a good model system to study polymer –

inorganic heterojunctions since PEDOT:PSS has little absorption, or generation of charge carriers. PEDOT:PSS acts as a minority carrier (hole) collector while blocking majority carrier (electrons) due to the high LUMO and the presence of an inversion layer at the interface and can be determined electronically.

5.2. Experimental Details

The HSC's were prepared on 1×1 cm^2, one-sided polished, n-type phosphorus-doped silicon (100) substrates (200 μm thick) with a resistivity of 1-2 Ω cm (Virginia Semiconductor Inc.). The substrates were cleaned by sonication in acetone and isopropyl alcohol and then thoroughly washed with filtered high-resistivity water (18.2 MΩ-cm). Co-solvent-added PEDOT:PSS solution was prepared by adding ethylene glycol (7 wt%) to PEDOT:PSS (Clevios™ PH1000), along with a fluorosurfactant (0.25 wt%).[137]

SiO_x Studies:

The native silicon oxide layer on the Si(100) substrate was removed by submersing the substrate in 2 vol% hydrofluoric acid for 10 minutes at room temperature and it was then rinsed with deionized water. Aluminum was immediately sputter-coated on the back side of the substrate to form the back electrode by using a magnetron sputtering system (EMS575X). For junctions on H-terminated Si substrates, the PEDOT:PSS solution was deposited on the front side immediately after the Al sputter-coating. PEDOT:PSS solution (80 μL) was spin-coated onto the silicon substrate at 6000 RPM, allowed to relax for 5 minutes, and then placed on a hot plate for curing at 110°C for 10 minutes. For junctions on SiO_2 passivated substrates, the substrates were washed with deionized water and allowed to oxidize naturally in a clean hood at room temperature for 2 hours, then the polymer was deposited identically as those without the oxide layer.

Post-treatment Studies

Post-treatment was conducted by adding 80 μL of a binary mixture of 50 vol% methanol (Sigma Aldrich, ≥99.9%) and 50 vol% ethylene glycol (VWR, ≥99.0%) onto the cured PEDOT:PSS film. The solution was allowed to penetrate the film for 2 minutes, and then it underwent spin-coating at 6000 RPM for 2 minutes and curing at 110 °C on a hot plate for 10 minutes.

P3HT Studies

Electronic grade rigioregular Poly-3-hexylthiophene (P3HT), m_n: 54000-75000 (Sigma Aldrich) was dissolved in selected solutions with different vapour pressures (VP) and boiling points (BP): chloro-benzene (VP: 9 Torr; BP: 131° C) , chlorobenzene (VP: 1.3 Torr; BP: 131° C), 1,2-dicholorobenzene (boiling point: 180° C), and 1,2,4-trichlorobenzene (VP: 1 Torr; BP: 214° C). The films were made by using 60 mg/ml solutions by dynamically applying 20 µl to a Si surface with native oxide, spinning at 6000 RPM for 20 seconds to obtain a 10-nm-thick film, or 3000 RPM for 20 seconds for a 30-nm-thick film, or 3000 RPM for 5 seconds for a 50-nm-thick film, or 3000 RPM for 5 seconds repeated twice for a 80-nm-thick film, each followed by 2-second acceleration to 12000 RPM to remove any excess solution. The ethylene glycol co-solvent-added PEDOT:PSS solution was then added to the P3HT layer as mentioned above.

Quartz substrates (SPI supplies), 10×10 mm^2 in size and 1 mm thick, were used for UV-Vis experiments. They were cleaned by sonication in acetone and isopropyl alcohol and then thoroughly washed with filtered high-resistivity water (18.2 MΩ-cm). Absorbance/transmittance measurements were conducted by using a Perkin Elmer Lambda 1050 UV-NIR spectrophotometer. A Filmmetric F40-UV thin film analyzer was used to measure film thickness, which was further verified by using a KLA Tencor P-6 profilometer. Raman spectra were collected by using a 785 nm laser in a Bruker Senterra Raman confocal microscope. Atomic Force Microscopy (AFM) images were collected by using an Asylum Research Cypher microscope.

5.3. Results and Discussion

5.3.1. Silicon Passivation Layer

The silicon oxide layer, SiO_x, at the interface between the PEDOT:PSS and n-Si substrate is examined since it acts as a passivation layer that will affect the open-circuit voltage of HSCs through its influence on carrier recombination. Figure 5.1 shows a comparison between HSCs prepared on H-terminated silicon with a native oxide layer that was allowed to grow for 2 hours before the PEDOT:PSS layer was applied and on H-terminated silicon where SiO_x was not allowed to grow. From the dark saturation JV curve of the passivated cell, the magnitude of the current is lower and the slope is higher with alower ideality factor (*m*) than that without passivation. Moreover the transition to diffusive behavior

(change in slope occurring at above 0.4 V) occurs at a lower voltage, which is indicative of a longer carrier lifetime and less recombination.

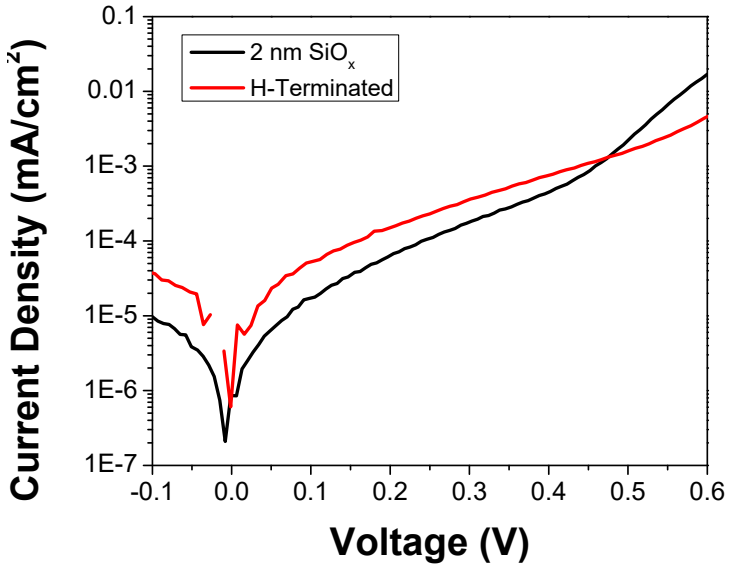

Figure 5.1: Dark saturation current vs applied voltage curves for cells with a H-terminated silicon substrate, and a 2-nm-thick SiO_x passivation layer on the silicon substrate.

The SiO_x passivation layer limits the amounts of defects and dangling bonds and the extent of Fermi level pinning at the midpoint of the band-gap ($E_g/2$), and it is believed to be beneficial to the separation of electron-hole pairs created in the space charge region. Thin, nm-thick, oxide layers have been reported to easily allow electron tunneling.[27,138] He *et al.* found that as the native-oxide passivation layer in HSCs became thicker than ~2 nm, it could act as an insulating layer, similar to a parallel plate capacitor, causing a potential drop and increasing resistance.[134]

Oxide growth occurs naturally in ambient conditions and it is accelerated at elevated temperatures or in high humidity environments. This sensitivity suggests that care must be taken in controlling the growth of this layer.[139] In our studies involving Raman spectroscopy, differences in the PEDOT peak shape and position were evidently dependent on whether the PEDOT:PSS film was applied to a H-terminated or a SiO_x passivated silicon substrate. Changes in the Raman features therefore provide a quick method of characterizing the underlying oxide layer. Figure 5.2 shows a large peak shift in the main C_α=C_β band from 1415 to 1428 cm^{-1} and a smaller blue shift of the C_α=C_α band at 1255 cm^{-1}, as well as an increase in the relative intensity of the C_β–C_β band at 1365 cm^{-1} with increasing thickness in the oxide

layer. To confirm that this shift is not a result of changes in the bulk electronic levels at the interface of silicon, the experiments were repeated on p-type silicon and identical results were obtained, confirming the change is not a result of charge transfer and de-doping of PEDOT:PSS. Instead, the observed changes are associated with molecular strain of the polymer caused by the hydrophobic nature of H-terminated silicon as opposed to the hydrophilic silicon oxide.

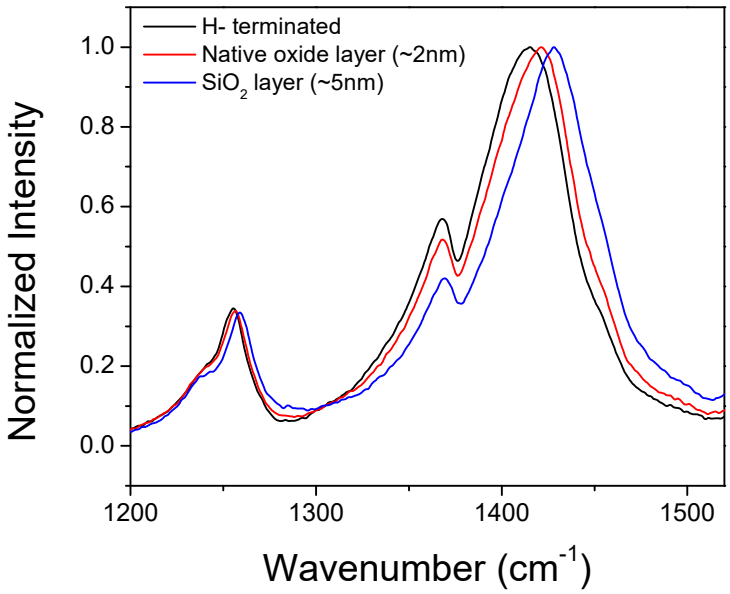

Figure 5.2: Raman spectra of PEDOT:PSS on silicon with different silicon oxide layer thicknesses.

It has been shown that organic molecules chemically binding onto the silicon substrate offer oxide growth resistance, [27,135,138] However, dynamic changes in the Raman spectrum of PEDOT:PSS on silicon with the native oxide layer removed can be observed with the growth of the underlying SiO_x layer. Figure 5.3a) shows the shift in the $C_\alpha=C_\beta$ band on H-terminated silicon over time for co-solvent-added films. The blue-shift in the peak maximum of the band follows an exponential trend with increasing time, as shown in Figure 5.3b), with an initial rate constant of $4x10^{-3}$ cm^{-1}/h^{-1}, that follows an increasing trend for the first ~10 hours before levelling out. The observed trend is in good agreement with the growth of the native oxide on bare silicon,[139,140] indicating that PEDOT:PSS offers little oxide growth resistance because the bands appear to shift toward positions corresponding to PEDOT:PSS on thick oxide layers, and

that silicon continues to oxidize gradually in ambient conditions.[‡] The formation of an oxide layer takes a couple of hours and should occur in a clean and controlled environment to be effective and reproducible. Quickly adding PEDOT:PSSS solution to h-terminated silicon, spin coating and annealing it during the oxide growth results in contamination and cell made in this fashion will be referred to as having a contaminated native oxide layer.

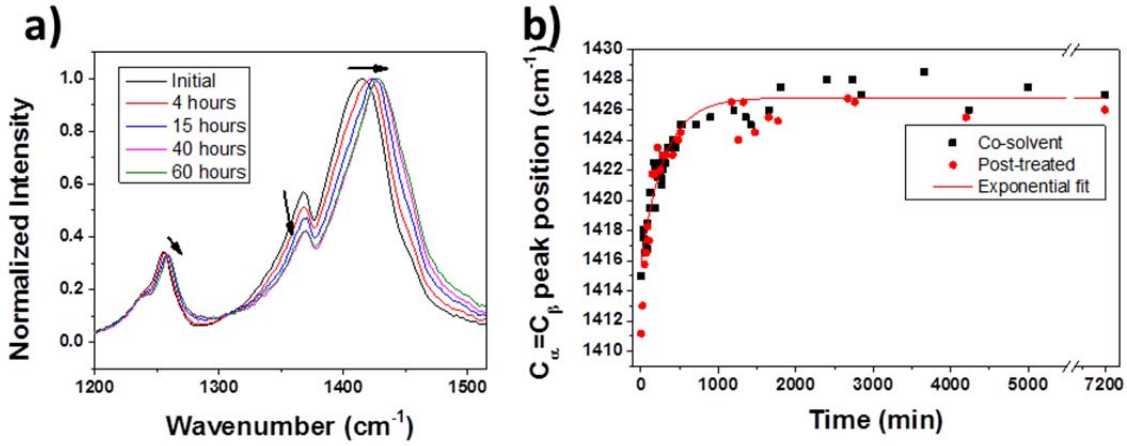

Figure 5.3: a) Evolution of the Raman spectrum of PEDOT:PSS on Si substrate over time, following the growth of the underlying silicon oxide layer. b) Changes in C_α=C_β peak position with time.

The JV characteristics were tested during the growth of the oxide layer under a co-solvent added PEDOT:PSS film (Figure 5.4a). An HSC was fabricated on a silicon substrate shortly after the substrate was treated with HF. The open-circuit voltage is found to decrease logarithmically with increasing oxidization time, while the fill factor also shows an overall downward trend. Figure 5.4b) shows increasing dark saturation current with time, along with the decreasing slope (between 0.1 and 0.4 V) of the curves, representing higher ideality factor, which suggests greater recombination through defects.[14,23,28] This decrease in performance with oxide growth is inconsistent with the increased performance seen when PEDOT:PSS is applied to pre-grown oxide (Figure 5.1). This is explained by the contamination of the oxide

[‡] Raider *et al.* showed that impurities are rapidly absorbed on silicon substrates after etching in HF, and that more carbon is initially absorbed on an etched substrate than one with an oxide present.[140] Moreover the impurity layer is found to decrease after oxidation had already been initiated.

layer. As the layer grows, it incorporates fragments and other impurities from the PEDOT:PSS, increasing the number of defects, resulting in Fermi-level pinning and higher Shockley-Read-Hall recombination.[24]

Table **5**.1: J(V) characteristics during the growth of SiO_x under a co-solvent-added PEDOT:PSS film.

Time (h)	Jsc (mA/cm^2)	Voc (V)	FF	Efficiency (%)
0.4	15.9	0.451	0.562	4.04
1.4	16.1	0.446	0.539	3.88
3.3	16.0	0.430	0.519	3.66
5.3	15.6	0.435	0.546	3.71
7.4	15.6	0.432	0.534	3.59
19.4	15.1	0.429	0.520	3.37
25.4	16.0	0.426	0.503	3.42

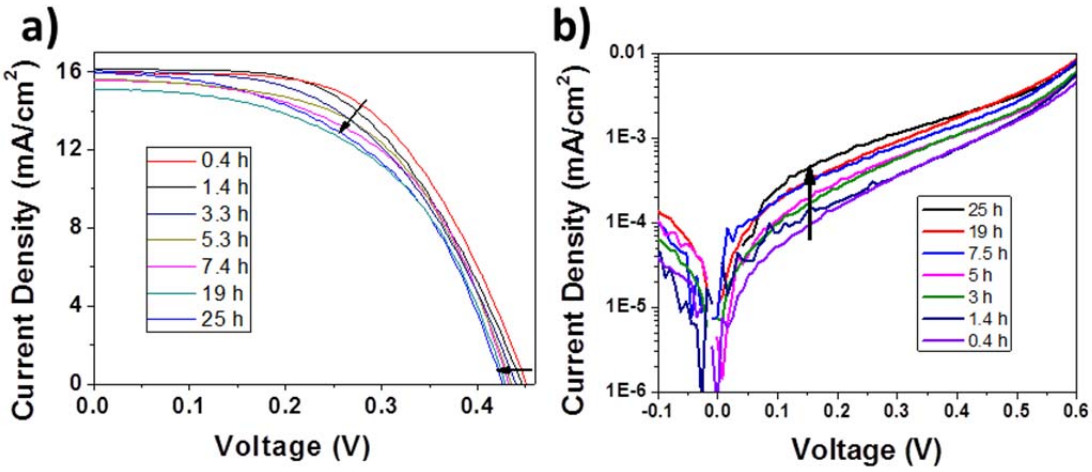

Figure 5.4: a) Illuminated J(V) curves and b) Dark saturation curves over time with the growth of silicon oxide layer under a co-solvent-added PEDOT:PSS film.

It has been well documented that covalently bonded passivating layers have an effect on the electron affinity, causing band bending either up or down depending on the charge and molecular polarization.[27,134,141] Figure 5.5 shows a schematic representation of the Schottky barrier junction for PEDOT:PSS on H-terminated Si, Si with contaminated native oxide, and Si with SiO_x interfaces. The growth of the oxide under the PEDOT:PSS layer could result in a range of bond lengths and orientations, disrupting any long-range order and could explain the changes seen in the Raman data (Figure 5.3). Moreover, contamination

of the surface from anionic PSS[‡] can leave the surface negatively charged and can act as electron donors, limiting band bending and the extent of the depletion layer as indicated by the decrease in current density (J_o) and open circuit voltage (Voc).[25] On the other hand, allowing for controlled native oxide growth on the surface before applying the polymer results in better surface passivation. Electron loss from dangling bonds traps positive charges and provides a positive surface dipole, blocking recombination, assisting hole transport and insuring a strong inversion layer so electron back transfer is minimized.[14] This sensitivity to surface defects exposes the challenges observed by others in obtaining high V_{OC} and efficient cells on nanostructured silicon[142,143,144].

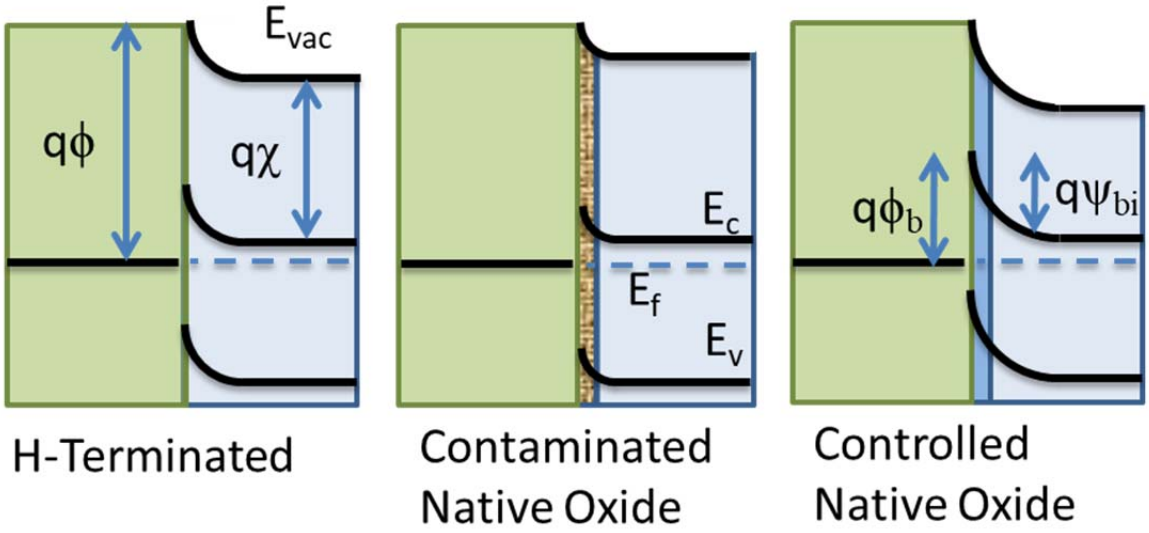

Figure 5.5**:** Energy band diagrams showing band bending at the interface between PEDOT:PSS and different n-silicon substrates: (Left) An H-terminated surface contains dangling bonds, and an increase in the number of surface states resulting in mid-gap Fermi-level pinning. (Center) A contaminated oxide layer results in more charged defects and a decrease in band bending. (Right) A controlled native oxide layer results in the greatest band bending and an inversion layer through a reduction in space charge region recombination. q is the electronic charge, ϕ are the work function of the metal, χ is the electron affinity of the semiconductor, E_{vac} is the vacuum level, E_f is the Fermi level, and $\Psi_{bi} = \phi - E_f$ is the built in potential and $\phi_b = \Psi_{bi} + |E_c - E_f|$ is the barrier height.

[‡] It was shown in Chapter 2 that PSS remains on the silicon surface after the film is removed.

5.3.2. Post-Treatment

As mentioned in Chapters 3 and 4 (Figure 3.10, and Figure 4.13), the open-circuit voltage obtained from illuminated IV curves for post-treated films was on average higher than those not. Moreover, after the post-treatment higher internal quantum efficiency was obtained in the short-wavelength region, which suggests greater collection of photocarriers created near the junction (Figure 4.10).[‡] The dark saturation current of the top performing co-solvent-added and post-treated cells are shown in Figure 5.6.

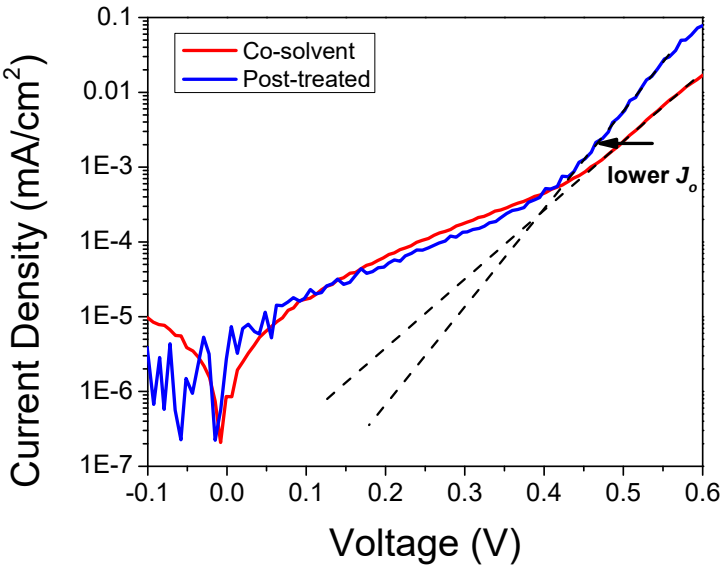

Figure 5.6: Dark saturation currents density as functions of voltage for cells made from co-solvent-added PEDOT:PSS films and post-treated films.

Linear extrapolation of the current density in the high forward bias range to V=0 indicates that the post-treated cells have a smaller J_o (1.5×10^{-9} mA/cm^2) than the co-solvent-added cells (5.8×10^{-8} mA/cm^2) and a smaller ideality factor indicated by the larger slope than that for the co-solvent-added cells, shown as dashed lines. It is well known that the dark saturation current is dominated by majority carrier injection into the anode material (electrons injection into PEDOT:PSS),[24,130,145] a lower value after post-treatment

[‡] A higher IQE in this region is indicative of low recombination through a lower majority carrier (electron) charge transfer coefficient, which also manifests itself as a higher potential barrier.[13]

indicates stronger inversion and electron blocking. Moreover, the transition to diffusive behaviour occurs at a lower voltage after post-treatment. Together these indicate that Shockley-Read-Hall recombination decreases and the charge carrier lifetime increases within the space charge region as indicated by Equation 5.6. However, the current density at lower voltage that is indicative of shunt resistance is similar for both films, which suggests similar majority charge carrier transfer at the interface.

Post-treatment has a large effect on the interface. As described in section 2.7.3. the removal of PSS from the interface allows the film to fall within the Schottky-mott regime causing the PEDOT work function to feel greater influence from the inorganic fermi-level.[62,65] This together with the change in blend stoichiometry of PEDOT after post-treatment and the increase in positive bi-polaron modes as evidenced by Raman and UV-vis experiments would indicate a strong change in interfacial potential. These effects results in the effective density of acceptor states, N_A to increase,[146] and causes an increase the inversion layer and decrease the electronic coupling between PEDOT:PSS and n-silicon. Future work should be conducted with different PEDOT:PSS grades to conclusively determine the effect that doping density has on the space charge region.

5.3.3. Poly(3-hexylthiophene)

Regioregular Poly(3-hexylthiophene) (P3HT) is a large band-gap semiconducting polymer with interesting self-organizing properties and different crystalline structures from PEDOT:PSS. P3HT is an ambipolar conductor and is non-conducting in its natural state and only becoming conducting upon doping and the addition of excess charges.[147,148] Morphological studies were conducted to produce highly crystalline P3HT, with good charge-transport properties, to be placed as an interfacial layer between PEDOT:PSS and n-type silicon with a native oxide layer.

The drying or relaxation rate of polymers has a significant effect on the crystal structure and thus conductivity.[149,150,151] For this reason, solvents with different vapor pressures and boiling points were tested to prepare crystalline regioregular P3HT, and these solvents include (in the order of increasing boiling point) chlorobenzene (CB), dichlorobenzene (DCB), and trichlorobenzene (TCB). The AFM and optical birefringence images of P3HT in these solvents all exhibit different morphologies and they are shown in Figure 5.7a). All solutions showed regular features but on different length scales. Low boiling point CB resulted in a short range chain structure whereas high boiling point TCB had much longer range structure with well-defined nanofibers a couple of micrometers long and <10 nm thick. The corresponding phase images shown in Figure 5.7b) show that CB has a homogeneous surface with the presence of some isolat-

ed polymer aggregates, while TCB exhibits straight, aligned bundles of fibers. DCB appears to have large regular elongated 2D features on the same scale as TCB, while the 1 μm scan indicates that they consist of entangled and agglomerated chain structures like those of CB. With the onset of large regular surface features, like those seen when DCB or TCB is employed, birefringence patterns can be observed using a cross polarizer (Figure 5.7c). Birefringence appear due to anisotropy and crystallization of a polymer film.[45,74] They are likely observable due to the higher crystallinity of DCB and TCB and inherent polymer structures with high orientation, like those shown in Figure 2.13.[118] There was no observable Birefringence for CB, the small features visible in the microscopic image are surface features.

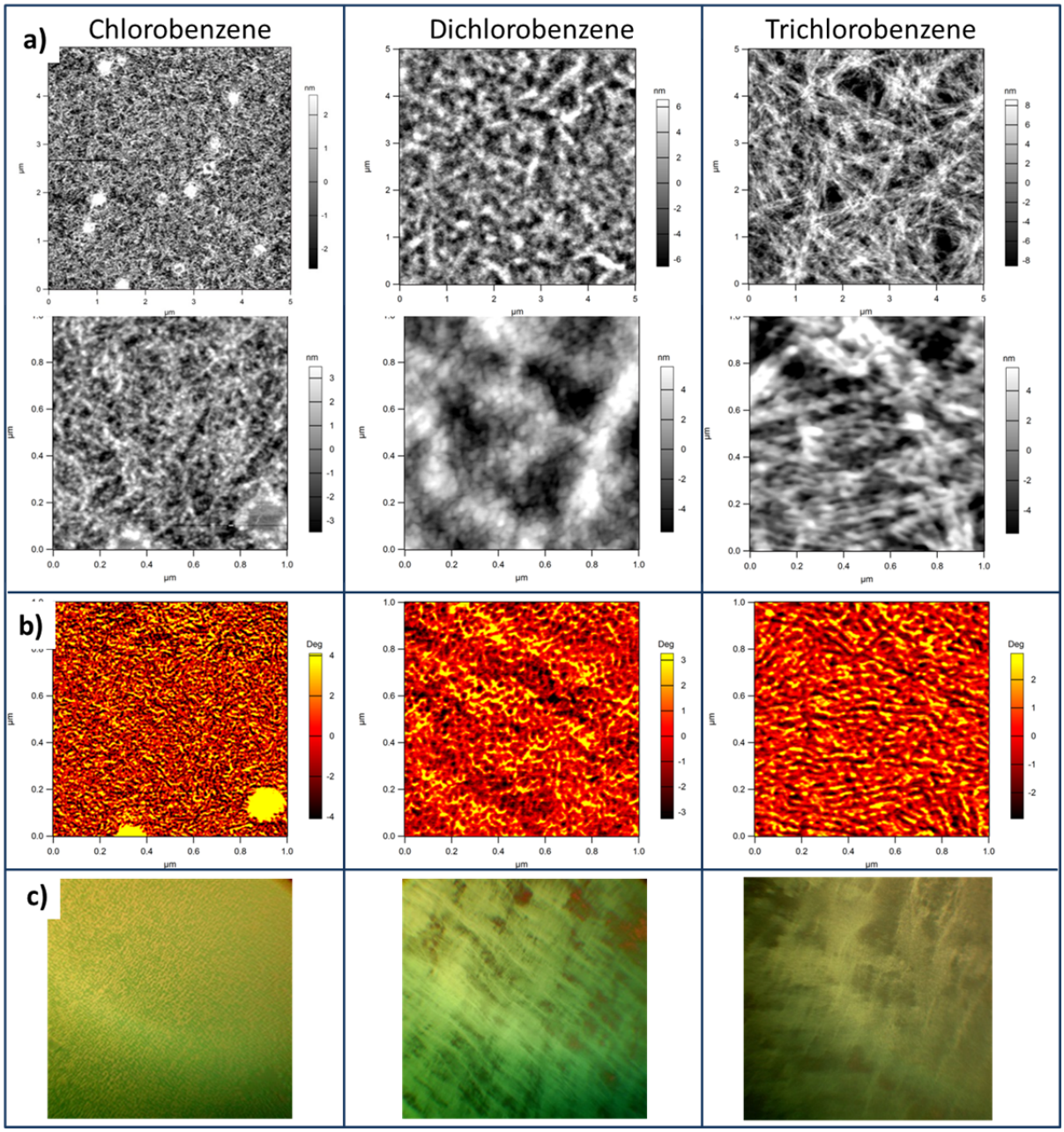

Figure 5.7: a) Tapping-mode AFM images of P3HT films prepared with chlorobenzene (left), dichlorobenzene (middle) resulting in surface features, and trichlorobenzene (right) resulting in nanofibers; b) their corresponding phase images; and c) optical cross polarized birefringence maps of these films on a silicon surface (50X magnification).

The extent of π-π stacking and crystallization can be identified through the UV-Vis absorption spectra as shown in Figure 5.8a). The broad absorbance band at ~550 nm corresponds to the π-π* (S_o –

S_1) transition of the polymer chain.[74,152] The red shift of the absorbance maximum with cosolvents with decreasing vapour pressure and increasing boiling point reflects an increase in conjugation length and decrease in kinks or twists of the backbone.[73] The lower-energy vibrionic feature at 620 nm indicates strong π-stacked aggregates,[153] while the higher-energy tail of the spectrum is associated with unaggregated, disordered chains that give rise to the formation of intrachain states.[74,152,154] The two lower-energy peaks observed near 620 nm and 570 nm correspond to the $A_{0\text{-}0}$, and $A_{0\text{-}1}$ vibrationally excited states, respectively.[‡] The Spano model uses the intensity ratio between these peaks to estimate the aggregate content and degree of intrachain order:[155]

$$\frac{I_{0-0}}{I_{0-1}} = \left(\frac{1 - \frac{0.24W}{E_p}}{1 + \frac{0.073W}{E_p}} \right)^2 \tag{5.8}$$

where E_p is the main intermolecular vibration energy, and W is the free exciton bandwidth within the crystalline domains. Qualitatively, the TCB results in the highest degree of crystallinity and the lowest amount of disordered unaggregated chains. This is further supported by their corresponding Raman spectra in Figure 5.8 b), which shows a broadening of the thiophene C=C ring breathing mode at 1450 cm^{-1} and a relative intensity increase in the thiophene C-C band at 1372 cm^{-1}. The decreasing trend in this (C=C/C-C) intensity ratio from CB to DCB to TCB is attributed to an increase in the corresponding conjugation length.[152]

[‡] The subscripts 0-0 and 0-1 correspond to the transition from the ground state S_0 to the vibrational states v=0, 1, 2 of the excited state or exciton S_1.

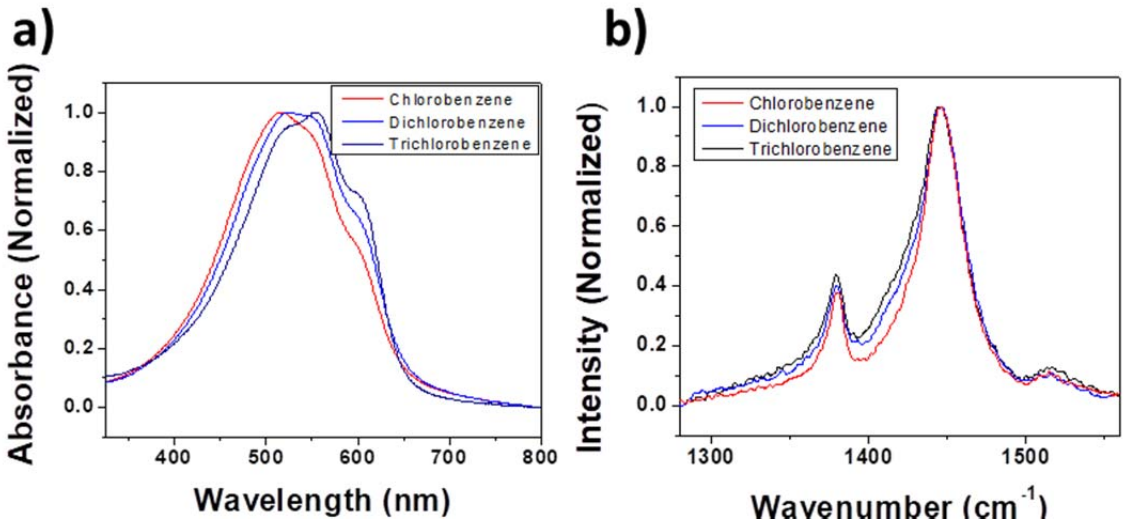

Figure 5.8: a) UV-Vis absorption spectra and b) Raman spectra of P3HT prepared using CB, DCB, TCB.

The crystalline orientation of the polymer is important and crystallization is preferred along the charge transport direction, parallel to the applied field.[33] Crystalline polymer chains with fewer defects result in greater orbital overlap, such as π-stacking, which facilitates inter-chain charge transport. The charge mobility in P3HT is therefore strongly dependent on the morphology.[70] Despite the high mobility in the one-dimensional crystalline nanostructures, the macroscopic mobility of the film is determined by the twisted chains in the amorphous regions and the level of nanocrystal interconnectivity.[154] Himmelberger *et. al.* has shown that local aggregation over very few chains is a preferred mesoscopic structure and that extended crystallinity is not necessary (explaining the excellent conductivity of PEDOT:PSS).[156] Charges propagate mainly along the polymer backbones but are not as easily isolated and trapped at grain boundaries.[157] Films with small crystallites and long interconnecting chains acting as bridges can have higher mobility. For this reason, the smaller crystallites and more homogeneous film coverage obtained for the DCB sample was chosen for the HSC experiments.

The ability of P3HT to act as a chromophore and the effect of its thickness on short-circuit current density is examined using quantum efficiency measurements. Figure 5.9a) shows the EQE curves of a DCB P3HT nanofiber layer with different thicknesses (of 10 nm, 30 nm, 50 nm and 80 nm) between a 80 nm co-solvent added PEDOT:PSS and Si substrate. Evidently, the EQE in the 400-600 cm^{-1} region decreases as a result of greater absorbance of increasing P3HT layer thickness and follows the absorbance profile of DCB (Figure 5.8a), indicating that photons absorbed by P3HT do not contribute to the photocurrent. Since the addition of even a thin layer of P3HT would reduce the photocurrent across this region,

it is unlikely that the addition of a chromophore at the interface could extend the absorbance spectra of HSCs. The creation of excitons and separation into electron-hole photocarriers at the interface do not occur, validating the Schottky model and that the space charge region is confined to the silicon base. For wavelengths larger than 650 nm, the EQE increases with thickness up to 50 nm and then decreases for larger thicknesses.

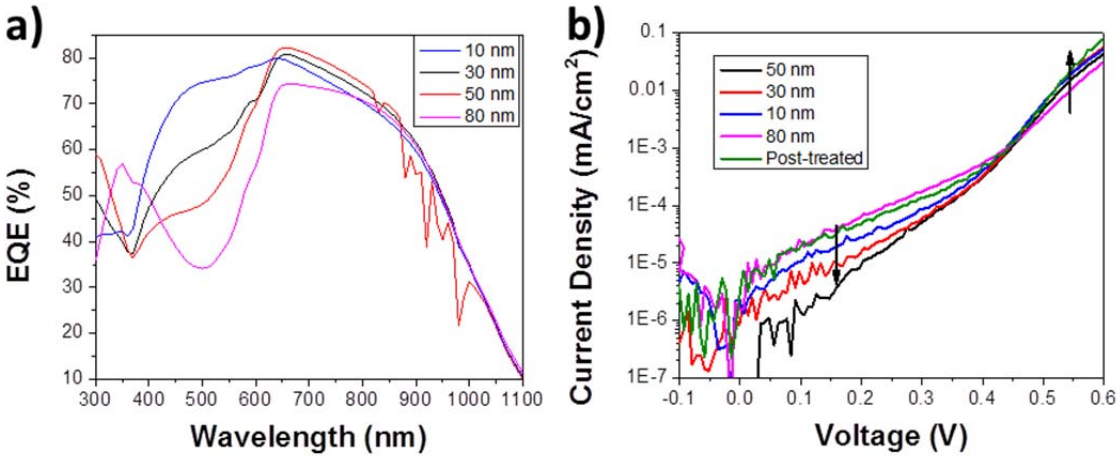

Figure 5.9: (a) External quantum efficiency of HSCs and (b) dark saturation current with P3HT interfacial layers of different thicknesses.(The 50 nm sample shows interference effects at longer wavelengths often seen in untextured solar cells)[90]

The dark saturation current is used to examine the interfacial effects introduced by a P3HT layer (Figure 5.9 b). Up until 50 nm the current density is found to decrease in the low forward bias region (0-0.4 V) with increasing P3HT layer thickness (as marked by the arrow in the low bias region), indicating that the shunt resistance of the cells increases with increasing thickness. The slope has become steeper (indicating a lower ideality factor) until the P3HT layer thickness reaches 50 nm above which layer thickness the slope decreases. The J_o values obtained from linear extrapolation of the curves in the mid forward bias region (0.4 V – 0.6 V) are shown in Table 5.2. Evidently, J_0 for cells with P3HT layer thinner than 80 nm are similar to that for the post-treated cells discussed above. There is also a slight increase in the current density in this region with decreasing thickness, suggesting a corresponding decrease in the series resistance (as marked by the arrow at high forward bias) with increasing P3HT layer thickness. (The J_{sc} for the highest performing post-treated cell, (30.48 mA/cm^2) is higher than the maximum of 28.3 mA/cm^2 discussed in chapter 4 because of the tendency of solar simulated J_{sc} to produce inflated values. (This is mainly due to changes in the potential barrier under low-intensity monochromatic illumination

and AM1.5G illumination. [158]) The increasing EQE above 650 nm, increasing shunt resistance, and similar J_o are indicative of better charge transfer at the interface and increasing carrier lifetime with increasing P3HT layer thickness below 80 nm. Figure 5.10a) shows the corresponding illuminated J vs V curves of HSCs containing a P3HT interface layer with different layer thicknesses. Significantly higher open-circuit voltages were obtained with an interfacial layer thinner than 80 nm than that without the P3HT interface layer. The highest achievable voltage, 0.592 V, was obtained with a P3HT layer thickness of 50 nm. However, significant effects from the series resistance resulting from increasing layer thickness that cause reduction in the fill factor are observed, which accounts for the poor performance when thicker interfacial films are used. If the conductivity of P3HT could be increased through, for example, doping, the series resistance could possibly be reduced, which would alleviate this adverse effect.

Table 5.2: J(V) characteristics of different thickness P3HT layer under PEDOT:PSS.

Thickness (nm)	J_o (mA/cm^2)	Voc (V)	Jsc (mA/cm^2)	FF	Efficiency (%)
80	3.2×10^{-8}	0.521	23.35	0.239	2.91
50	1.7×10^{-9}	0.592	28.40	0.402	6.75
30	1.5×10^{-9}	0.576	25.16	0.542	7.85
10	2.7×10^{-9}	0.565	28.88	0.628	10.25
Post-treated	1.5×10^{-9}	0.557	30.48	0.701	11.90

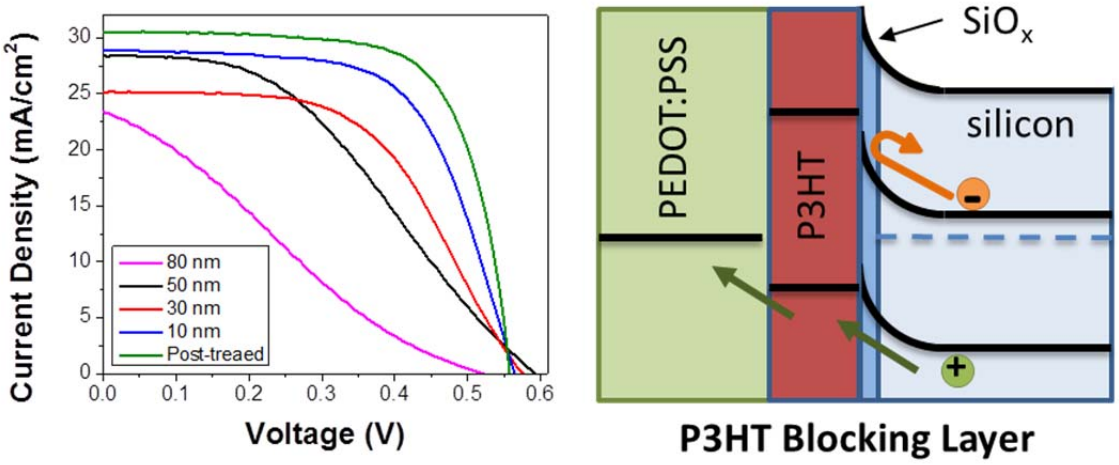

Figure 5.10: (a) Illuminated J(V) curves of PEDOT:PSS-Si HSCs with a P3HT interface layer of different thickness. (b) Schematic of band structure of the P3HT interface layer in the HSC. Orange arrow represents the electron current while green arrows represent the hole current (conventional current).

The relative positions of the band levels of the interfacial layer will determine the carrier transport across the junction, the proper alignment of band energies could favorably facilitate transport of photo-generated minority carriers (holes) while blocking majority carriers (electrons). For an effective electron blocking layer on silicon, the LUMO must be higher than the conduction band, with the HOMO ideally matching or slightly higher than the valance band. A staggered type heterojunction band alignment provides energetically favorable flow of holes while blocking electrons, and P3HT paired with silicon exhibit band levels matching these characteristics as seen in figure 5.10 b. Since the addition of P3HT at the interface has an effect on the carrier lifetime without greatly affecting the diffusion current (as supported by the nearly constant J_o for layer thickness below 80 nm), the P3HT layer is thought not to affect the surface energy and band bending but act as a blocking layer for electrons . Although a P3HT layer is not directly beneficial to HSCs (since excitons created by absorbance outside the silicon base layer do not contribute to the photocurrent), a sufficiently thin such layer (less than 80 nm) does increase the open-circuit voltage acting as an electron blocking layer. Future work will be to develop an appropriate transparent interfacial layer that could also increase the efficiency of these cells.

Combining the calculated maximum short circuit current, of 28.3 mA/cm^2 from chapter 4 and the maximum obtainable open circuit voltage of 0.557 (seen for HSCs using silicon wafers with a resistivity of 1-2 Ω cm and phosphorous doping concentration of 10^{18} cm^{-3} and a 2 nm controlled native oxide layer) and with an achievable fill factor of 0.75, The maximum achievable hybrid solar cell efficiency of 11.8% is obtained for this set up. This could be approved upon through the use of a more highly doped silicon substrate, more transparent or conductive polymer film, or the use of an appropriate blocking layer as shown here.

5.4. Conclusion

The effects of interfacial conditions on HSCs were examined in the present study. First, the passivation of silicon surface was tested. The cells with a 2-nm-thick SiO_x passivation layer are found to perform better than those with H-terminated Si substrate and they produce a greater surface band bending forming an inversion layer. Remarkably, PEDOT:PSS does not appear to protect against the oxide growth on the Si substrate. If the PEDOT:PSS layer is applied without sufficient passivation, formation of a contaminated interface with reduced band bending and reduced open-circuit voltage would occur. Second, as shown in previous chapters, stoichiometric and morphological changes in PEDOT:PSS emitter layer through post-treatment was tested. Post-treatment was found to produce a statistically higher open-circuit voltage and interfacial charge transfer as seen from IQE measurements. Analysis of the dark saturation

current studied showed a significantly lower J_o, and a constant shunt resistance indicative of a change in the effective density of acceptor states with the removal of PSS and incensement of bi-polaron modes as the result of post-treatment. Lastly, P3HT was tested as an interfacial layer. Chlorobenzene resulted in films with good homogeneity but poor crystallinity, while trichlorobenzene was found to produce films with significant crystallinity with the formation of an fibrous network parallel to the substrate, i.e. perpendicular to the direction of electron transport. Films prepared with dichlorobenzene resulted in homogeneous, two-dimensional surface features with interconnected monocrystalline domains, best suited for use in HSCs. When a P3HT blocking layer was deposited between PEDOT:PSS and the silicon substrate, it behaved as a chromophore absorbing light but not as an electron donor as it does in organic heterojunction solar cells, indicating that the depletion region stays in the silicon surface validating the Schottky model. However, the addition of P3HT of an appropriate layer thickness led to the largest open-circuit voltages obtained. Such a P3HT layer was seen to reduce the shunt resistance while maintaining J_o, indicating that it acted as a blocking layer for electrons while allowing holes to pass, likely due to its appropriately positioned band energies. In summary, a passivation layer results in upward band bending through the reduction of surface states. Post-treatment further increases the band bending through the increase in the effective density of acceptor states of the emitter layer, and has been witnessed in higher open circuit voltage, IQE, and in light generated current density in Chapters 3 and 4. Finally, the insertion of P3HT acts as a blocking layer, and selectively blocks electron charge carriers in the silicon while permitting holes to cross.

6. Conclusion and Future work

The highly conducing polymer PEDOT:PSS was paired with n-type silicon to examine its photoelectrical properties in hybrid solar cell devices. First, PEDOT:PSS films were prepared by using the conductivity enhancing methods, including post-treatment and the addition of a co-solvent to the aqueous solution. Then, the optical and electrical properties were quantified to determine the contribution of film thickness on the reflectance and resistivity in order to precisely optimize the short-circuit current of the cell. Finally, the interaction between PEDOT:PSS and silicon was evaluated by examining the formation of the heterojunction and the effect on the open-circuit voltage.

In order to increase the sheet conductivity of spin-coated PEDOT:PSS films, a post-treatment method was developed by using a mixture of ethylene glycol and methanol. The optimal mixture of 50 vol% resulted in a doubling in the sheet conductivity to 1334 ±129 S/cm over films formed from PEDOT:PSS films with ethylene glycol added as a co-solvent (637 S/cm ±58 S/cm). It also resulted in an average 51.7% reduction in film thickness as observed in reflectometry and UV-vis measurements. The conductivity enhancing methods caused a change in the linear conformation of the PEDOT to a more quinoidal character, with the post-treatment method producing the greatest change, as seen with Raman spectroscopy.

FTIR of the effluent post-treatment solution indicated that the observed reduction in film thickness was due to the removal of PSS, which was soluble in the ethylene glycol/methanol solution while PEDOT remained as a film. Observed in AFM images, the nanodomains that make up the film become more defined after post-treatment. However, similarities in topography before and after post-treatment indicate the immutability of the domains and that the PSS is removed uniformly throughout the film. Analysis of individual domains revealed that they deformed after post-treatment, decreasing in height and increasing in aspect ratio, which is attributed to an elongated quinoidal structure of PEDOT chains laying more parallel to the silicon substrate. These large changes observed using 50 vol% ethylene glycol and methanol post-treatment solution are the result of a decrease in viscosity when compared to pure ethylene glycol, and large London dispersion forces capable of intercepting and cause charge screening between the PEDOT and PSS chains. Together with the added benefit of agitation of the polymer caused by Marangoni eddies.

When the films were tested in hybrid solar cells, the open-circuit voltage increased from 0.48 V to 0.49 V, fill factor increased from 0.49 to 0.60 and the efficiency from 6.77% to 8.05% for co-solvent

and post-treated films, respectively. However the property most strongly correlated to the conductivity, the short-circuit current actually decreased after the post-treatment (that improved the conductivity) and went from 27.73 mA/cm^2 to 27.15 mA/cm^2 for co-solvent and post-treated films, respectively. This decrease was attributed to increased absorbance of the PEDOT rich films as observed by UV-Vis spectrometry, and a decrease in quantum efficiency due to increased anisotropy and resistance perpendicular to the substrate.

To explore why post-treatment decreased the short-circuit current and examine the effect of thickness on hybrid solar cells, the optical and electrical properties of the films were thoroughly investigated by fitting the experimental results with thin film optical models. From UV-vis transmittance measurements, the extinction coefficient and refractive index were calculated and they showed that the values obtained for the post-treated films deviated from those of the pristine and co-solvent added films, both of which were similar.

Using the extinction coefficient, the reflectance was modeled using a single stack layer. The reflection spectra of PEDOT:PSS films on silicon were measured at different thicknesses. By fitting the model to the experiment data, the contribution to reflectance of PEDOT:PSS and silicon could be obtained. The thickness at which reflection is minimized and anti-reflectance is maximized was found to be 102 nm. Using the reflectances, index of refraction and phase shift determined through fitting, the model was extended to estimate the quantum efficiency for the amount of energy transmitted into the silicon and then used to fit EQE data and calculate the short-circuit current. It could be seen that J_{sc} followed a sigmoidal curve with increasing thickness with a maximum of 28.3 mA/cm^2 at a thickness of 85 nm for pristine and co-solvent films and 26.2 mA/cm^2 at 63 nm for post-treated films. The experimental data indicated that post-treatment had a significantly lower EQE at higher wavelengths (above 500 nm) resulting in lower overall EQE. Fitting allows the generation and collection of photo carriers entering silicon, Si-Generation, to be determined, from which the collection probability was calculated. The indirect band-gap of silicon contributed to a decreased collection probability between 600 nm and 1050 nm. There was an increase above 1050 nm, which was likely the result of the Lambertian textured rear surface trapping the light.

Knowing the reflectance, quantum efficiency, and absorbance data with respect to the film thickness, the optical and electrical loss mechanisms for incident light could be determined for the optimized 85 nm hybrid solar cell. A respectful 61.5% was captured by the cell and converted to current; 22.2% and

69% was lost to reflectance and absorbance, respectively; 2.7% traversed the cell and was absorbed by the rear electrode; while the remaining 6.7% was lost due to recombination at the surface and in the bulk.

Removing the optical component of the EQE allowed for the electrical contributions to be observed, the internal quantum efficiency. With increasing thickness, the IQE decreased as a result of increasing resistivity. The total IQE was fitted using the single diode equivalent circuit model to obtain a comparative measure of the resistivity, and that for the post-treated films was 75% and 64% more than the that of pristine and co-solvent added films, respectively, which was caused by increase in the anisotropy and resistance perpendicular to the substrate. It was concluded that the maximum short-circuit current density depends on optimizing the decreasing total reflectance and increasing the resistivity and absorbance with thickness. Signifying a decrease in either perpendicular resistivity or absorbance would lead to a higher J_{SC} at a larger thickness.

The hybrid solar cells showed a wide variability in the open-circuit voltage between samples, A detailed examination of the heterojunction using of dark current density was conducted to understand this and to improve performance. Surface passivation of the silicon, by allowing a thin native oxide layer to form naturally in ambient conditions, resulted in a lower ideality factor and dark current density than hydrogen-terminated bare silicon. It was discovered that the oxide layer thickness caused a blue shift in the Raman signal of C_α=C_β band allowing for easy normalization of the substrates. Using this method, it was also found that the oxide growth continued after the application of PEDOT:PSS on H-terminated silicon resulting in a contaminated passivation layer. However, following this peak position with the growth of the oxide layer could also be measured in real time. The continued growth of this contaminated oxide layer under the PEDOT:PSS film resulted in decreasing solar cell performance and increasing ideality factor with time. It was concluded that the dangling bonds of H-terminated silicon created surface defects and Fermi level pinning, applying PEDOT:PSS and allowing oxide layer to grow underneath could encapsulate anionic PSS and other contaminates and increase the number of defects and trap sites reducing the band bending in the space charge region. The controlled growth of a layer of native oxide in clean ambient conditions for 2 hours before the application of PEDOT:PSS resulted in stable high V_{OC}, and low ideality factor solar cells that are the result of a strong inversion layer at the heterojunction.

Consistently higher V_{OC} from the solar simulator measurements, and higher short wavelength IQE for post-treated films indicated favorable heterojunction properties for these cells compared to those with pristine or co-solvent added films. Examination of the dark current density showed that post-treated cells exhibited lower saturation current (1.5×10^{-9} mA/cm^2) and smaller ideality factor than the co-solvent-

added cells (5.8×10^{-8} mA/cm^2) indicating a stronger inversion layer and electron blocking. The removal of PSS from the film after post-treatment and change in the ratio of PEDOT to PSS would change the effective density of acceptor states at the surface resulting in a stronger inversion layer and the observed increase in V_{OC} and IQE. In future work, detailed examination of the dark current density of hybrid solar cells with different ratios of PEDOT to PSS should be conducted in order to determine how the effective density of acceptor states influences the inversion layer in hybrid solar cells.

P3HT was studied to examine the effect of an absorbing, high band gap interfacial thin layer. Solvents with different vapor pressures and boiling points were tested to modify morphology and crystallinity. Crystallinity was observed to increase with lower vapor pressure and higher boiling point. Trichlorobenzene resulted in long crystalline fibers, dichlorobenzene solution resulted in regular elongated 2D structures, while chlorobenzene produced homogeneous short-chain structures. Since films made from dichlorobenzene consisted of small homogenous crystallites with good crystallinity and orientation for perpendicular charge transport, it was applied as an interfacial layer. EQE measurements showed a decrease in efficiency caused by absorbance from P3HT and no beneficial charge carrier generation. This leads to the conclusion that the space charge region shares similar characteristics as a p^+-n junction and lies primarily in the silicon and that charge separation and transfer does not occur on the polymer side of hybrid solar cells. Future work should examine extending the space charge region by placing appropriate inorganic quantum-dot chromophores at the surface to extend and enhance the blue (300- 500 nm wavelength) region.

Dark current density was tested to observe the charge transfer properties with the large band gap P3HT at the interface. A layer thickness of 50 nm resulted in the lowest dark current density obtained in all tests indicating high shunt resistance, even though the dark saturation current was similar as those post-treated films. These results along with a higher EQE seen above 650 nm and higher open-circuit voltage (0.592 V) are associated with increased charge carrier lifetime and charge transfer across the junction with increasing P3HT below 80 nm. Despite this, the increased absorbance from the film, poor conductivity resulting in large series resistance, and a low fill factor resulted in poor hybrid solar cell performance. Future work should be conducted to increase the conductivity of P3HT by doping, or by using a large band gap polymer with higher mobility, or a thin transparent inorganic film such as TiO_2 to serve as a blocking layer.

This thesis took an comprehensive look at all the properties of PEDOT:PSS/silicon hybrid solar cells, a cheap and viable alternative technology to conventional solar cell. This research showcased effec-

tive, and easy ways of quickly increasing the conductivity of PEDOT:PSS through post-treatment and the removal of PSS, however it highlighted that not all conductivity enhancing methods effect devices in the same way. For efficient hybrid solar cells it is important to not compromise the optical and interfacial properties in the drive to increase conductivity. This work exposed the importance of film thickness to device properties. A versatile model was developed that can be used on other hybrid organic/inorganic systems to quickly optimize, and separate the optical and electrical properties. This model should be used as a starting point and validity test to see the suitability of any new hybrid system. The examination of the PEODT:PSS/Silicon heterojunction emphasized the sensitivity and importance of forming an appropriate junction. Under controlled deposition conditions, device post-treatment or through the addition an interfacial blocking layer; changes to the p^{+}-n junction could be realized and exploited for better performance. This work showed that for this combination of materials the highest obtainable efficiency was 11.8%, a respectful value for these modest devices, and it highlighted ways other hybrid solar cell systems improve upon this.

Bibliography

(1) Crabtree, G. W.; Lewis, N. S. Solar Energy Conversion. *Phys. Today* **2007**, *60* (3), 37–42.

(2) U.S. Energy Information Administration. Electric Power Monthly: With Data for May 2014. **2018**, No. May, 1–222.

(3) Muratori, M.; Ledna, C.; McJeon, H.; Kyle, P.; Patel, P.; Kim, S. H.; Wise, M.; Kheshgi, H. S.; Clarke, L. E.; Edmonds, J. Cost of Power or Power of Cost: A U.S. Modeling Perspective. *Renew. Sustain. Energy Rev.* **2017**, *77* (December 2016), 861–874.

(4) Kreith, F. *Principles of Sustainable Energy Systems*; CRC Press, 2014.

(5) Swanson, R. M. A Vision for Crystalline Silicon Photovoltaics. *Prog. Photovoltaics Res. Appl.* **2006**, *14* (5), 443–453.

(6) Zhao, J.; Wang, A.; Green, M. A.; Ferrazza, F. 19.8% Efficient "Honeycomb" Textured Multicrystalline and 24.4% Monocrystalline Silicon Solar Cells. *Appl. Phys. Lett.* **1998**, *73* (14), 1991–1993.

(7) Yang, W. S.; Park, B.-W.; Jung, E. H.; Jeon, N. J. Iodide Management in Formamidinium-Lead-Halide – Based Perovskite Layers for Efficient Solar Cells. *Science (80-.).* **2017**, *356* (6345), 1376–1379.

(8) Yan, L.; Bai, Y.; Yang, B.; Chen, N.; Tan, Z.; Hayat, T.; Alsaedi, A. Extending Absorption of Near-Infrared Wavelength Range for High Efficiency CIGS Solar Cell via Adjusting Energy Band. *Curr. Appl. Phys.* **2018**, *18* (4), 484–490.

(9) Jäckle, S.; Liebhaber, M.; Gersmann, C.; Mews, M.; Jäger, K.; Christiansen, S.; Lips, K. Potential of PEDOT:PSS as a Hole Selective Front Contact for Silicon Heterojunction Solar Cells. *Sci. Rep.* **2017**, *7* (1), 1–8.

(10) Mathew, S.; Yella, A.; Gao, P.; Humphry-Baker, R.; Curchod, B. F. E.; Ashari-Astani, N.; Tavernelli, I.; Rothlisberger, U.; Nazeeruddin, M. K.; Grätzel, M. Dye-Sensitized Solar Cells with 13% Efficiency Achieved through the Molecular Engineering of Porphyrin Sensitizers. *Nat. Chem.* **2014**, *6* (3), 242–247.

(11) Sai, H.; Matsui, T.; Kumagai, H.; Matsubara, K. Thin-Film Microcrystalline Silicon Solar Cells: 11.9% Efficiency and Beyond. *Appl. Phys. Express* **2018**, *11* (2), 0–4.

(12) Yang, Y.; Zhang, Z. G.; Bin, H.; Chen, S.; Gao, L.; Xue, L.; Yang, C.; Li, Y. Side-Chain Isomerization on an n-Type Organic Semiconductor ITIC Acceptor Makes 11.77% High Efficiency Polymer Solar Cells. *J. Am. Chem. Soc.* **2016**, *138* (45), 15011–15018.

(13) Price, M. J.; Foley, J. M.; May, R. a.; Maldonado, S. Comparison of Majority Carrier Charge Transfer Velocities at Si/Polymer and Si/Metal Photovoltaic Heterojunctions. *Appl. Phys. Lett.* **2010**, *97* (8), 8–11.

(14) Kitai, A.; Adrian. *Principles of Solar Cells, LEDs, and Diodes : The Role of the PN Junction*; Wiley, 2011.

(15) Bittner, Z. S.; Spencer, S.; Terrinoni, A.; Hubbard, S. M. A Study on Hybrid Organic/Silicon Heterojunction Solar Cells. *2013 IEEE 39th Photovolt. Spec. Conf.* **2013**, 0997-1002.

(16) Pietsch, M.; Bashouti, M. Y.; Christiansen, S. The Role of Hole Transport in Hybrid Inorganic/Organic Silicon/Poly(3,4-Ethylenedioxy-Thiophene):Poly(Styrenesulfonate) Heterojunction Solar Cells. *J. Phys. Chem. C* **2013**, *117* (18), 9049–9055.

(17) Thiyagu, S.; Hsueh, C.-C.; Liu, C.-T.; Syu, H.-J.; Lin, T.-C.; Lin, C.-F. Hybrid Organic-Inorganic Heterojunction Solar Cells with 12% Efficiency by Utilizing Flexible Film-Silicon with a Hierarchical Surface. *Nanoscale* **2014**, *6* (6), 3361–3366.

(18) Wright, M.; Uddin, A. Organic-Inorganic Hybrid Solar Cells: A Comparative Review. *Sol. Energy Mater. Sol. Cells* **2012**, *107*, 87–111.

(19) Nagamatsu, K. A.; Avasthi, S.; Jhaveri, J.; Sturm, J. C. A 12 % Efficient Silicon / PEDOT : PSS Heterojunction Solar Cell Fabricated at < 100 ◦ C. *IEEE J. Photovoltaics* **2014**, *4* (1), 260–264.

(20) Chi, D.; Qi, B.; Wang, J.; Qu, S.; Wang, Z. High-Performance Hybrid Organic-Inorganic Solar Cell Based on Planar n-Type Silicon. *Appl. Phys. Lett.* **2014**, *104* (19), 193903.

(21) de L. Kronig, R.; Penney, W. G. Quantum Mechanics of Electrons in Crystal Lattices. *Proc. R. Soc. A Math. Phys. Eng. Sci.* **1931**, *130* (814), 499–513.

(22) Bragg, W. L. The Diffraction of Short Electromagnetic Waves by a Crystal. *Scientia* **1929**, *23* (45).

(23) Neamen, D. A. *Semiconductor Physics and Devices: Basic Principles*, 2nd ed.; McGraw-Hill higher education; McGraw-Hill, 2003.

(24) Irene, E. A. *Surfaces, Interfaces, and Thin Films for Microelectronics*; Wiley-Interscience, 2008.

(25) Nelson, J. *The Physics of Solar Cells*; Imperial College Press, 2003.

(26) Zhang, F.; Sun, B.; Song, T.; Zhu, X.; Lee, S. Air Stable , Efficient Hybrid Photovoltaic Devices Based on Poly (3-Hexylthiophene) and Silicon Nanostructures. *Chem. Mater.* **2011**, 2084–2090.

(27) Vilan, A.; Yaffe, O.; Biller, A.; Salomon, A.; Kahn, A.; Cahen, D. Molecules on Si: Electronics with Chemistry. *Adv. Mater.* **2010**, *22* (2), 140–159.

(28) Kirchartz, T.; Ding, K.; Rau, U. *Advanced Characterization Techniques for Thin Film Solar Cells*; Abou-Ras, D., Kirchartz, T., Rau, U., Eds.; Wiley-VCH Verlag GmbH & Co. KGaA: Weinheim, Germany, 2011.

(29) Pizzini, S. Towards Solar Grade Silicon: Challenges and Benefits for Low Cost Photovoltaics. *Sol. Energy Mater. Sol. Cells* **2010**, *94* (9), 1528–1533.

(30) Baron, Andrew; Pinn-Tsong, Chiang; Sravani, Gullapalli; Christopher, Hamilton; Jason, Holden; Christopher, Kelty; Inna, K. *Chemistry of Electronic Materials*; Barron, A. R., Ed.; Connexions, 2011.

(31) The American Society for Testing and Materials (ASTM). Reference Air Mass 1.5 Spectra https://www.nrel.gov/grid/solar-resource/spectra-am1.5.html (accessed Mar 2, 2018).

(32) Shirakawa, H.; Louis, E. J.; Gau, S. C.; Chiang, C. K.; Fincher, C. R.; Park, Y. W.; Macdiarmaid, A. G.; Heeger, A. J. Electrical Conductivity in Doped Polacetylene. *Phys. Rev. Lett.* **1977**, *39* (17), 1098–1101.

(33) Geoghegan, M.; Hadziioannou, G. *Polymer Electronics*; Oxford University Press, 2013.

(34) Joo, J.; Long, S. Charge Transport of the Mesoscopic Metallic State in Partially Crystalline Polyanilines. *Phys. Rev. B - Condens. Matter Mater. Phys.* **1998**, *57* (16), 9567–9580.

(35) Chalmers, J. M.; Editors, P. R. G.; Furukawa, Y. Vibrational Spectroscopy of Conducting Polymers. **2002**.

(36) Scheer, R.; Schock, H. W. (Hans-W.; Wiley InterScience (Online service). *Chalcogenide Photovoltaics : Physics, Technologies, and Thin Film Devices*; Wiley-VCH, 2011.

(37) Armour, M.; Davies, A. G.; Upadhyay, J.; Wassermann, A. Colored Electrically Conducting Polymers from Furan, Pyrrole, and Thiophene. *J. Polym. Sci. Part A-1 Polym. Chem.* **1967**, *5* (7), 1527–1538.

(38) Tourillon, G.; Garnier, F. New Electrochemically Generated Organic Conducting Polymers. *J. Electroanal Chem.* **1982**, *135*, 173–178.

(39) Elschner, A. *PEDOT : Principles and Applications of an Intrinsically Conductive Polymer*; CRC Press, 2011.

(40) F. Jonas, G. Heywang, and W. S. BAYER AG. Patent No. DE 38 13 589, 1988.

(41) G. Heywang, F. Jonas, J. H. and M. D. BAYER AG. Patent No. DE 38 43 412 A1, 1988.

(42) Im, S. G.; Gleason, K. K.; Olivetti, E. A. Doping Level and Work Function Control in Oxidative Chemical Vapor Deposited Poly (3,4-Ethylenedioxythiophene). *Appl. Phys. Lett.* **2007**, *90* (15), 1–4.

(43) Pei, Q.; Zuccarello, G.; Ahlskog, M.; Inganäs, O. Electrochromic and Highly Stable Poly(3,4-Ethylenedioxythiophene) Switches between Opaque Blue-Black and Transparent Sky Blue. *Polymer (Guildf).* **1994**, *35* (7), 1347–1351.

(44) Lock, J. P.; Lutkenhaus, J. L.; Zacharia, N. S.; Im, S. G.; Hammond, P. T.; Gleason, K. K. Electrochemical Investigation of PEDOT Films Deposited via CVD for Electrochromic Applications. *Synth. Met.* **2007**, *157* (22–23), 894–898.

(45) Evans, D.; Fabretto, M.; Mueller, M.; Zuber, K.; Short, R.; Murphy, P. Structure-Directed Growth of High Conductivity PEDOT from Liquid-like Oxidant Layers during Vacuum Vapor Phase Polymerization. *J. Mater. Chem.* **2012**, *22* (30), 14889.

(46) Meng, H.; Perepichka, D. F.; Wudl, F. Facile Solid-State Synthesis of Highly Conducting Poly

(Ethylenedioxythiophene). *Angew. Chemie (International ed.)* **2003**, *42* (6), 658–661.

(47) Guo, C.; Zhou, L.; Lv, J. Effects of Expandable Graphite and Modified Ammonium Polyphosphate on the Flame-Retardant and Mechanical Properties of Wood Flour-Polypropylene Composites. *Polym. Polym. Compos.* **2013**, *21* (7), 449–456.

(48) Ha, Y. H.; Nikolov, N.; Pollack, S. K.; Mastrangelo, J.; Martin, B. D.; Shashidhar, R. Towards a Transparent, Highly Conductive Poly (3,4-Ethylenedioxythiophene). *Adv. Funct. Mater.* **2004**, *14* (6), 615–622.

(49) Groenendaal, L.; Zotti, G.; Aubert, P. H.; Waybright, S. M.; Reynolds, J. R. Electrochemistry of Poly(3,4-Alkylenedioxythiophene) Derivatives. *Adv. Mater.* **2003**, *15* (11), 855–879.

(50) Krafft, F. J. and W. BAYER AG. Patent No. EP 440957, 1990.

(51) Kirchmeyer, S.; Reuter, K. Scientific Importance, Properties and Growing Applications of Poly(3,4-Ethylenedioxythiophene). *J. Mater. Chem.* **2005**, *15* (21), 2077.

(52) Lang, U.; Muller, E.; Naujoks, N.; Dual, J. Microscopical Investigations of PEDOT:PSS Thin Films. *Adv. Funct. Mater.* **2009**, *19* (8), 1215–1220.

(53) K. Router, A. Karbach, H. Ritter, N. W. BAYER AG. Patent No. EP 440974, 2003.

(54) Dupont, S. R.; Novoa, F.; Voroshazi, E.; Dauskardt, R. H. Decohesion Kinetics of PEDOT:PSS Conducting Polymer Films. *Adv. Funct. Mater.* **2014**, *24* (9), 1325–1332.

(55) Heraeus Clevios GmbH. *Clevios PH 1000*; **2010**; Vol. 5.

(56) Lang, U.; Naujoks, N.; Dual, J. Mechanical Characterization of PEDOT:PSS Thin Films. *Synth. Met.* **2009**, *159* (5–6), 473–479.

(57) Greco, F.; Zucca, A.; Taccola, S.; Menciassi, A.; Fujie, T.; Haniuda, H.; Takeoka, S.; Dario, P.; Mattoli, V. Ultra-Thin Conductive Free-Standing PEDOT/PSS Nanofilms. *Soft Matter* **2011**, *7* (22), 10642.

(58) Huang, J.; Miller, P. F.; De Mello, J. C.; De Mello, a. J.; Bradley, D. D. C. Influence of Thermal Treatment on the Conductivity and Morphology of PEDOT/PSS Films. *Synth. Met.* **2003**, *139* (3),

569–572.

(59) Culebras, M.; Go, C. M. Thermoelectric Measurements of PEDOT : PSS / Expanded Graphite Composites. **2013**, 2855–2860.

(60) Kang, H. S.; Kang, H. S.; Lee, J. K.; Lee, J. W.; Joo, J.; Ko, J. M.; Kim, M. S.; Lee, J. Y. Humidity-Dependent Characteristics of Thin Film Poly(3,4- Ethylenedioxythiophene) Field-Effect Transistor. *Synth. Met.* **2005**, *155* (1), 176–179.

(61) Nardes, A. M.; Janssen, R. J.; Kemerink, M. A Morphological Model for the Solvent-Enhanced Conductivity of PEDOT:PSS Thin Films. *Adv. Funct. Mater.* **2008**, *18* (6), 865–871.

(62) Hwang, J.; Amy, F.; Kahn, A. Spectroscopic Study on Sputtered PEDOT · PSS: Role of Surface PSS Layer. *Org. Electron. physics, Mater. Appl.* **2006**, *7* (5), 387–396.

(63) Crispin, X.; Jakobsson, F. L. E.; Crispin, a; Grim, P. C. M.; Andersson, P.; Volodin, a; van Haesendonck, C.; Van der Auweraer, M.; Salaneck, W. R.; Berggren, M. The Origin of the High Conductivity of Poly(3,4-Ethylenedioxythiophene)-Poly(Styrenesulfonate) (PEDOT- PSS) Plastic Electrodes. *Chem. Mater.* **2006**, *18* (4), 4354–4360.

(64) Hwang, J.; Wan, A.; Kahn, A. Energetics of Metal-Organic Interfaces: New Experiments and Assessment of the Field. *Mater. Sci. Eng. R Reports* **2009**, *64* (1–2), 1–31.

(65) Greczynski, G.; Kugler, T.; Keil, M.; Osikowicz, W.; Fahlman, M.; Salaneck, W. R. Photoelectron Spectroscopy of Thin Films of PEDOT – PSS Conjugated Polymer Blend : A Mini-Review and Some New Results. *J. Electron Spectros. Relat. Phenomena* **2001**, *121* (1–3), 1–17.

(66) MacDiarmid, a. G.; Epstein, A. J. The Concept of Secondary Doping as Applied to Polyaniline. *Synth. Met.* **1994**, *65* (2–3), 103–116.

(67) Kim, N.; Kee, S.; Lee, S. H.; Lee, B. H.; Kahng, Y. H.; Jo, Y. R.; Kim, B. J.; Lee, K. Highly Conductive PEDOT:PSS Nanofibrils Induced by Solution-Processed Crystallization. *Adv. Mater.* **2014**, *26* (14), 2268–2272.

(68) Ouyang, J. “secondary Doping” Methods to Significantly Enhance the Conductivity of PEDOT:PSS for Its Application as Transparent Electrode of Optoelectronic Devices. *Displays*

2013, *34* (5), 423–436.

(69) Kim, Y. H.; Sachse, C.; Machala, M. L.; May, C.; Müller-Meskamp, L.; Leo, K. Highly Conductive PEDOT:PSS Electrode with Optimized Solvent and Thermal Post-Treatment for ITO-Free Organic Solar Cells. *Adv. Funct. Mater.* **2011**, *21* (6), 1076–1081.

(70) Bhatt, M. P.; Magurudeniya, H. D.; Rainbolt, E. a.; Huang, P.; Dissanayake, D. S.; Biewer, M. C.; Stefan, M. C. Poly(3-Hexylthiophene) Nanostructured Materials for Organic Electronics Applications. *J. Nanosci. Nanotechnol.* **2014**, *14* (2), 1033–1050.

(71) Jung, B.; Theato, P. Chemical Strategies for the Synthesis of Protein – Polymer Conjugates. *Adv. Polym. Sci.* **2012**, No. May 2012, 1–34.

(72) Avasthi, S.; Lee, S.; Loo, Y. L.; Sturm, J. C. Role of Majority and Minority Carrier Barriers Silicon/Organic Hybrid Heterojunction Solar Cells. *Adv. Mater.* **2011**, *23* (48), 5762–5766.

(73) Chen, T.; Wu, X.; Rieke, R. D. Regiocontrolled Synthesis of Poly(3-Alkylthiophenes) Mediated by Rieke Zinc: Their Characterization and Solid-State Properties. *J. Am. Chem. Soc.* **1995**, *117* (1), 233–244.

(74) Brinkmann, M. Structure and Morphology Control in Thin Films of Regioregular Poly(3-Hexylthiophene). *J. Polym. Sci. Part B Polym. Phys.* **2011**, *49* (17), 1218–1233.

(75) Kim, J. Y.; Jung, J. H.; Lee, D. E.; Joo, J. Enhancement of Electrical Conductivity of Poly(3,4-Ethylenedioxythiophene)Poly(4-Styrenesulfonate) by a Change of Solvents. *Synth. Met.* **2002**, *126*, 311–316.

(76) Marcilla, R.; Salsamendi, M.; Pozo-gonzalo, C.; Carrasco, P. M.; Pomposo, J. a; Mecerreyes, D. Influence of Ionic Liquids on the Electrical Conductivity and Morphology of PEDOT : PSS Films. *Chem. Mater.* **2007**, *8* (17), 2147–2149.

(77) Xia, Y.; Zhang, H.; Ouyang, J. Highly Conductive PEDOT:PSS Films Prepared through a Treatment with Zwitterions and Their Application in Polymer Photovoltaic Cells. *J. Mater. Chem.* **2010**, *20* (43), 9740.

(78) Xia, Y.; Ouyang, J. Anion Effect on Salt-Induced Conductivity Enhancement of Poly(3,4-

Ethylenedioxythiophene):Poly(Styrenesulfonate) Films. *Org. Electron. physics, Mater. Appl.* **2010**, *11* (6), 1129–1135.

(79) Fan, B.; Mei, X.; Ouyang, J. Significant Conductivity Enhancement of Conductive Poly(3,4-Ethylenedioxythiophene):Poly(Styrenesulfonate) Films by Adding Anionic Surfactants into Polymer Solution. *Macromolecules* **2008**, *41* (16), 5971–5973.

(80) Vosgueritchian, M.; Lipomi, D. J.; Bao, Z. Highly Conductive and Transparent PEDOT:PSS Films with a Fluorosurfactant for Stretchable and Flexible Transparent Electrodes. *Adv. Funct. Mater.* **2012**, *22* (2), 421–428.

(81) Jönsson, S. K. M.; Birgerson, J.; Crispin, X.; Greczynski, G.; Osikowicz, W.; Denier van der Gon, a. W.; Salaneck, W. R.; Fahlman, M. The Effects of Solvents on the Morphology and Sheet Resistance in Poly(3,4-Ethylenedioxythiophene)-Polystyrenesulfonic Acid (PEDOT-PSS) Films. *Synth. Met.* **2003**, *139* (1), 1–10.

(82) Pettersson, L. A. .; Ghosh, S.; Inganäs, O. Optical Anisotropy in Thin Films of Poly(3,4-Ethylenedioxythiophene)–poly(4-Styrenesulfonate). *Org. Electron.* **2002**, *3* (3–4), 143–148.

(83) Crispin, X.; Marciniak, S.; Osikowicz, W.; Zotti, G.; Denier Van Der Gon, A. W.; Louwet, F.; Fahlman, M.; Groenendaal, L.; Schryver, F. D.; Salaneck, W. R. Conductivity, Morphology, Interfacial Chemistry, and Stability of Poly (3 , 4-Ethylene Dioxythiophene)-Poly (Styrene Sulfonate): A Photoelectron Spectroscopy Study. *J. Polym. Sci. B* **2003**, *41* (21), 2561–2583.

(84) Rodríguez, A. B.; Voigt, M. M.; Martin, S. J.; Whittle, T. J.; Dalgliesh, R. M.; Thompson, R. L.; Lidzey, D. G.; Geoghegan, M. Structure of Films of Poly(3,4-Ethylene Dioxythiophene)-Poly(Styrene Sulfonate) Crosslinked with Glycerol. *J. Mater. Chem.* **2011**, *21* (48), 19324.

(85) Xia, Y.; Ouyang, J. PEDOT:PSS Films with Significantly Enhanced Conductivities Induced by Preferential Solvation with Cosolvents and Their Application in Polymer Photovoltaic Cells. *J. Mater. Chem.* **2011**, *21* (13), 4927–4936.

(86) Xia, Y.; Ouyang, J. Significant Conductivity Enhancement of Conductive Poly(3,4-Ethylenedioxythiophene): Poly(Styrenesulfonate) Films through a Treatment with Organic Carboxylic Acids and Inorganic Acids. *ACS Appl. Mater. Interfaces* **2010**, *2* (2), 474–483.

(87) Wu, F.; Li, P.; Sun, K.; Zhou, Y.; Chen, W.; Fu, J.; Li, M. Conductivity Enhancement of PEDOT : PSS via Addition of Chloroplatinic Acid and Its Mechanism. *Adv. Electron. Mater.* **2017**, *1700047*, 1–10.

(88) Cruz-Cruz, I.; Reyes-Reyes, M.; López-Sandoval, R. Formation of Polystyrene Sulfonic Acid Surface Structures on Poly(3,4-Ethylenedioxythiophene): Poly(Styrenesulfonate) Thin Films and the Enhancement of Its Conductivity by Using Sulfuric Acid. *Thin Solid Films* **2013**, *531*, 385–390.

(89) Gangopadhyay, R.; Das, B.; Molla, M. R. How Does PEDOT Combine with PSS? Insights from Structural Studies. *RSC Adv.* **2014**, *4* (83), 43912–43920.

(90) Ouyang, J. Solution-Processed Pedot:Pss Films with Conductivities as Indium Tin Oxide through a Treatment with Mild and Weak Organic Acids. *ACS Appl. Mater. Interfaces* **2013**, *5* (24), 13082–13088.

(91) Alemu, D.; Wei, H.-Y.; Ho, K.-C.; Chu, C.-W. Highly Conductive PEDOT:PSS Electrode by Simple Film Treatment with Methanol for ITO-Free Polymer Solar Cells. *Energy Environ. Sci.* **2012**, *5* (11), 9662.

(92) Xia, Y.; Sun, K.; Ouyang, J. Solution-Processed Metallic Conducting Polymer Films as Transparent Electrode of Optoelectronic Devices. *Adv. Mater.* **2012**, *24* (18), 2436–2440.

(93) Thomas, J. P.; Leung, K. T. Defect-Minimized PEDOT:PSS/Planar-Si Solar Cell with Very High Efficiency. *Adv. Funct. Mater.* **2014**, *24* (31), 4978–4985.

(94) Ouyang, J.; Chu, C. W.; Chen, F. C.; Xu, Q.; Yang, Y. High-Conductivity Poly(3,4-Ethylenedioxythiophene):Poly(Styrene Sulfonate) Film and Its Application in Polymer Optoelectronic Devices. *Adv. Funct. Mater.* **2005**, *15* (2), 203–208.

(95) Thomas, J. P.; Zhao, L.; McGillivray, D.; Leung, K. T. High-Efficiency Hybrid Solar Cells by Nanostructural Modification in PEDOT:PSS with Co-Solvent Addition. *J. Mater. Chem. A* **2014**, *2* (7), 2383–2389.

(96) Ouyang, J.; Xu, Q.; Chu, C. W.; Yang, Y.; Li, G.; Shinar, J. On the Mechanism of Conductivity Enhancement in Poly(3,4- Ethylenedioxythiophene):Poly(Styrene Sulfonate) Film through Solvent

Treatment. *Polymer (Guildf).* **2004**, *45* (25), 8443–8450.

(97) Liu, Q.; Imamura, T.; Hiate, T.; Khatri, I.; Tang, Z.; Ishikawa, R.; Ueno, K.; Shirai, H. Optical Anisotropy in Solvent-Modified Poly(3,4-Ethylenedioxythiophene): Poly(Styrenesulfonic Acid) and Its Effect on the Photovoltaic Performance of Crystalline Silicon/Organic Heterojunction Solar Cells. *Appl. Phys. Lett.* **2013**, *102* (24), 243902.

(98) Vitoratos, E.; Sakkopoulos, S.; Dalas, E.; Paliatsas, N.; Karageorgopoulos, D.; Petraki, F.; Kennou, S.; Choulis, S. a. Thermal Degradation Mechanisms of PEDOT:PSS. *Org. Electron. physics, Mater. Appl.* **2009**, *10* (1), 61–66.

(99) Garreau, S.; Louarn, G.; Buisson, J. In Situ Spectroelectrochemical Raman Studies of Poly (3, 4-Ethylenedioxythiophene)(PEDT). *Macromolecules* **1999**, *32* (20), 6807–6812.

(100) Garreau, S.; Duvail, J. L.; Louarn, G. Spectroelectrochemical Studies of Poly (3,4-Ethylenedioxythiophene) in Aqueous Medium. *Synth. Met.* **2002**, *125*, 325–329.

(101) Farah, A.; Rutledge, S.; Schaarschmidt, A.; Lai, R.; Freedman, J. P.; Helmy, A. S. Conductivity Enhancement of Poly(3,4-Ethylenedioxythiophene)-Poly(Styrenesulfonate) Films Post-Spincasting. *J. Appl. Phys.* **2012**, *112* (11), 113709.

(102) Li, L.; Ma, R.; Iyi, N.; Ebina, Y.; Takada, K.; Sasaki, T. Hollow Nanoshell of Layered Double Hydroxide. *Chem. Commun.* **2006**, *2* (29), 3125–3127.

(103) Guo, S.; Solares, S. D.; Mochalin, V.; Neitzel, I.; Gogotsi, Y.; Kalinin, S. V.; Jesse, S. Multifrequency Imaging in the Intermittent Contact Mode of Atomic Force Microscopy: Beyond Phase Imaging. *Small* **2012**, *8* (8), 1264–1269.

(104) Jones, R. L.; Kumar, S. K.; Ho, D. L. Chain Conformation in Ultrathin Polymer ® Lms. **1999**, *400* (July), 146–149.

(105) Nardes, A. M.; Kemerink, M.; Janssen, R. a J.; Bastiaansen, J. a M.; Kiggen, N. M. M.; Langeveld, B. M. W.; Van Breemen, A. J. J. M.; De Kok, M. M. Microscopic Understanding of the Anisotropic Conductivity of PEDOT:PSS Thin Films. *Adv. Mater.* **2007**, *19* (9), 1196–1200.

(106) Takano, T.; Masunaga, H.; Fujiwara, A.; Okuzaki, H.; Sasaki, T. PEDOT Nanocrystal in Highly

Conductive PEDOT:PSS Polymer Films. *Macromolecules* **2012**, *45*, 3859–3865.

(107) Tsierkezos, N. G.; Molinou, I. E. Densities and Viscosities of Ethylene Glycol Binary Mixtures at 293 . 15 K. *J. Chem. Eng. Data* **1999**, *44*, 955–958.

(108) Lee, I.; Kang, C. H.; Lee, B.-S.; Lee, H. W. Thermodynamic Studies on the Structure of Iso-Dielectric Binary Mixtures of Methanol with Ethylene Glycol, Acetonitrile, Nitrobenzene and Nitromethane. *J. Chem. Soc. Faraday Trans.* **1990**, *86* (9), 1477–1481.

(109) Cratin, P. D.; Gladden, J. K. Excess Thermodynamic Properties of Binary Liquid System Ethylene Glycol-Methanol. *J. Phys. Chem.* **1963**, *67* (8), 1665–1669.

(110) Chen, Y.; Ozaki, Y.; Czarnecki, M. A. Molecular Structure and Hydrogen Bonding in Pure Liquid Ethylene Glycol and Ethylene Glycol–water Mixtures Studied Using NIR Spectroscopy. *Phys. Chem. Chem. Phys.* **2013**, *15* (42), 18694.

(111) Thomas, J. P.; Srivastava, S.; Zhao, L.; Abd-Ellah, M.; McGillivray, D.; Kang, J. S.; Rahman, M. A.; Moghimi, N.; Heinig, N. F.; Leung, K. T. Reversible Structural Transformation and Enhanced Performance of PEDOT:PSS-Based Hybrid Solar Cells Driven by Light Intensity. *ACS Appl. Mater. Interfaces* **2015**, *7*, 7466–7470.

(112) Dennler, G.; Forberich, K.; Scharber, M. C.; Brabec, C. J.; Tomiš, I.; Hingerl, K.; Fromherz, T. Angle Dependence of External and Internal Quantum Efficiencies in Bulk-Heterojunction Organic Solar Cells. *J. Appl. Phys.* **2007**, *102* (5), 054516.

(113) Nelson, J. Diffusion-Limited Recombination in Polymer-Fullerene Blends and Its Influence on Photocurrent Collection. *Phys. Rev. B* **2003**, *67* (15), 155203.

(114) Quinten, M. Spectral Reflectance and Transmittance of a Layer Stack. In *A Practical Guide to Optical Metrology for Thin Films*; Wiley-VCH Verlag GmbH & Co. KGaA, 2012; pp 59–80.

(115) Born, M.; Wolf, E. *Principles of Optics : Electromagnetic Theory of Propagation, Interference and Diffraction of Light*; Cambridge University Press, 1999.

(116) Chopra; L., K.; 1933. Thin Film Phenomena. 1969.

(117) Macleod, H. A. (Hugh A.; Angus), H. A. (Hugh. *Thin-Film Optical Filters*; CRC Press/Taylor &

Francis, 2010.

(118) Higashihara, T.; Ueda, M. Recent Progress in High Refractive Index Polymers. *Macromolecules* **2015**, *48* (7), 1915–1929.

(119) Palik, E. D. *Handbook of Optical Constants of Solids*; Academic Press, 1998.

(120) Quinten, M. Thin-Film Thickness Determination. In *A Practical Guide to Optical Metrology for Thin Films*; Wiley-VCH Verlag GmbH & Co. KGaA, 2012; pp 121–140.

(121) Yang, Z.; Fang, Z.; Sheng, J.; Ling, Z.; Liu, Z.; Zhu, J.; Gao, P.; Ye, J. Optoelectronic Evaluation and Loss Analysis of PEDOT:PSS/Si Hybrid Heterojunction Solar Cells. *Nanoscale Res. Lett.* **2017**, *12* (1), 10–15.

(122) Moulé, A. J.; Meerholz, K. Intensity-Dependent Photocurrent Generation at the Anode in Bulk-Heterojunction Solar Cells. *Appl. Phys. B Lasers Opt.* **2008**, *92* (2), 209–218.

(123) Moulé, A. J.; Bonekamp, J. B.; Meerholz, K. The Effect of Active Layer Thickness and Composition on the Performance of Bulk-Heterojunction Solar Cells. *J. Appl. Phys.* **2006**, *100* (9), 094503.

(124) Green, M. A.; Keevers, M. J. Optical Properties of Intrinsic Silicon at 300K. *Prog. Photovolt.* **1995**, *3* (December 1994), 189–192.

(125) Green, M. A. Self-Consistent Optical Parameters of Intrinsic Silicon at 300 K Including Temperature Coefficients. *Sol. Energy Mater. Sol. Cells* **2008**, *92* (11), 1305–1310.

(126) Precker, J. W.; da Silva, M. Experimental Estimation of the Band Gap in Silicon and Germanium from the Temperature–voltage Curve of Diode Thermometers. *Am. J. Phys.* **2002**, *70* (11), 1150.

(127) Padilla, M.; Michl, B.; Thaidigsmann, B.; Warta, W.; Schubert, M. C. Short-Circuit Current Density Mapping for Solar Cells. *Sol. Energy Mater. Sol. Cells* **2014**, *120* (PART A), 282–288.

(128) Benick, J.; Richter, A.; Müller, R.; Hauser, H.; Feldmann, F.; Krenckel, P.; Riepe, S.; Schindler, F.; Schubert, M. C.; Hermle, M.; Bett, A. W.; Glunz, S. W. High-Efficiency n-Type HP Mc Silicon Solar Cells. *IEEE J. Photovoltaics* **2017**, *7* (5), 1171–1175.

(129) Scheer, R.; Schock, H. W. (Hans-W.; Wiley InterScience (Online service). *Chalcogenide Photovoltaics : Physics, Technologies, and Thin Film Devices*; Wiley-VCH, 2011.

(130) Erickson, A. S.; Zohar, A.; Cahen, D. N-Si-Organic Inversion Layer Interfaces: A Low Temperature Deposition Method for Forming a p-n Homojunction in n-Si. *Adv. Energy Mater.* **2014**, *4* (9).

(131) Bardeen, J. Surface States and Rectification at a Metal-Semiconductor Contact. *Phys. Rev.* **1947**, *71* (10), 717–727.

(132) Mönch, W. Barrier Heights of Real Schottky Contacts Explained by Metal-Induced Gap States and Lateral Inhomogeneities. *J. Vac. Sci. Technol. B Microelectron. Nanom. Struct.* **1999**, *17* (4), 1867.

(133) Jäckle, S.; Mattiza, M.; Liebhaber, M.; Brönstrup, G.; Rommel, M.; Lips, K.; Christiansen, S. Junction Formation and Current Transport Mechanisms in Hybrid N-Si/PEDOT:PSS Solar Cells. *Sci. Rep.* **2015**, *5*, 1–12.

(134) He, L.; Jiang, C.; Wang, H.; Lai, D.; Rusli. High Efficiency Planar Si/Organic Heterojunction Hybrid Solar Cells. *Appl. Phys. Lett.* **2012**, *100* (7), 2012–2015.

(135) Zhang, F.; Liu, D.; Zhang, Y.; Wei, H.; Song, T.; Sun, B. Methyl/Allyl Monolayer on Silicon: Efficient Surface Passivation for Silicon-Conjugated Polymer Hybrid Solar Cell. *ACS Appl. Mater. Interfaces* **2013**, *5* (11), 4678–4684.

(136) Zhang, Y.; Zu, F.; Lee, S.-T.; Liao, L.; Zhao, N.; Sun, B. Heterojunction with Organic Thin Layers on Silicon for Record Efficiency Hybrid Solar Cells. *Adv. Energy Mater.* **2014**, *4* (2), n/a-n/a.

(137) McGillivray, D.; Thomas, J. P.; Abd-Ellah, M.; Heinig, N. F.; Leung, K. T. Performance Enhancement by Secondary Doping in PEDOT:PSS/Planar-Si Hybrid Solar Cells. *ACS Appl. Mater. Interfaces* **2016**, *8* (50), 34303–34308.

(138) Scott, A.; Janes, D. B.; Risko, C.; Ratner, M. A. Fabrication and Characterization of Metal-Molecule-Silicon Devices. *Appl. Phys. Lett.* **2007**, *91* (3), 1–4.

(139) Morita, M.; Ohmi, T.; Hasegawa, E.; Kawakami, M.; Ohwada, M. Growth of Native Oxide on a Silicon Surface. *J.Appl.Phys.* **1990**, *68* (1990), 1272–1281.

(140) Raider, S. I. Oxide Growth on Etched Silicon in Air at Room Temperature. *J. Electrochem. Soc.* **1975**, *122* (3), 413.

(141) Walter, M. G.; Liu, X.; Leary, L. E. O.; Brunschwig, B. S.; Lewis, N. S. Electrical Junction Behavior of Poly (3 , 4-Ethylenedioxythiophene) (PEDOT) Contacts to H - Terminated and CH 3 - Terminated p - , n - , and n + - Si (111) Surfaces. **2013**, No. 111.

(142) Schmidt, J.; Titova, V.; Zielke, D. Organic-Silicon Heterojunction Solar Cells: Open-Circuit Voltage Potential and Stability. *Appl. Phys. Lett.* **2013**, *103* (18), 1–5.

(143) Jeong, H.; Song, H.; Pak, Y.; Kwon, I. K.; Jo, K.; Lee, H.; Jung, G. Y. Enhanced Light Absorption of Silicon Nanotube Arrays for Organic/Inorganic Hybrid Solar Cells. *Adv. Mater.* **2014**, *26* (21), 3445–3450.

(144) Wei, W. R.; Tsai, M. L.; Ho, S. Te; Tai, S. H.; Ho, C. R.; Tsai, S. H.; Liu, C. W.; Chung, R. J.; He, J. H. Above-11%-Efficiency Organic-Inorganic Hybrid Solar Cells with Omnidirectional Harvesting Characteristics by Employing Hierarchical Photon-Trapping Structures. *Nano Lett.* **2013**, *13* (8), 3658–3663.

(145) Liu, Q.; Ohki, T.; Liu, D.; Sugawara, H.; Ishikawa, R.; Ueno, K.; Shirai, H. Efficient Organic/Polycrystalline Silicon Hybrid Solar Cells. *Nano Energy* **2015**, *11*, 260–266.

(146) Kim, E.-G.; Bré, J.-L. Electronic Evolution of Poly(3,4-Ethylenedioxythiophene) (PEDOT): From the Isolated Chain to the Pristine and Heavily Doped Crystals. **2008**, No. 3, 16880–16889.

(147) Li, J.; Rochester, C. W.; Jacobs, I. E.; Aasen, E. W.; Friedrich, S.; Stroeve, P.; Moulé, A. J. The Effect of Thermal Annealing on Dopant Site Choice in Conjugated Polymers. *Org. Electron. physics, Mater. Appl.* **2016**, *33*, 23–31.

(148) Jacobs, I. E.; Aasen, E. W.; Oliveira, J. L.; Fonseca, T. N.; Roehling, J. D.; Li, J.; Zhang, G.; Augustine, M. P.; Mascal, M.; Moulé, A. J. Comparison of Solution-Mixed and Sequentially Processed P3HT:F4TCNQ Films: Effect of Doping-Induced Aggregation on Film Morphology. *J. Mater. Chem. C* **2016**, *4* (16), 3454–3466.

(149) Chang, J.; Sun, B.; Breiby, D. W.; Nielsen, M. M. Enhanced Mobility of Poly (3-Hexylthiophene) Transistors by Spin-Coating from High Boiling Point Solvents. *Chem. Mater.* **2004**, *16* (7), 4772–

4776.

(150) Zen, A.; Pflaum, J.; Hirschmann, S.; Zhuang, W.; Jaiser, F.; Asawapirom, U.; Rabe, J. P.; Scherf, U.; Neher, D. Effect of Molecular Weight and Annealing of Poly(3-Hexylthiophene)s on the Performance of Organic Field-Effect Transistors. *Adv. Funct. Mater.* **2004**, *14* (8), 757–764.

(151) Lee, C. S.; Yin, W.; Holt, A. P.; Sangoro, J. R.; Sokolov, A. P.; Dadmun, M. D. Rapid and Facile Formation of P3HT Organogels via Spin Coating: Tuning Functional Properties of Organic Electronic Thin Films. *Adv. Funct. Mater.* **2015**, *25* (36), 5848–5857.

(152) Carach, C.; Gordon, M. J. Optical Measures of Thermally Induced Chain Ordering and Oxidative Damage in Polythiophene Films. **2013**.

(153) Wilson, J. S.; Kim, J.; Brown, P. J.; Thomas, D. S.; Ko, A.; Ramsdale, C. M.; Sirringhaus, H.; Friend, R. H. Effect of Interchain Interactions on the Absorption and Emission of Poly „ 3-Hexylthiophene …. **2003**, 1–16.

(154) Clark, J.; Chang, J.; Spano, F. C.; Friend, R. H.; Silva, C.; Clark, J.; Chang, J.; Spano, F. C.; Friend, R. H.; Silva, C. Determining Exciton Bandwidth and Film Microstructure in Polythiophene Films Using Linear Absorption Spectroscopy Determining Exciton Bandwidth and Film Microstructure in Polythiophene. **2012**, *163306* (2009), 2007–2010.

(155) Spano, F. C. Modeling Disorder in Polymer Aggregates: The Optical Spectroscopy of Regioregular Poly(3-Hexylthiophene) Thin Films. *J. Chem. Phys.* **2005**, *122* (23).

(156) Wang, S.; Fabiano, S.; Himmelberger, S.; Puzinas, S.; Crispin, X.; Salleo, A.; Berggren, M. Experimental Evidence That Short-Range Intermolecular Aggregation Is Sufficient for Efficient Charge Transport in Conjugated Polymers. *Proc. Natl. Acad. Sci.* **2015**, *112* (34), 10599–10604.

(157) Kline, R. J.; Mcgehee, M. D.; Kadnikova, E. N.; Liu, J.; Fre, J. M. J.; Toney, M. F. Dependence of Regioregular Poly (3-Hexylthiophene) Film Morphology and Field-Effect Mobility on Molecular Weight. **2005**, 3312–3319.

(158) Thin Film Heterostructures. *Chalcogenide Photovoltaics*. February 25, 2011.

(159) Eaton, P.; West, P. *Atomic Force Microscopy*; Oxford University Press, 2010.

(160) Inc., A. R. *SPM Applications Guide USER GUIDE 3 Imaging and Spectroscopy Applications Guide*; 2013.

(161) Green, M. A. Lambertian Light Trapping in Textured Solar Cells and Light-Emitting Diodes: Analytical Solutions. *Prog. Photovoltaics Res. Appl.* **2002**, *10* (4), 235–241.

(162) Griffiths, D. J. (David J.; Jeffery), D. J. (David. *Introduction to Electrodynamics*; Prentice-Hall, 1981.

(163) Robinson, T. S. Optical Constants by Reflection. *Proc. Phys. Soc. Sect. B* **2002**, *65* (11), 910–911.

(164) Abelès, F. Optical Properties of Thin Absorbing Films. *J. Opt. Soc. Am.* **1957**, *47* (6), 473–482.

Appendix 1: AM-FM

Atomic force microscopy multifrequency imaging also known as bimoidal AFM, or amplitude modulation frequency modulation (AM-FM) uses multiple lock-in amplifiers to monitor multiple higher order cantilever vibration modes in non-contact mode. [159] Generally the first and the first and the second, or the first and the third fundamental frequency is used, with the higher order is superimposed onto the lower frequency as in Figure A1. In AM-FM the higher frequency mode is adjusted to keep the frequency constant, while the lower frequency maintains amplitude. Since the first fundamental frequency is sensitive to energy loss it is often used with phase imaging to determine physical properties of polymers as well as topographic contributions, but can be influenced by contact area, and viscoelasticity and adhesion. [159,160,103]The higher frequencies are sensitive to tip sample interactions that conserve energy like viscoelasticity, or van-der-Walls interactions which can be converted into quantitative modulus measurements they tend to have a higher quality (Q) factor resulting in sharper images. [159,160,103]

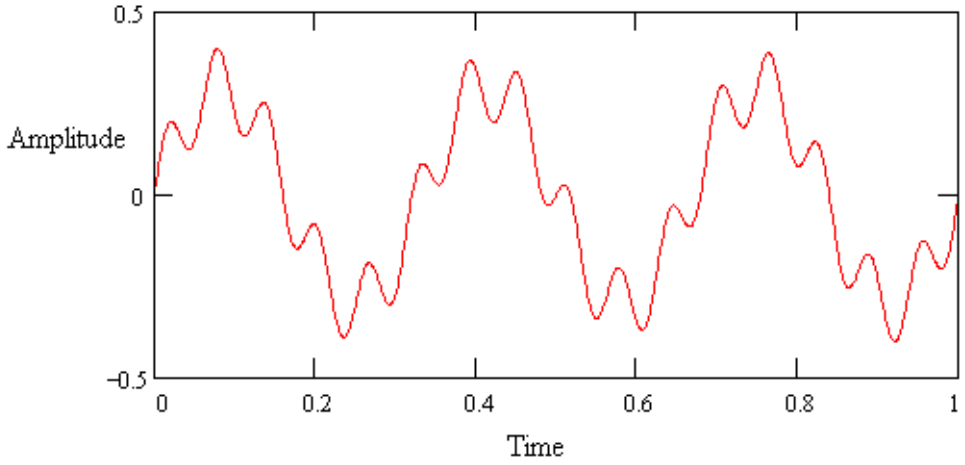

Figure A1: first and second cantilever harmonics superimposted.

Appendix 2: Lavenberg-Marquardt Algorithm

The nonlinear least squares method was used in solving for different parameters since all cases were over determined systems (there were more equations than unknowns). Least squares method minimizes the sum of the squares of the residuals of every curve to be fitted to obtain the optimum solution. Since they are nonlinear they must be solved numerically in an iterative process.

The Lavengerg-Marquardt algorithm (LMA) interpolates between Gauss-Newton algorithm and gradient decent method. Such minimization process is good at finding the local minimum but not always the global minimum. The parameter(s), β, that best minimizes the sum of the squares of the deviations, $s(\beta)$, is:

$$\hat{\beta} = \text{argmin}_{\beta}\, S(\beta) \equiv \text{argmin}_{\beta} \sum_{i=1}^{m} [y_i - f(x_i, \beta)]^2$$

Which minimizes a model curve, $f(x, \beta)$, over a set of empirical curves, m, comprised of independent and dependent variables (x_i, y_i). Informed initial guesses are given for β indicating where to start the iterative procedure to insure proximity to the global minimum. To begin the gradient decent is used to determine the next best value:

$$f(x_i, \beta + \delta) \approx f(x_i, \beta) + \frac{\partial f(x_i, \beta)}{\partial \beta}\delta$$

If the reduction of *S* is too fast or slow a damping factor is added and controlled to avoid getting trapped in a local minimum, and speeding up convergence. This contribution of the Gauss-Newton algorithm.

Appendix 3: Permissions

DISCLAIMER

The National Renewable Energy Laboratory (NREL) is operated for the U.S. Department of Energy by the Alliance for Sustainable Energy, LLC ("Alliance"). As such the following rules apply:

Copyright Status

NREL-authored documents are sponsored by the U.S. Department of Energy under Contract DE-AC36-08GO28308. Accordingly, with respect to such documents, the U.S. Government and others acting on its behalf retain a paid-up nonexclusive, irrevocable world-wide license to reproduce, prepare derivative works, distribute copies to the public, and perform publicly and display publicly, by or on behalf of the Government. Use of documents available from or referenced by this server may be subject to U.S. and foreign Copyright Laws.

Data and Software

Access to or use of any data or software made available on this server ("Data") shall impose the following obligations on the user, and use of the Data constitutes user's agreement to these terms. The user is granted the right, without any fee or cost, to use or copy the Data, provided that this entire notice appears in all copies of the Data. Further, the user agrees to credit the U.S. Department of Energy (DOE)/NREL/ALLIANCE in any publication that results from the use of the Data. The names DOE/NREL/ALLIANCE, however, may not be used in any advertising or publicity to endorse or promote any products or commercial entities unless specific written permission is obtained from DOE/NREL/ ALLIANCE. The user also understands that DOE/NREL/ALLIANCE are not obligated to provide the user with any support, consulting, training or assistance of any kind with regard to the use of the Data or to provide the user with any updates, revisions or new versions thereof. DOE, NREL, and ALLIANCE do not guarantee or endorse any results generated by use of the Data, and user is entirely responsible for the results and any reliance on the results or the Data in general.

USER AGREES TO INDEMNIFY DOE/NREL/ALLIANCE AND ITS SUBSIDIARIES, AFFILIATES, OFFICERS, AGENTS, AND EMPLOYEES AGAINST ANY CLAIM OR DEMAND, INCLUDING REASONABLE ATTORNEYS' FEES, RELATED TO USER'S USE OF THE DATA. THE DATA ARE PROVIDED BY DOE/NREL/ALLIANCE "AS IS," AND ANY EXPRESS OR IMPLIED WARRANTIES, INCLUDING BUT NOT LIMITED TO THE IMPLIED WARRANTIES OF MERCHANTABILITY AND FITNESS FOR A PARTICULAR PURPOSE ARE DISCLAIMED. IN NO EVENT SHALL DOE/NREL/ALLIANCE BE LIABLE FOR ANY SPECIAL, INDIRECT OR CONSEQUENTIAL DAMAGES OR ANY DAMAGES WHATSOEVER, INCLUDING BUT NOT LIMITED TO CLAIMS ASSOCIATED WITH THE LOSS OF DATA OR PROFITS, THAT MAY RESULT FROM AN ACTION IN CONTRACT, NEGLIGENCE OR OTHER TORTIOUS CLAIM THAT ARISES OUT OF OR IN CONNECTION WITH THE ACCESS, USE OR PERFORMANCE OF THE DATA.

Copyright Clearance Center RightsLink®

Home | Create Account | Help

ACS Publications
Most Trusted. Most Cited. Most Read.

Title: Performance Enhancement by Secondary Doping in PEDOT:PSS/Planar-Si Hybrid Solar Cells

Author: Donald McGillivray, Joseph P. Thomas, Marwa Abd-Ellah, et al

Publication: Applied Materials

Publisher: American Chemical Society

Date: Dec 1, 2016

Copyright © 2016, American Chemical Society

LOGIN

If you're a copyright.com user, you can login to RightsLink using your copyright.com credentials.

Already **a RightsLink user** or want to learn more?

PERMISSION/LICENSE IS GRANTED FOR YOUR ORDER AT NO CHARGE

This type of permission/license, instead of the standard Terms & Conditions, is sent to you because no fee is being charged for your order. Please note the following:

- Permission is granted for your request in both print and electronic formats, and translations.
- If figures and/or tables were requested, they may be adapted or used in part.
- Please print this page for your records and send a copy of it to your publisher/graduate school.
- Appropriate credit for the requested material should be given as follows: "Reprinted (adapted) with permission from (COMPLETE REFERENCE CITATION). Copyright (YEAR) American Chemical Society." Insert appropriate information in place of the capitalized words.
- One-time permission is granted only for the use specified in your request. No additional uses are granted (such as derivative works or other editions). For any other uses, please submit a new request.

BACK | CLOSE WINDOW

Copyright © 2018 Copyright Clearance Center, Inc. All Rights Reserved. Privacy statement. Terms and Conditions.
Comments? We would like to hear from you. E-mail us at customercare@copyright.com

Copyright Clearance Center RightsLink®

Home | Account Info | Help

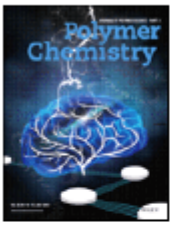

Title: Structure and morphology control in thin films of regioregular poly(3-hexylthiophene)
Author: Martin Brinkmann
Publication: Journal of Polymer Science Part B: Polymer Physics
Publisher: John Wiley and Sons
Date: Jul 11, 2011
Copyright © 2011, John Wiley and Sons

Logged in as:
Donald McGillivray
University of Waterloo
LOGOUT

Order Completed

Thank you for your order.

This Agreement between University of Waterloo -- Donald McGillivray ("You") and John Wiley and Sons ("John Wiley and Sons") consists of your license details and the terms and conditions provided by John Wiley and Sons and Copyright Clearance Center.

Your confirmation email will contain your order number for future reference.

printable details

License Number	4476750671233
License date	Nov 26, 2018
Licensed Content Publisher	John Wiley and Sons
Licensed Content Publication	Journal of Polymer Science Part B: Polymer Physics
Licensed Content Title	Structure and morphology control in thin films of regioregular poly(3-hexylthiophene)
Licensed Content Author	Martin Brinkmann
Licensed Content Date	Jul 11, 2011
Licensed Content Volume	49
Licensed Content Issue	17
Licensed Content Pages	16
Type of use	Dissertation/Thesis
Requestor type	University/Academic
Format	Electronic
Portion	Figure/table
Number of figures/tables	1
Original Wiley figure/table number(s)	Figure 1
Will you be translating?	No
Order reference number	a
Title of your thesis / dissertation	Enhanced Conducting Polymer PEDOT:PSS/ Silicon Hybrid Solar Cells: Optimization of Thin Film Properties and Heterojunction Interactions
Expected completion date	Jan 2019